HABILITATION À DIRIGER DES RECHERCHES

de

l'Université Paris-Saclay

École doctorale de physique PHENIICS

Établissement d'inscription : Université Paris-Sud

Laboratoire d'accueil : Laboratoire de l'Accélérateur Linéaire (UMR 8607 CNRS)

Nicolas DELERUE

Interactions between Laser and Electrons

Date de soutenance : Jour Mois 2018

Jean-Marie DE CONTO	(LPSC CNRS)	Rapporteur
Patric MUGGLI	(Max-Planck-Institut für Physik)	Rapporteur
Franck ZIMMERMANN	(CERN)	Rapporteur
Jury de soutenance : Prénom NOM	(Institution)	Examinateur
Prénom NOM	(Institution)	Examinateur
Prénom NOM	(Institution)	Examinateur
Prénom NOM	(Institution)	Examinateur
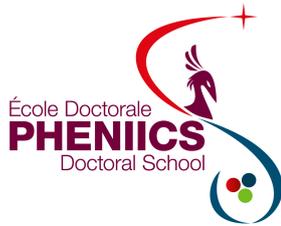
Titre : Interactions entre des Lasers et des Electrons

Mots Clefs : Accélérateurs de particules, Accélération Laser-Plasma, Diffusion Compton, Laser, Mesure d'émittance, Mesure de profile longitudinal

Résumé :

Title : Interactions between Laser and Electrons

Keys words : Compton scatterings, Emittance measurement, Laser, Laser-plasma acceleration, Particle accelerators, Profile measurement

Abstract :

Contents

Chapter 1

Introduction

1.1 History of particle accelerators

1.1.1 Early accelerators

The history of particle accelerators started around the 1870s when Crookes applied a potential difference between two electrodes in a vacuum tube: Cathode rays were observed and they would latter be identified as accelerated electrons [1]. Later Rutherford proposed to use α particles to probe the the inner structure of matter [2] and Geiger and Marsden carried the experiment out on a gold foil in 1908 [3]. For the first time a probe had been used to study subatomic matter. In 1917, by bombarding nitrogen with α particle Rutherford demonstrated that it was possible to transmute an atom by sending a high energy particles onto it [4, 5].

The next step was to find how to accelerate the probe to higher energies. In 1920 Wideröe proposed to use an alternating current in a coil to accelerate electrons by electromagnetic induction, however this was limited by the defocusing induced by the magnetic field. Instead he decided to use radiofrequence (RF) voltages and demonstrated that ions could be accelerated in such way [6]. This idea inspired Lawrence who decided to build a device in which the particles would still be accelerated by RF voltages but a large magnetic field would bend the particles in a circular trajectory between two accelerations. This device became known as a cyclotron and with such design Lawrence accelerated protons to an energy of 1.22 MeV in 1931. This earned him the Nobel Prize in Physics in 1939.

At the same time Cockcroft and Walton used a high voltage generator (now known as a Cockcroft-Walton generator) used to accelerate protons up to an energy of 700 keV. With these protons they succeeded in transmuting lithium into helium [7, 8]. They received the Nobel Prize in Physics in 1951 for this work.

All these researches where halted by the outbreak of the second world war (WWII) but some of the technologies needed by accelerators were developed for other application. For example, the generation of RF wave was boosted by the invention in 1937 of the klystron by the Varian brothers and its development as a power source for radars during the war.

1.1.2   Accelerators after WWII

After the war significant effort were devoted to research in Nuclear physics and this relied heavily on accelerators. In France the research carried at the University of Paris needed more space to build larger devices and in 1956 they were relocated south of Paris, in the Orsay area, where a 1 GeV linear accelerator and a cyclotron were built. The Linear Accelerator Laboratory (*Laboratoire de l'Accélérateur Linéaire*, LAL) was created around this 1-GeV linear accelerator [9].

In 1960 Touschek proposed a ring device, AdA (*Anello di Accumulazione*, accumulation ring in italian) in which electrons and positrons could be injected with the aim of colliding them. In the first attempt, in Frascati, the linac did not deliver a sufficiently energetic beam to allow the production and storage of enough particles to allow the observation of collisions. AdA was then brought to LAL and tested with the LAL linac. These tests were successful and in 1964 the first electron-positron collisions were observed, opening a new era, the colliders era, in high energy physics (HEP) research.

AdA was soon followed by other colliders, VEP-1 (e^-e^- collider) and VEPP-2 (e^-e^+ collider) in Novosibirsk [10], the Princeton-Stanford storage ring experiment and, in Orsay, the Orsay Collider Ring (*Anneau de Collision d'Orsay*, ACO).

The next four decades would see a large number of lepton colliders built, the largest being the CERN's Large Electron Positron collider (LEP) which achieved a center-of-mass energy of more than 209 GeV, the highest center-of-mass energy achieved for e^-e^+ collisions to date.

The European Organisation for Nuclear Research (CERN, formerly *Conseil Européen de la Recherche Nucléaire*) was founded in 1954 to pool european research in nuclear physics. Several proton accelerators and storage rings were built at CERN including the Proton Synchrotron (1959) and the Intersecting Storage Ring (the first proton-proton collider, in 1971).

All these progress with accelerators and colliders have driven discoveries in particle physics and shaped our understanding of elementary particle physics, leading to several Nobel prizes and a very accurate validation of the Standard Model of Particle Physics, culminating with the discovery of the Higgs boson in 2012.

Figure 1.1 gives a non exhaustive list of colliders, their energy and operation dates, showing the tremendous progress made in the field over that past century (such plot is called a "Linvingston plot"). The trend has been to a fast increase of the centrer-of-mass

energy of the lepton colliders with the energy tripling every 6 years from 1960 until 1995. Fewer hadron colliders have been built because they are significantly more expensive but for them it is possible to see that the energy was doubling every 6 years.

This increase in energy required the colliders' circumference to increase even faster: as shown on figure 1.2 from 1963 to 1989 they doubled in size every 2 year, from 3 m to 27 km!

However these trends required more and more construction time between two machines (and also more money) and it is now clear that the next generation colliders will not follow these trends, neither in energy nor in circumference[1]. This breakdown in the trend has led many scientists to say that at the energy frontier accelerator technology has probably reached its limit.

It is important to note that although higher energies open the door to discoveries in particle physics, it is not the only driver for discoveries. Lower energy machines such as KEKB and PEPII have also made important discoveries while being away from the energy frontier. In that case the discovery became possible because the accelerator operated with intense beam and therefore delivered a very high luminosity (the intensity frontier) allowing physicists to collect very large amount of data.

1.2 Applications of accelerators beyond HEP

Although the development of the most impressive accelerators has been driven by high energy physics, these accelerators are only a small fraction of the 17 000 accelerators operating worldwide and more than 650 in France[2].

As early as 1938 Lawrence, together with Chaikoff, decided to study how his cyclotron could be used for medical research. He showed that it could produce isotopes with therapeutic applications. After the war, in 1954, cyclotrons were also used to develop proton therapy (in which a beam of protons is used to kill a cancer tumor). Today Cyclotrons producing medical isotopes can be purchased "off-the-shelf" from specialized companies. There are about 60 proton therapy facilities in the world, the main limitation to their development being their cost, they use a proton beam of a few hundred MeV.

Radiotherapy offers a cheaper alternative to proton therapy. It uses a short linac (about 1 m) to accelerate electrons to about 20 MeV and send them on a tungsten target where they produce X-rays. There are several thousand radiotherapy accelerators installed worldwide (and about 600 in France).

---

[1]If the 100-km circumference Future Circular Collider (FCC) currently being designed, is built before 2032 with at least 50 TeV per beam it will still follow the trend for hadron colliders' energy but not for circumference.

[2]In the case of electron accelerators we do not consider cathode ray tubes such as old television sets but only accelerators where the particles reach an energy of at least 1 MeV.
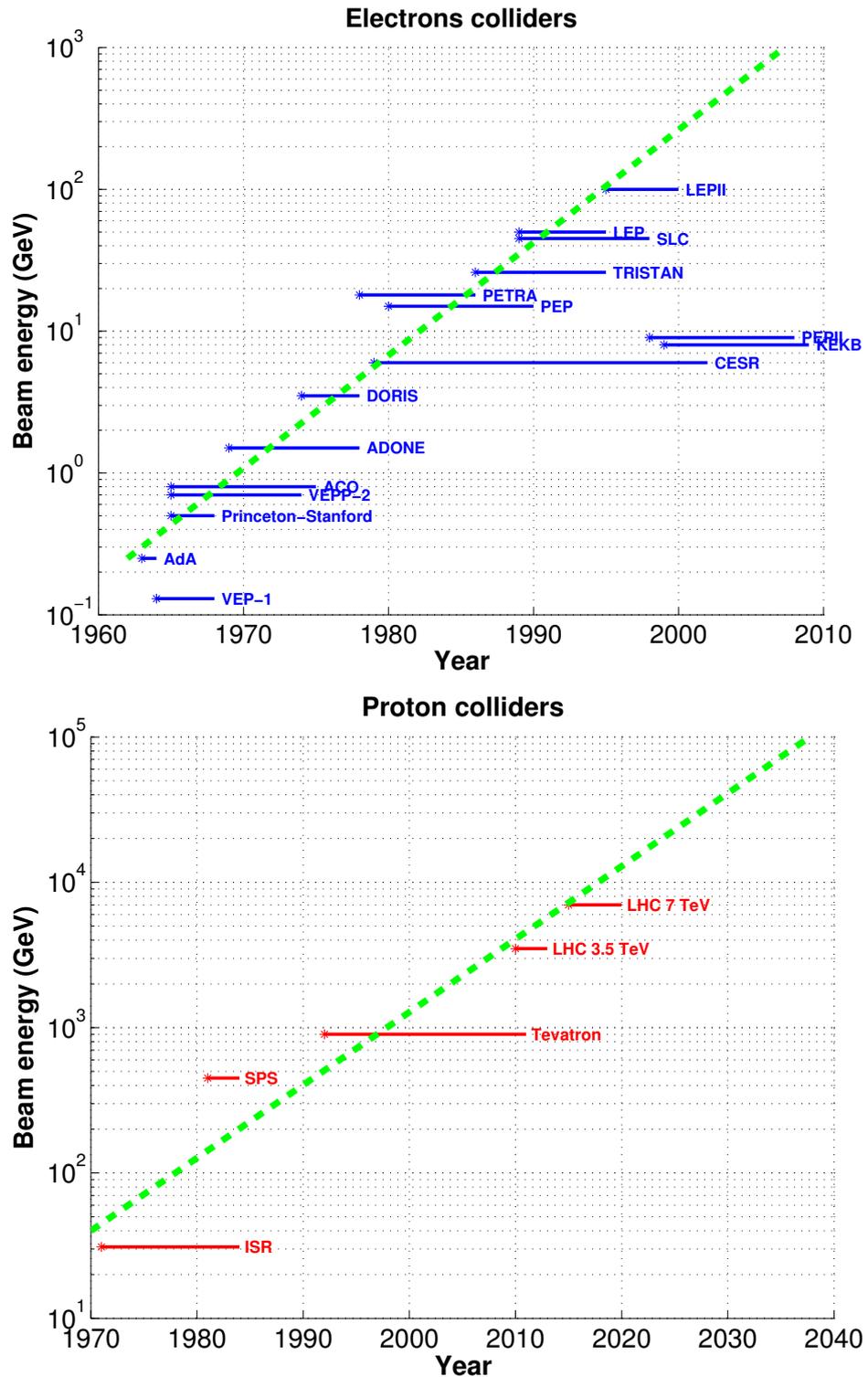
Figure 1.1: Non exhaustive chart showing the energy of colliders versus their operating years. The upper plot is for electron-positron (or electron-electron) colliders, the lower plot is for hadron colliders. The green lines givesa possible trend (energy tripling every 6 years for lepton colliders, energy doubling every 6 years for hadron colliders). The planned ILC, a 1 TeV electron collider, will not follow that trend as it was not operational by 2010 and to follow the protons' colliders trend the FCC, a 50 TeV proton collider, should be operational by 2032.
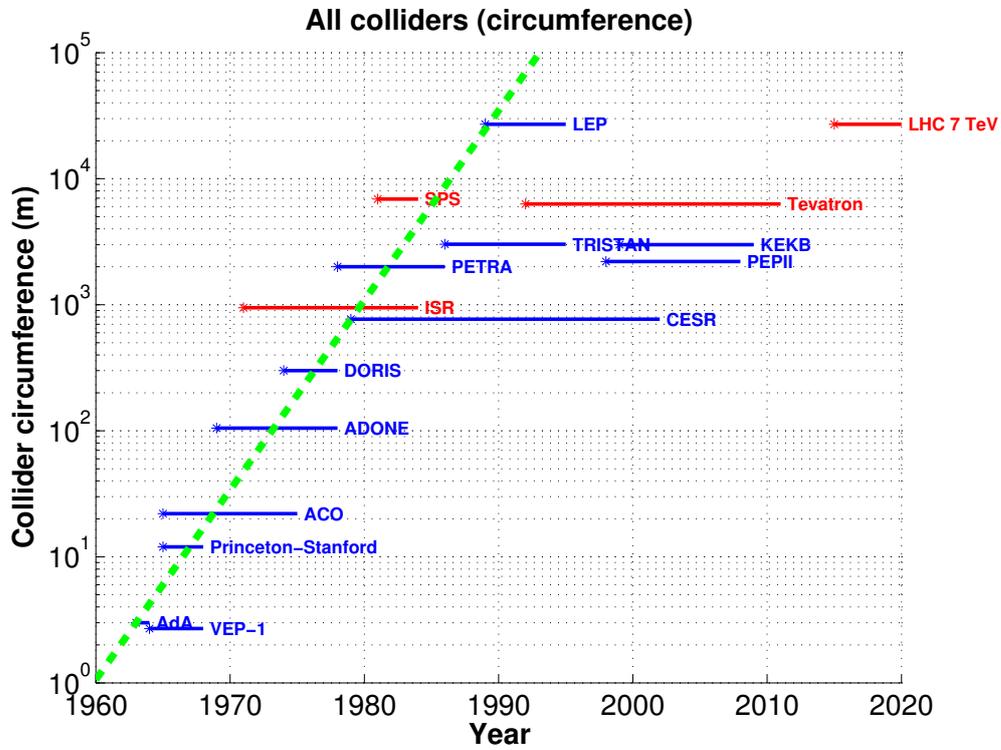
Figure 1.2: Non exhaustive chart showing the circumference of colliders versus their operating years. Lepton colliders are in blue and hadron colliders are in red. The green line gives a possible trend (circumference doubling every 2 years). To follow this trend colliders reaching 100 km should have been operational before year 2000 which was not the case.

When charged particles are accelerated (longitudinally or radially) they emit radiation. When the acceleration occurs radially it is called "Synchrotron radiation". Such radiation was first observed in 1946. It is potentially very bright and can reach wavelength that can hardly be reached by other means giving it a large number of applications in material science, chemistry and biology. It can, for example, be used to determine the elemental composition of a sample, its crystalline structure or the presence of structural defects. Synchrotron radiation light sources typically use a storage ring with a beam of a few GeV electrons. There are about fifty storage rings used as synchrotron radiation light sources installed in the world, including two in France, one near Orsay called "Synchrotron SOLEIL" and one in Grenoble called ESRF (*European Synchrotron Radiation Facility*) [11].

The production of synchrotron radiation can be significantly enhanced by stimulated emission creating a Free Electron Laser (FEL). There are more than a dozen FEL in operation in the world. Unlike storage ring based synchrotron radiation light sources, FEL typically use only a linac to accelerate the electrons. Depending on the wavelength to be reached the length of this linac can be a few tens meters (for infrared) to several kilometers (for hard X-rays). In Orsay there is one FEL called CLIO (*Centre Laser Infrarouge d'Orsay*). It was built jointly by LAL and another laboratory called LURE.

High energy protons sent on a neutron rich nucleus will trigger a process called spallation during which several neutrons are emitted. These neutrons can penetrate deeply in matter and can be used to probe the proton density of a sample. There are about half a dozen spallation sources operating in the world. In addition the neutrons produced during spallation can be used to trigger nuclear reactions in fissile materials. This property is being used in Accelerator Driven Systems (ADS), a new kind of nuclear reactors where the chain reaction is subcritical and the extra neutrons needed to sustain the reactor operations are brought by spallation from an accelerator. ADS are still in the design phase but they are seen as a possible solution to burn nuclear waste.

Accelerator based on Van de Graaff generator with a charge exchange mechanism it the high voltage terminal are called "Tandem". They are still heavily used for research in nuclear physics but also in a variety of other domains such as radiocarbon dating (as done by the LMC14 near Orsay), sample analysis or even to study old artefacts as is being done by the AGLAE accelerator under the Louvres museum in Paris.

All these applications mean that there is a market for turn-key accelerators and most of the accelerators installed worldwide have been built by the industry. Most of the accelerator R&D today is focussed on improving accelerators for HEP, nuclear physics and light sources.

1.3 Accelerators today and state of the art

The largest accelerator today, both by size and by energy per particle is the Large Hadron Collider (LHC) located near Geneva. In proton-proton collisions mode it accelerates beam of 6.5 TeV (to be upgraded to 7 TeV) and in ion-ion collision mode it accelerates $^{208}Pb^{82+}$ ions up to an energy of 2.8 TeV per nucleon. To minimize its power consumption it operates using superconducting accelerating cavities and superconducting magnets. The LHC has replaced the Large Electron-Positron collider (LEP) which was the largest electron-positron collider in the world with an energy of more than 100 GeV per beam. The LEP had superconducting accelerating cavities but normal conducting magnets. Its energy per beam was limited by the loss due to the emission of synchrotron radiation in each bend of the accelerator

After the shutdown of LEP and another lepton collider of slightly lower energy, the Stanford Linear Collider (SLC), the highest energy available for an electron collider decreased significantly with the B factories (PEPII and KEKB) being the highest energy accelerator (asymmetric collisions of 9 GeV on 3.1 GeV for PEPII and 8 GeV on 3.5 GeV for KEKB). This drop in energy can be explained by the large size and power consumption required to build a lepton collider with an energy of the order of 100 GeV per beam or more. PEPII and KEKB have now been shutdown and replaced by SuperKEKB in Japan.

To prepare the next generation colliders several test facilities have being built across the world, focussing on some of the R&D steps required to build the next collider. Among them, I worked at the Accelerator Test Facilty (ATF) at KEK which uses a 1.3 GeV ring and aimed to demonstrate the damping of the beam for a warm technology collider. The ATF has been upgraded into the ATF2 which aims at solving issues related to the beam focussing at the interaction point and associated instrumentation.

I also performed experiments at the Facility for Advanced aCcelerators Experimental Tests (FACET) at SLAC. Which uses two third of the SLC linac to provide experimenters with a 20 GeV beam to study beam driven plasma acceleration and the associated diagnostics.

I also participated in experiments at two tests facilities at the Frascati National Laboratory (LNF): the Beam Test Facility (BTF), a 500 MeV extraction from the LNF linac and SPARC (*Sorgente Pulsata Auto-amplificata di Radiazione Coerente*, Pulsed and Self-Amplified Radiation Source) which is made of a linac delivering a 200 MeV electron beam.

Apart from the LHC, high energy ions collisions can also be obtained a the Relativistic Heavy Ions Collider (RHIC) located in Brookhaven and which can deliver beams of a large number of ions species with energies between 3.85 GeV and 100 GeV per nucleon. In France heavy ions can also be studied (but not collided) at the GANIL (*Grand Accélérateur National d'Ions Lourds*, National Large Accelerator of Heavy Ions) and its

newest facility, SPIRAL2 (*Système de Production d'Ions Radioactifs Accélérés en Ligne*, Production Facility for Radioactive Ions Accelerated Inline).

1.4 Future Accelerators

Progress in HEP and nuclear physics will require more powerful accelerators. The next generation of accelerators is likely to be conventional but advanced concept or completely new design need to be studied for the long term.

1.4.1 Conventional accelerators

The LHC is working well and has already made impressive discoveries but as time passes the discovery potential decreases[3]. Once a sufficient amount of data will have been collected in the present configuration, upgrades will be required (luminosity and possibly energy)[4]. At the moment there is no machine approved and funded to extend the physics reach beyond the LHC. The two main contenders are the International Linear Collider (ILC) and the Future Circular Collider (FCC).

The ILC would be a linac with a length of up to 40 km using superconducting accelerating cavities to accelerate electrons and positrons up to an energy of 250 GeV, 500 GeV or 1 TeV (depending on the results of LHC's run 2). The use of a linac has the advantage of minimizing the energy loss due to synchrotron radiation but it requires fresh particles to be produced and accelerated for each collision. The most likely location to build it would be Japan. One of the key element for the ILC is the gradient that can be achieved in the accelerating cavities. This gradient is limited by irregularities that may appear on the metallic surfaces. These irregularities when exposed to high field will trigger breakdowns. Most of these irregularities can be processed by conditioning the cavities but there will still be a maximum accelerating field that can be achieved for any given cavity. The lower the electromagnetic wavelength the higher the maximum field will be. For L-band (1.3 GHz) cavities for the ILC the design gradient is about 35 MV/m whereas for X-band (12 GHz) cavities gradients beyond 100 MV/m have been achieved. Despite a lower gradient superconducting cavities have been chosen for the ILC as they power consumption is much lower. A linear collider based on warm X-band cavities is also being studied under the name Compact LInear Collider (CLIC).

The FCC would be a ring with a circumference of 100 km. It is foreseen as a machine that would first collide leptons (FCC-ee) with 45 GeV to 200 GeV per beam and then protons (FCC-hh) with about 50 TeV per beam. In both cases the machine will used superconducting accelerating cavities and the FCC-hh will also use superconducting

---

[3]For most studies the discovery potential evolves with the square root of the amount of data collected, so doubling the amount of data collected increases only the discovery potential by a factor 1.4.

[4]The High Luminosity LHC (HL-LHC) is already approved and due to start beyond 2025.

magnet (this is not possible for FCC-ee due to the power lost by synchrotron radiation). It is proposed to built it near CERN. There is also a Chinese project close from FCC-ee called CEPC-SPPC.

One of the key feature of future colliders is that they will have to use cold (superconducting) technology which is much more efficient than warm technology. This choice is less obvious with smaller accelerators as the cost and complexity overhead of an helium cooling plant are not always offset but the power gain.

1.4.2 Energy Recovery Linacs

A key advantage of a ring based collider over a linac is that the particles can be recycled a large number of turns and they are therefore more efficient. However rings have their own limitations such as a limited size at the focal point to avoid disruptive beam-beam effect and the emittance increase due to collective effects. For synchrotron radiation sources rings have the drawback of producing longer particle bunches as they fill their RF bucket and therefore the light pulse produced are longer (typically several picoseconds).

A design to combine the advantages of both has been proposed under the name "Energy Recovery Linac" (ERL) [12]. In an ERL the particles travel in a closed orbit but after one turn they arrive 180° out of phase in the accelerating cavity and are therefore decelerated. Their energy is transferred back as electromagnetic waves in the cavity and a fresh bunch of particles is injected just behind. This fresh bunch will therefore be accelerated by the energy deposited by the previous bunch. This design has been seen as very promising for FELs but designs of colliders using the ERL principle start to be discussed [13].

1.4.3 Plasma accelerators

As discussed above conventional accelerating cavities are limited by RF breakdown. One solution to achieve higher accelerating gradients is to use the ponderomotive force created by a beam in a plasma. Such driver beam can be either a laser pulse or a bunch of charged particles.

The acceleration mechanism in plasma acceleration will be discussed in section **??** (page **??**).

Laser driven plasma acceleration

Electrons   Laser driven plasma acceleration of electrons has been proposed Tajima and Dawson in 1979 [14]. This acceleration occurs when a high power ($> 50\,\mathrm{TW}$) ultra-short ($< 50\,\mathrm{fs}$) laser pulse is sent on low pressure gas volume (either a gas jet or gas confined in a capillary or cell). The laser power ionises the gas, creating a plasma in which a very intense electromagnetic wave propagates and accelerates electrons. The electrons can

either be injected externally (from a conventional injector) or be taken from the plasma (this is called self-injection). The most impressive results so far have been obtained with self-injection but this require sufficient laser power to create a wave-breaking in the plasma that will free the electrons.

The first demonstration of laser-driven plasma acceleration was obtained by the UCLA group in 1994 [15] when they accelerated an externally injected beam of 2.1 MeV to 9.1 MeV another early result was obtained in France in 1998, also with external injection and an electron beam energy gain of 1.6 MeV [16]. A significant breakthrough was made in 2004 when "quasi-monoenergetic" beams of about 100 MeV [17, 18, 19] and two years later a GeV beams was produced [20]. More recently beams of more than 4 GeV have been demonstrated [21] and higher energies have been reported during conferences. These results use the so called "bubble regime" in which the laser pulse is so intense that it creates a region behind it that is fully depleted from electrons. It is in this region that some electrons are captured and accelerated.

A detailed review of developments in laser-driven plasma accelerators can be found in [22] and the energy reached by some of these experiments as function of the year is shown on figure 1.3.
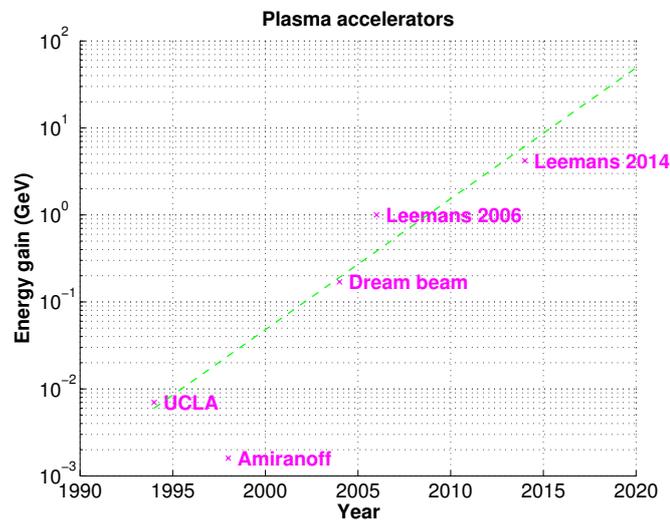
Figure 1.3: Non exhaustive chart showing the electron energy reached in laser-driven plasma acceleration experiment versus the experiment year. The green line shows corresponds to an energy doubling every two years. It is important to stress that the data from this figure show the maximum energy reached, not the energy at which a stable beam was produced as in figure 1.1, therefore the two figures can not be compared directly.

The impressive results obtained in the bubble regime had overshadowed other regimes of acceleration. However in the past few years there has been renewed interest for other

scheme such as the quasi-linear regime with external injection. In this regime the laser pulse is not intense enough to trigger self-injection and therefore the electron have to be brought externally. Several experiments using externally injected electrons from a conventional accelerator have been proposed recently (FLAME at Frascati [23], REGAE and SINBAD [24] at DESY, ESCULAP at LAL [25])

This regime can also be used to reach higher energies by adding several acceleration stages one after the other. The first experimental tests of this technique have been published recently [26].

Although large energies have been reached, the beam stability is not as good as it is in conventional accelerators and therefore significant research are still needed before these accelerators can be used as colliders or even as drivers for a FEL. The charge accelerated are also rather small (1 pC to 10 pC). A design for a laser-plasma linear collider has nevertheless been proposed [27].

Ions   High power ultra-short lasers can also be used to accelerate ions. The laser pulse has to be sent on a thin solid target and the acceleration mechanism is different, it is called Target Normal Sheath Acceleration (TNSA). According to TNSA, when the laser pulse hits the target its energy is transferred to the atoms of the target. The energy then propagates in the target until it reaches the other side where some atoms are ionized and expelled. A current of electrons also propagates in the target in the opposite direction and electrons are emitted toward the laser source. Proton beams of 58 MeV [28] have been reported with a very broad spectrum. This is much less than what was reported for electrons but still very promising. A detailed review of laser-driven ion acceleration can be found in [29].

Beam driven plasma acceleration

The energy required to create the accelerating field in the plasma can also be taken from a bunch of charged particles. SLAC has performed several experiments demonstrating this possibility. In 2007 an experiment at the Final Focus Test Beam (FFTB) reported energy doubling of a few electrons from a 42 GeV beam [30]. More recently FACET at SLAC has seen several progress in that area: acceleration of a higher charge using 2 separate bunches [31], acceleration of positrons [32],... However here the gradient is strongly dependent on the energy of the drive beam. A similar experiment at much lower energy is being planned at SPARC_LAB in Frascati [33].

Another limitation of electron driven plasma acceleration is that the energy gained by one electron has to be taken from another electron which is decelerated by the same amount. To overcome this limitation the AWAKE collaboration [34] proposes to use a beam extracted from the SPS beam at CERN and use it to accelerate electrons. Their simulations show that they could accelerate the electrons to several hundred GeVs. They have recently reported during conferences significant progress toward this goal [35].

Dielectric acceleration

Another technique to transfer power from a high power laser to a beam uses a dielectric conductor. In the case it is directly the electromagnetic field of the optical waves that create the accelerating field. In such accelerators the electrons are naturally bunched at the optical wavelength [36]. Although the gradients achieved so far are lower than in plasma acceleration this technique offers the possibility of miniaturisation of the accelerator with gradients still higher than with a conventional accelerator. In some case a dielectric material can be used to replace the plasma in beam driven plasma acceleration. Given the small size of such accelerators which could be realized almost entirely on a silicium chip, this is sometimes dubbed "accelerator-on-a-chip".

1.5 Diagnostics for accelerators

The operation of accelerators would not be possible without diagnostics giving real time information to the operator on the status of the beam inside the accelerator. Diagnostics use either the fact that charged particle emit radiation while travelling or that they deposit energy when interacting with matter. Diagnostics relying on the radiation emitted include Beam Position Monitor (BPMs), Beam Current Monitors but also more advanced diagnostics such as transition radiation monitors or Smith-Purcell monitors. They usually do not interfere much with the beam. Diagnostics that required energy to be deposited often destroy the beam. They include Faraday cups, wire-scanners and fluorescent screens.

Some beam parameters can be difficult to measure and will require some beam preparation before its measurement. The most common example is the measurement of the beam energy which require first the beam to be deflected with a spectrometer magnet of known energy before its position can be measured with a screen or a BPM. Deflecting cavities and pepper-pots are part of this category.

A significant part of my career has been devoted to developing new diagnostics that allow measurement in can where older diagnostics would fail either because the beam is too intense (for example in the case of laser-wire discussed in chapter 3) or because it is not stable enough (for example with high-energy pepper-pots discussed in chapter **??** or Smith-Purcell monitor, chapter **??**).

Before being used in new facilities these diagnostics had to be tests at conventional accelerators with known characteristics. I have been the pleasure to use several accelerators for that purpose: the Accelerator Test Facility at KEK, the Beam Test Facility at INFN Frascati, the booster to main ring line at the DIAMOND synchrotron, the linac at the SOLEIL synchrotron, the LINAC2 at CERN, FACET at SLAC, the diagnostic line at SPARC at INFN Frascati and the CLIO Linac. Each accelerator has its own specificities as far as beam characteristics are concerned but also the procedures to install a

new equipment, vacuum procedures, safety procedures,... This makes each test a new adventure.

1.6 Lasers

Several of the projects I have worked on involved lasers and it is therefore useful to discuss recent progress with lasers and their applications to particle accelerators.

1.6.1 Recent progress with lasers

Since the first experimental realization of a LASER (Light Amplification by Stimulated Emission of Radiation) in 1960 the development of lasers has been very fast. In a LASER, atoms from a suitable medium are pumped to a higher energy level so that a population inversion is created. The spontaneous emission of a photon by one of these atoms will provoke massive stimulated emission by the other atoms of the amplification medium. Mirrors are often used to form a cavity in which the photons recirculate, increasing the photon yield at each pass. Damages in the amplification medium limit the maximum power that can be reached in a laser. Until the 1980's this prevented the production of short pulses as in such pulses the power can be very large. This changed after the demonstration of chirped pulse amplification (CPA) in which a laser pulse is stretched by a grating before being amplified and then recompressed.

The spread of CPA has led to high-power ultra-short laser pulses such as those used in laser-plasma acceleration. Today terawatt lasers producing sub-picoseconds pulses are not restricted to laser laboratories but can be purchased commercially and leading manufacturers (including at least two french companies) are not afraid of offering for sale Petawatt class laser (however the price is of the order of several million euros making it a not-so-common purchase). These high-power lasers typically use titane sapphire (Ti:Sa) as amplification medium as it has a wide amplification band which is important for CPA. Although they can be purchased commercially it is important to note that, like accelerators, such lasers require significant maintenance to operate them on a daily basis and very few of them are designed to operate round-the-clock like an accelerator.

The availability of Petawatt class lasers at an affordable cost has led to progress in physics and in particular in laser-plasma acceleration. In the UK I have had the opportunity to work on the ASTRA-Gemini Petawatt laser just after its commissioning. In France I have had the opportunity to do research both on Laserix and UHI-100 which are two laser from the hundred-TW class.

The laser community is now working on more ambitious lasers with a target power of about 10 PW per beam. This is the aim of the APOLLON laser currently being developed near Orsay but also of the ELI-NP laser to be installed in Magurele (Romania).

For applications that do not require ultra-short pulses but only picosecond pulses other amplification materials are available than Ti:Sa. Nd:YAG (Neodymium-dopped yttrium aluminum garnet, $Nd : Y_3Al_5O_{12}$) and Nd:YLD (Neodymium-dopped yttrium lithium fluoride) offer better efficiency and are easier to pump (but they have a much narrower amplification band).

The telecom industry has made an extensive use of laser to transport information over long distances. This has led to the development of erbium-doped fibers lasers. Fiber lasers have the advantage of producing radiation that is already in a fiber and therefore it does not have to be coupled in a fiber (an operation that is always source of losses). The beam quality in a fiber is usually much better than in solid-state lasers and because all elements of the laser are spliced together there is no risk of misalignment. As the fiber has a large outer surface heat load management is also easier.

The advantages of Erbium-doped fiber lasers have encouraged research in other amplification medium, leading to the apparition among others of Ytterbium-doped fiber lasers. Ytterbium is much more resistant to high power the Erbium and this has led to the development of high-power fiber lasers. This power yield has been increased further by specially designed fiber components that allow chirping (and de-chirping) of these narrow band laser pulses, allowing CPA with pulsed lasers. The high quality of the beam produced by these lasers has also made them a good choice as seed oscillators for high power amplification. Two experiments on which I worked, Laser-Wire and MightyLasers, used fibers lasers as oscillator and in the case of MightyLaser the full laser chain was made of fibers.

1.6.2   Applications of lasers in accelerators

Lasers can enhance the performances of accelerators in several ways. At the source of an electron accelerator, a laser can be used to produce the electrons by photoelectric effect instead of thermionic effect. This has the advantage of producing a bunch of electrons with a lower emittance and allow the production of pulses shorter than what can be achieved with a pre-buncher and a buncher. This mechanism is used in several photo-injectors around the world, including PHIL at LAL. In the case of ion sources a laser can be used to selectively ionise one atom to a desired charge state with a better efficiency than other mechanism. Resonant Ionization Laser Ion Source (RILIS) is a common method to produce radioactive ions and it used in several facilities such as ISOLDE at CERN , ISAC at TRIUMF, REGLIS at SPIRAL2 and at IPN Orsay in the RIALTO line.

Further down the accelerator the alignement of the components is important to preserve the emittance along the linac. Laser based alignement techniques are now a common procedure in almost all accelerators.

Compton scattering of laser photons on the electrons (or ions) of the accelerator, can be used either as a diagnostics (as is done in the Laser-Wire project) or as a source of

intense X-rays or gamma-rays (as is done in the MightyLaser, ThomX and ELI-NP-GS projects).

Part I

Compton scattering

Chapter 2

Introduction to Compton scattering

Compton scattering is the scattering of a photon by an electron. It has first been proposed when describing the process that occur in the atomic shell where the photons have more energy than the electrons. As the typical energy of a visible photon is about $1\,\text{eV}$ whereas the typical energy of an electron in an accelerator is several MeV, this process is called *Inverse Compton Scattering*. It is represented by the Feynman diagram on figure 2.1.
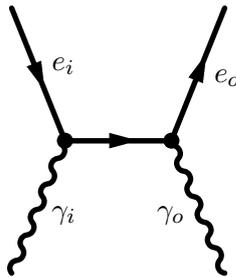

Figure 2.1: Feynman diagram of Compton scattering.

In this process the outgoing photon (γ_o) will gain energy and be scattered at an angle θ_o with respect to the plane defined by the incoming electron (e_i) and photon (γ_i). The angle between the incoming photon and electron is θ_γ. In most experiments described in this document the later will be injected transversely with respect to the electron beam, hence $\theta_\gamma = 90°$. To compute the photon energy gain one needs to look at the frequency of the incoming photon in the lab frame ν_i and the electron frame [37]:

$$\nu'_i \quad = \quad \nu_i[\gamma(1 + \beta \sin \theta_\gamma)] = \nu_i[\gamma(1 + \beta)] \tag{2.1}$$

In the electron frame the photon frequency does not change during the Compton scat-

tering ($\nu'_i = \nu'_o$) however the emitted photon is boosted by the electron with respect to the lab frame:

$$\nu_o = \nu'_o[\gamma(1 + \beta\cos\theta_o)] = \nu_i[\gamma^2(1 + \beta)(1 + \beta\cos\theta_o)] \tag{2.2}$$

and with $\beta \to 1$:

$$\nu_o \simeq \nu_i[2\gamma^2(1 + \beta\cos\theta_o)] \tag{2.3}$$

The maximum energy shift is achieved for $\theta_o = 0°$:

$$\nu_o = 4\gamma^2\nu_i \tag{2.4}$$

For Laser-Wire and MightyLaser the electron beam energy at the ATF was $1.27\,\mathrm{GeV}$ (that is $\gamma = 2540$) hence the maximum scattered photon energy was about $26\,\mathrm{MeV}$. For ThomX, the beam energy will be $50\,\mathrm{MeV}$ and the maximum photon energy about $40\,\mathrm{keV}$.

If we take $\theta_o = \gamma^{-1}$, from equation 2.3 we see that the energy of the outgoing photons drop by half.

The cross-section for the process is given by the Thompson scattering cross-section:

$$\sigma_T = \frac{8\pi}{3}r_e^2 \simeq 6.65 \times 10^{-29}\,\mathrm{m}^2 \tag{2.5}$$

with r_e the classical radius of the electron.

The luminosity of an electron-photon collider is given by:

$$\mathcal{L} = f\frac{n_e n_\gamma}{4\pi\sigma_x\sigma_y} \tag{2.6}$$

where f is the collision rate, n_e and n_γ the number of electrons and photons respectively in the interaction area and σ_x and σ_y the transverse dimensions of the interaction area.

Assuming a beam squeezed to a size of $\sigma_x = 25\,\mu\mathrm{m}$ and $\sigma_y = 10\,\mu\mathrm{m}$, the luminosity per particle and per crossing becomes $\mathcal{L} = 3.18 \times 10^4 \frac{\mathrm{m}^{-2}}{N_e \times N_\gamma}$.

The scattering probability at each crossing is therefore :

$$\mathcal{P}_{\mathrm{scat}} = \mathcal{L} \times \sigma_T = 2.12 \times 10^{-24} \text{ per electron and per photon} \tag{2.7}$$

Assuming a bunch of $160\,\mathrm{pC}$, that is $N_e = 10^9$, each photon has a probability $\mathcal{P}_{\mathrm{scat}} = 2.12 \times 10^{-15}$ of colliding during the crossing between the laser and the electron bunch.

As we can see this probability is very small and this explains why in the MightyLaser experiment the photons are recycled in a Fabry-Perot cavity.

A laser pulse of $E = 1\,\mathrm{nJ}$ of infra-red photons ($\lambda = 1048\,\mathrm{nm}$; $E_\gamma \simeq 2 \times 10^{-19}\,\mathrm{J}$) contains $n_\gamma \simeq 5 \times 10^9$ photons and the probability of scattering for an electron when the two bunches cross is therefore 10^{-14}. The use of a ring to circulate the electrons is therefore also justified.

Chapter 3

Compton scattering as a beam diagnostic: Laser-wire

The beam delivery section of the International Linear Collider (ILC) [38] will be used to tune high intensity beams with high accuracy to focus them to the nanometric size required at the interaction point. To achieve this, the beam size will have to be know with micrometer accuracy. Neither screens nor conventional wire-scanners are able to sustain such high flux while giving such small resolution. A proposed solution would be to use a laser-wire instead of a wire-scanner.

In a laser-wire a tightly focussed high-power laser beam crosses an electron beam. The Compton scattering that occurs is proportional to the number of electrons across the laser path. By moving the laser beam it is possible to measure the transverse profile of the beam with an accuracy corresponding to the size of the laser beam in the interaction area.

This technique has been pioneered at the SLC [39]. A variant of it has been tested at high power H^- accelerators such as SNS [40] and the ISIS Test Stand in the UK [41]. For H^- machines, the physical process involved is photodissociation instead of Compton scattering.

I joined a R&D group to demonstrate the feasibility of a laser-wire for the ILC in 2004. Our aim was to demonstrate the possibility of scanning the ATF extraction line beam with micrometer resolution.

3.1   Large aperture lens design

One of the key points of this experiment was the design of a lens capable of giving a diffraction limited (or almost) spot at the interaction point. In addition this lens has to include as one of its optical elements a fused silica window (to allow the transition

between the air and the accelerator vacuum) and be radiation hard. The radiation hardness required the use of only fused silica (although test made later have shown that optics made of another glass, BK7, have a good lifetime under radiation as well and thus could have been used). As the lens had to be outside the vacuum it had to have a long focal lens (longer than 24 mm).

The solution chosen at SLC of using a parabolic mirror inside the vacuum was rejected as this did not allow scanning the laser beam sufficiently fast for the ILC requirement (the SLC laser-wire scanned the beam by moving the chamber vertically).

I designed such lens using the ZEMAX [42] Optical Design Software and documented it in [43]. Only its main features (taken from [43]) are described here.

This lens is made of 3 elements: the first element has an aspheric surface and a spheric one. The second element has two spheric surfaces. The last element is flat and is used as a window to allow the laser light to enter the beam pipe. All these element are made of top-quality fused silica. Beam dynamics and mechanical considerations require the inner side of the window to be more than 20 mm away from the interaction point (IP) which must be roughly in the centre of the beam pipe, in this design this inner surface of the window is 24 mm away from the IP. The window has a thickness of 12.7 mm. The position of the two other elements is constrained by mechanical and cost consideration: to allow the sealing of the window these two elements must be more than 14 mm away from the window but they must be kept as close as possible to the window to limit their size (and hence their cost). In our design one of these elements is located 18 mm away from the window and has a thickness of 5.3 mm. The second element (aspheric) is located 2 mm further away and has a thickness of 7 mm. The layout of this lens and the energy distribution from the centroid are shown in figure 3.1.

As only fused silica could be used the lens could not be achromatic and it was designed to work with frequency doubled Nd:YAG lasers.

One of the difficulties with this design is that each surface can also act as a reflective mirror. This is especially true with the input window as it is flat. Given that this lens was designed to be used with a high power laser we wanted to avoid any ghost focus inside the glass element. However after several attempts we did not find any reasonable solution and therefore we settled for a design with a second order ghost with a diameter of 500 µm in the first element as shown on figure 3.2. Our calculation showed that this ghost would not be an issue at the design power. After several year of operation these predictions have proven true.

3.2   Experiment at the ATF

The lens was part of an experiment that I coordinated with the aim to install a laser-wire in the extraction line at the ATF at KEK in Japan. The experiment is detailed in [44].
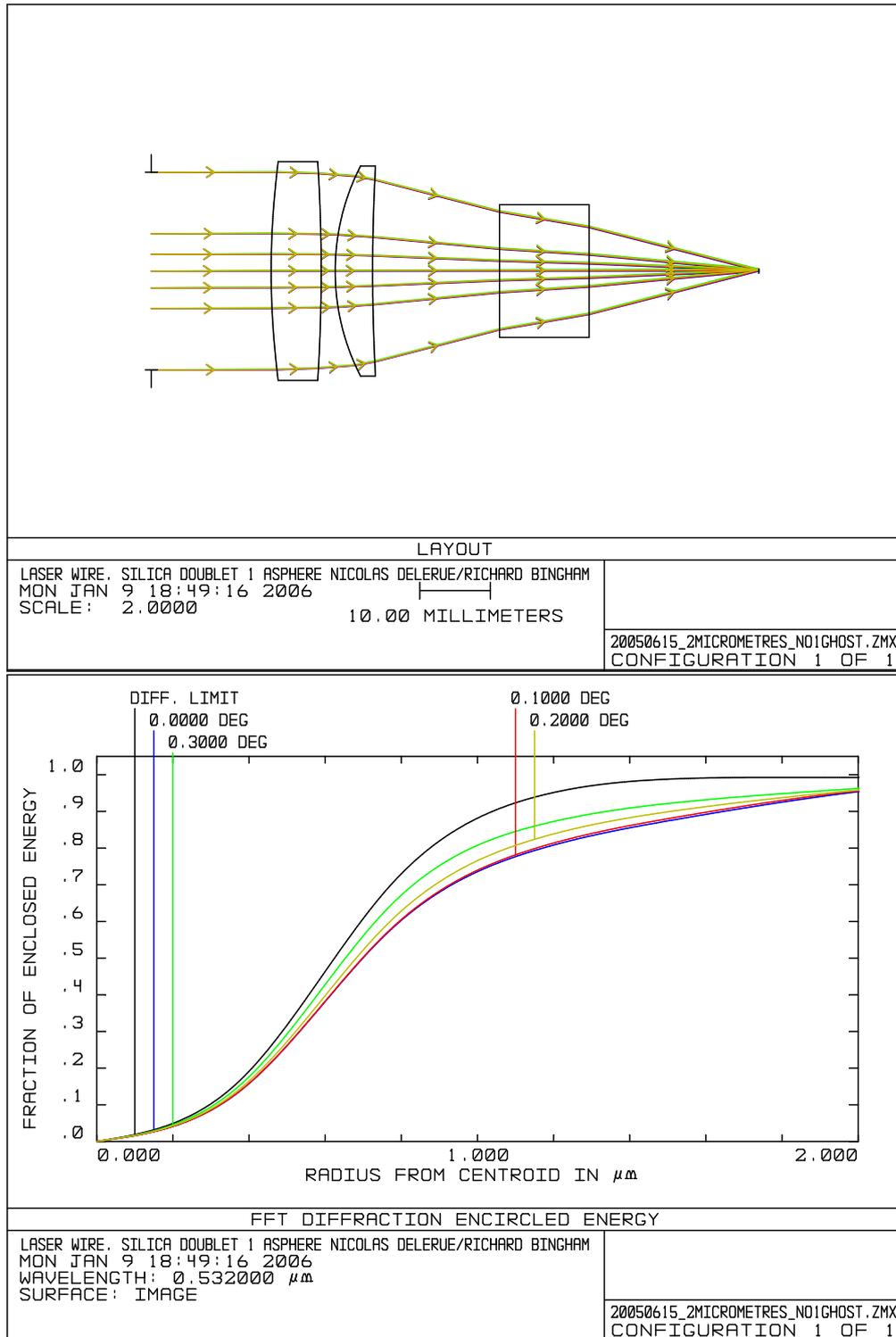
Figure 3.1: Laser-wire lens doublet design (top) and energy distribution from the centroid (bottom). The upper (black) line shows the diffraction limit, the 4 other lines show the real value when the incoming laser beam has a tilt of 0 degree (blue), 0.1 degree (red), 0.2 degrees (yellow) and 0.3 degrees (green). Images taken from [43].
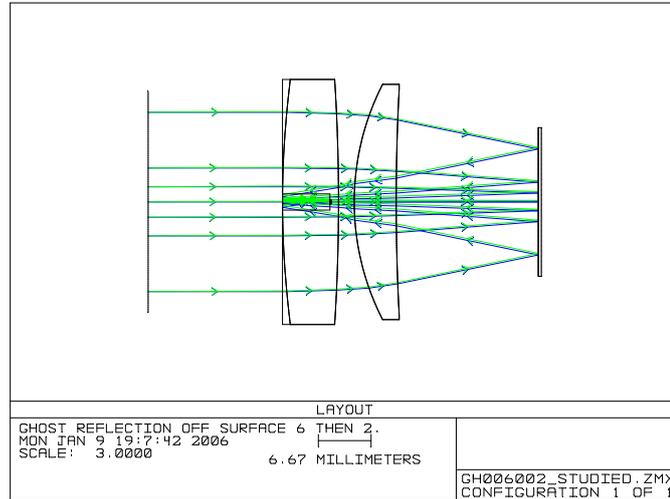
Figure 3.2: This ghost reflection of the lens focus is formed by a reflection on the outer surface of the vacuum window and on the aspherical surface.

The main novelty of the experiment was to be able to scan with a micrometer resolution thanks to the lens described above. The system also had to be compatible with ultrafast scanning (kHz rate) to allow a bunch profile measurement in a single train at the ILC although we used a slower system at the ATF as the repetition rate was only 1.65 Hz. A description of the ATF can be found in [45].

The experiment was installed in a bend of the ATF extraction line to allow an easy extraction of the γ rays produced by Compton scattering. The layout of the ATF extraction line with the location of the laser-wire is shown in figure 3.3. The laser was installed above the extraction line and a telescope brought the laser radiation near the IP. An optical table allowed to measure the laser properties near the IP. Some laser diagnostics were also installed after the IP to monitor the laser during data taking. The laser delivery layout is shown on figure 3.4. A calorimeter was located behind a bending magnet to measure the γ rays produced.

One of the main difficulty for this experiment was to find the collisions. As both the laser beam had by design a very small size the it was very difficult to find the overlap between the two beams. One of the lessons I learned from this experiment is that we should have kept the possibility of defocussing the laser at first (for example with a lens on a translation stage) to have a larger laser spot size while trying to adjust the other parameters (especially the laser phase with respect to the electron bunches arrival time).
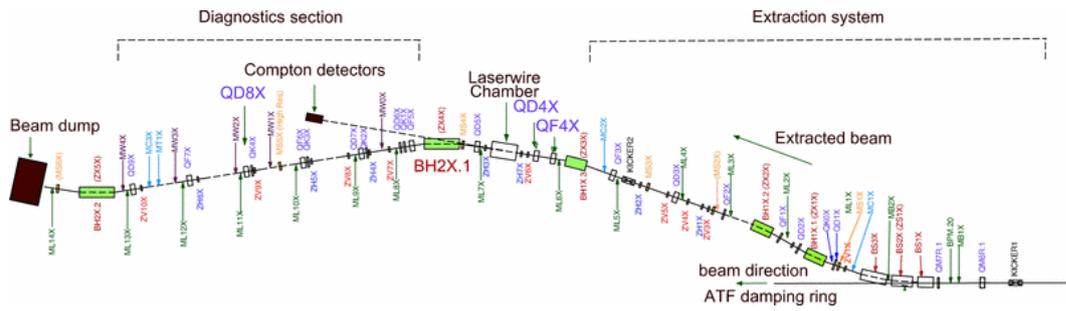
Figure 3.3: Layout of the ATF extraction line showing the location of the laser-wire. Image taken from [44].
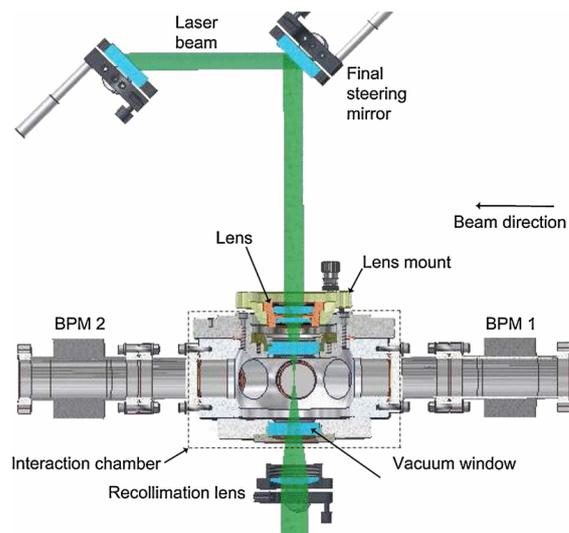
Figure 3.4: Experimental layout of the laser-wire installed in the ATF extraction line. Image taken from [44].

3.3   High repetition rate laser

Another key point in the laser-wire R&D was to demonstrate that a laser suitable for the needs of the ILC could be built. The power of this laser had to be chosen so that a sufficient number of photons would be produced at each collision to allow a fast scanning of the beam. However the beam quality had to be good enough to give a micrometer resolution and, given the chromatic constraints of the lens discussed above, it had to have a narrow wavelength width. The requirements of this laser have been summarized in [46]. I was in charge of the technology choice for this laser.

My calculation showed that we needed about 10 MW of laser power with a pulse duration of 1 ps. One of the limiting factor was the specific repetition rate required: to match the ILC repetition rate the laser had to produce burst of pulses at a pulse repetition rate of 6.5 MHz (or 3.25 MHz) during 900 μs at a train repetition rate of 5 Hz.

Several technologies were available to us. The most mature technology to give high power is clearly Titane Sapphire (Ti:Sa). Back in 2006 I visited factories in the US were several Ti:Sa lasers were being assembled at the same time. At the time such large production line did not exist for the other technologies (or at last not with the suppliers we visited).

However the mode quality offered by suppliers of Ti:Sa lasers was not as good as that of Nd:YAG or Nd:YLF lasers. During the process of the technology choice we paid particular attention to Ytterbium fibers lasers (already discussed in section 1.6.1). Although that technology was not as mature as Ti:Sa or Nd:YLF it had a clear potential and we were confident[1] that on the timescale of the construction of the linear collider[2]. So in the end we decided to choose a fiber laser from Amplitude Systèmes with some developments to be done together [47].

The scheme on which we converged was to buy the laser oscillator commercially and to do the amplifier ourselves, taking advantage of the recent developments of photonics crystal fibers to achieve the power required. This development was not complete when I left Oxford but it was on a good way [48].

---

[1]And 6 years later I visited in France production lines of fibers lasers that were comparable to those I had seen earlier in the US for Ti:Sa lasers.

[2]Back in 2006, it was expected that the ILC would be built before 2020.

Chapter 4

Compton scattering as a source of X-rays: MightyLaser

4.1 The MightyLaser experiment

The aim of the MightyLaser experiment at the KEK ATF is to demonstrate that it is possible to produce high flux of polarized γ rays. Such flux could be used, for example, to produce polarized positrons at a high rate for the ILC. The experiment uses a Fabry-Perot cavity to enhance the laser power. It builds on previous efforts done at LAL [49] to use Fabry-Perot cavities for Compton scattering. The MightyLaser cavity has the specificity of using a pulsed laser to increase the peak power that can be achieved. For better stability it uses 4 mirrors in a "bow tie" configuration (as shown on figure 4.1). The cavity and the project have been described in details in [50]. I joined the project at the end of year 2010 when most of the hardware developments had already been done. They are documented in [50]. My main contribution to this project has been to lead the experimental campaign at the KEK ATF as described below.

4.2 Experiment at the ATF

The installation of an instrument in an accelerator bring a large number of additional constraints compared to a laboratory environment. The constraints include the inability to access the hardware (including oscilloscopes close from the experiment) during the operations, additional vibrations, thermal effects,... On MightyLaser we had to adjust the experiment to these constraints by developing tools that allowed us to control and operate the cavity remotely. We also had to correlate our measurements with the accelerator status to show that what we measured was a real signal and not an unexpected background. Our first results (obtained before the earthquake that devastated Japan in

29
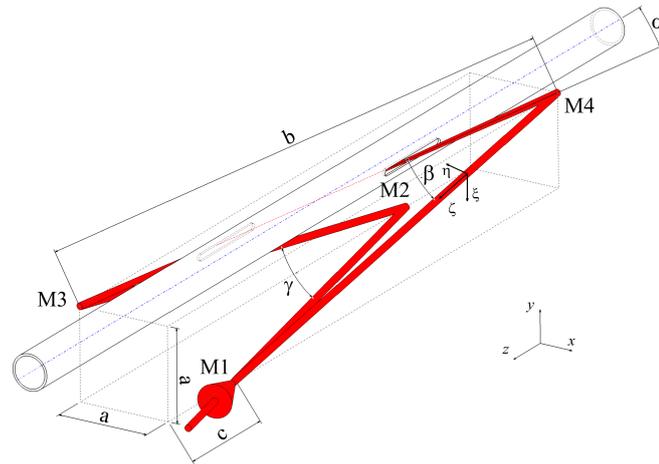
Figure 4.1: Schematic drawing of the four-mirror cavity installed at ATF as published in [50]. The laser beam is represented by the red cones and the incident laser beam by a red arrow.

2011) are documented in [51, 52].

Together with a graduate student, Iryna Chaikovska, I developed most of these remote tools. The layout of data acquisition system that we developed over a few weeks to be ready for the data taking is shown on figure 4.2.

Examples of the data we obtained are shown in figure 4.3. The full analysis is documented in [52] and in Iryna Chaivovska's thesis [53].

After the earthquake the lack of environmental control in the accelerator during several weeks required significant work to put the cavity back in working order. After attempts to do this work in Japan it was decided to do it in France before a reinstallation in Japan. It was only in December 2012 that we were ready to take data again with a significantly increased power enhancement in the cavity. This power enhancement was however limited by new problems such as the heat load on the mirrors which modified there curvature and hence the geometry of the cavity[1]. Example of the results obtained at that time are shown on figure 4.4 and have been published in [55].

4.3   Beam dynamics of Compton scattering at the ATF

Another important point was to understand the effect of Compton scattering on the electron beam stored in the ring. Although it was not expected to have any significant effects on the beam with the laser power that we had in the cavity this was an important

---

[1]These problems were later solved during the thesis of another graduate student (Pierre Favier[54]) but I was not part of tis work.
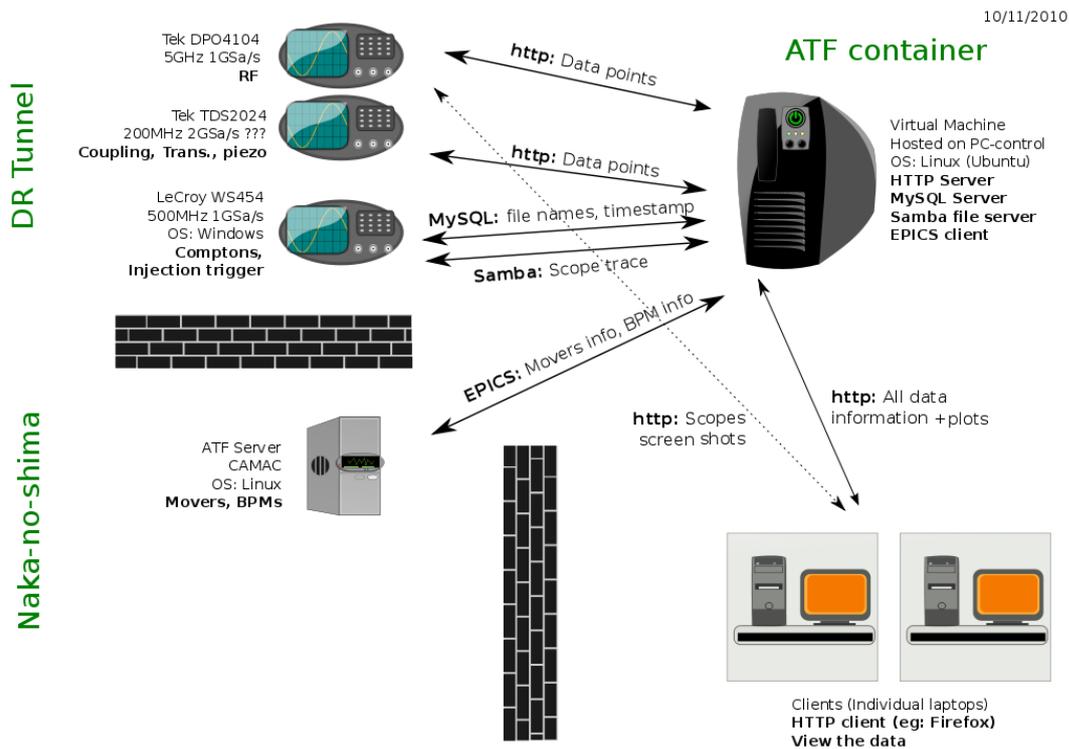
Figure 4.2: Layout of the data acquisition system developed for the MightyLaser experiment at KEK.
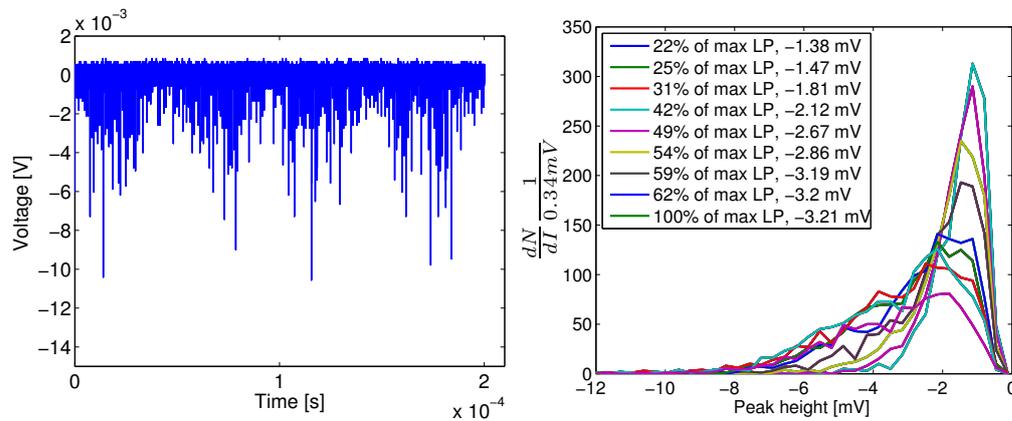
Figure 4.3: Left: image from [52] showing the typical signal shape for the high energy γ rays produced by Compton scattering observed in the MightyLaser experiment. Each spike on the picture corresponds to the γ production after successive bunch crossings over 0.2 ms. Right: image from [51], showing the γ ray spectrum for different laser power (LP) stored in the Fabry-Perot cavity.
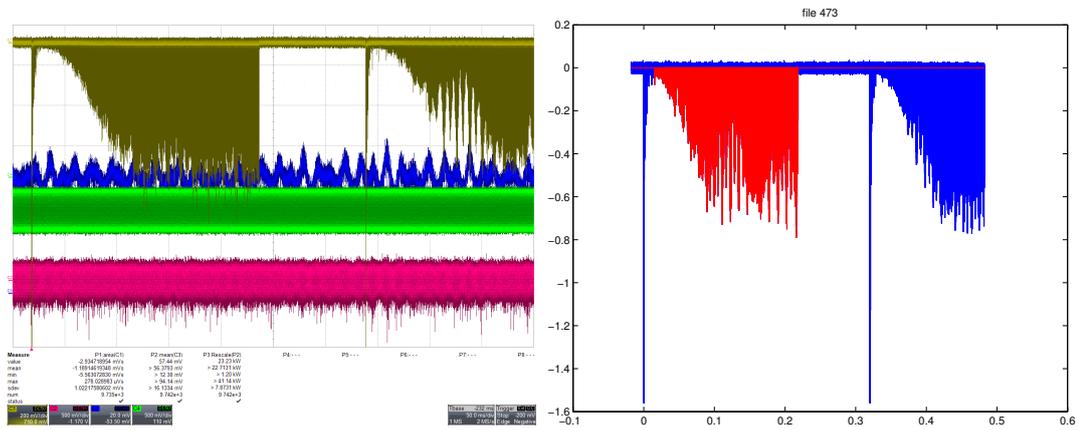
Figure 4.4:   (left) Typical screen shot of a the data taken during one electron storage period with the laser power obtained in December 2012. The gamma ray signal from the calorimeter is shown in brown (this signal is negative because of the PMT bias), the photodiode signal giving the power in the cavity is shown in blue. The pink and green signals are used to monitor beam condition. (right) Example of data after processing: only the red area is considered as being signal for a given beam (the blue peak to the left corresponds to noise observed during the injection of the beam in the ring and the blue area to the right corresponds to signal from another beam injection).

point to check. This work was done by Iryna Chaikovska under my guidance [53, 56]. It showed that given the short storage duration no effect were to be expected and even the beam diagnostics in the extraction line would not be sensitive enough to see anything. After the 2012 upgrade when we took long data runs we noticed (see figure 4.5) that we were clearly able to see in our data the effect of intrabeam scattering as predicted by [57] and this has to be taken into account when predicting the total flux that can be produced. These results have been published [55].

This work also led me to similar work applied to the ThomX ring. It will be described in chapter 5.

4.4   Extension: ELI-NP-GS

The success of the work on MightyLaser led to other applications. In particular the European Light Infrastructure project (ELI) for its Nuclear Pillar (NP) will use Compton scattering for its Gamma Source (GS).

At first we considered using a Fabry-Perot cavity for this application as had been done in MightyLaser however a quick calculation shows that given the high γ flux required and
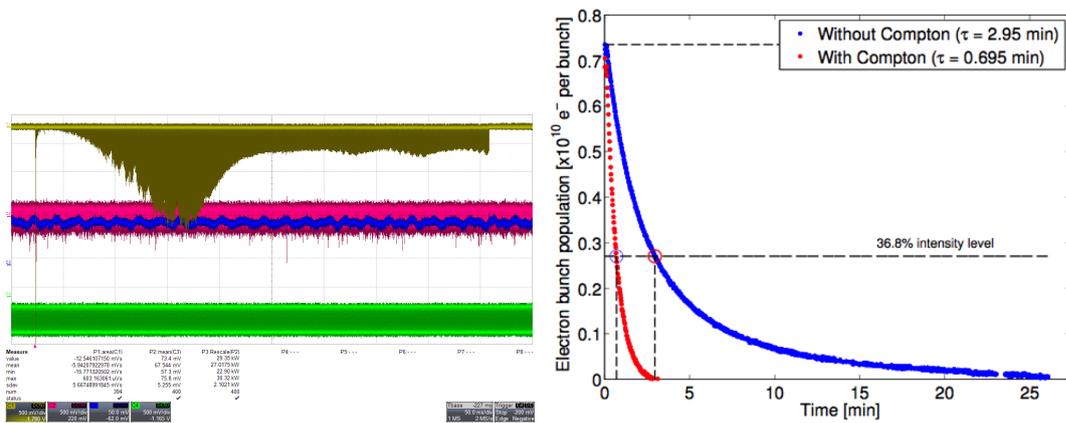
Figure 4.5:   (left) Data taken during one long electron storage period. The effect of the electron damping (from 50ms to 150ms) is clearly visible as well as the effect of intrabeam scattering after that. The gamma ray signal from the calorimeter is shown in brown (this signal is negative because of the PMT bias), the photodiode signal giving the power in the cavity is shown in blue. The pink and green signals are used to monitor beam condition. (Right) Beam charge as a function of time with and without Compton. The effect of Compton scattering on particle losses is clearly visible.

the low repetition rate (128 pulses[2] per macro pulse repeated at $100\,\mathrm{Hz}$) this solution is not favored. Two reasons explain this: the average power stored in the cavity would induce significant thermal effects[3] and loading a cavity for only 128 crossings would waste more power (due to the reflexion on the input mirror) than it would save thanks to the power enhancement inside the cavity, the laser system would therefore be more complicated. Instead of a cavity we therefore decided to use recirculator made of a large set of mirrors between which the pulses would bounce between each pass at the interaction point.

The beam crossing angle required significant attention: the Compton cross-section is much higher in the case of head-on collisions than when the beam has a higher crossing angle. However the mirrors need to be positioned around the interaction point and a small crossing angle prevent the positioning of a sufficient number of mirrors. This is illustrated on figure 4.6. Although this points to a large number of pulses other parameters (and further optimisation) led to the choice of 32 pulses.

Further optimisation work was necessary to be able to adjust the timing between each pulse to the structure of the train. The resulting recirculator has been documented in [58] (and is now being built but I no longer work on this project). The whole technical

---

[2]At that time 32, 64 or even 128 crossing were considered; it was later decided to have only 32 crossings as it made the geometry easier.

[3]When we did this work, in November 2011, we did not know that we would already see the thermal effects at the ATF experiment but we suspected that such effect would appear at an average power lower than what was required for ELI-NP-GS.
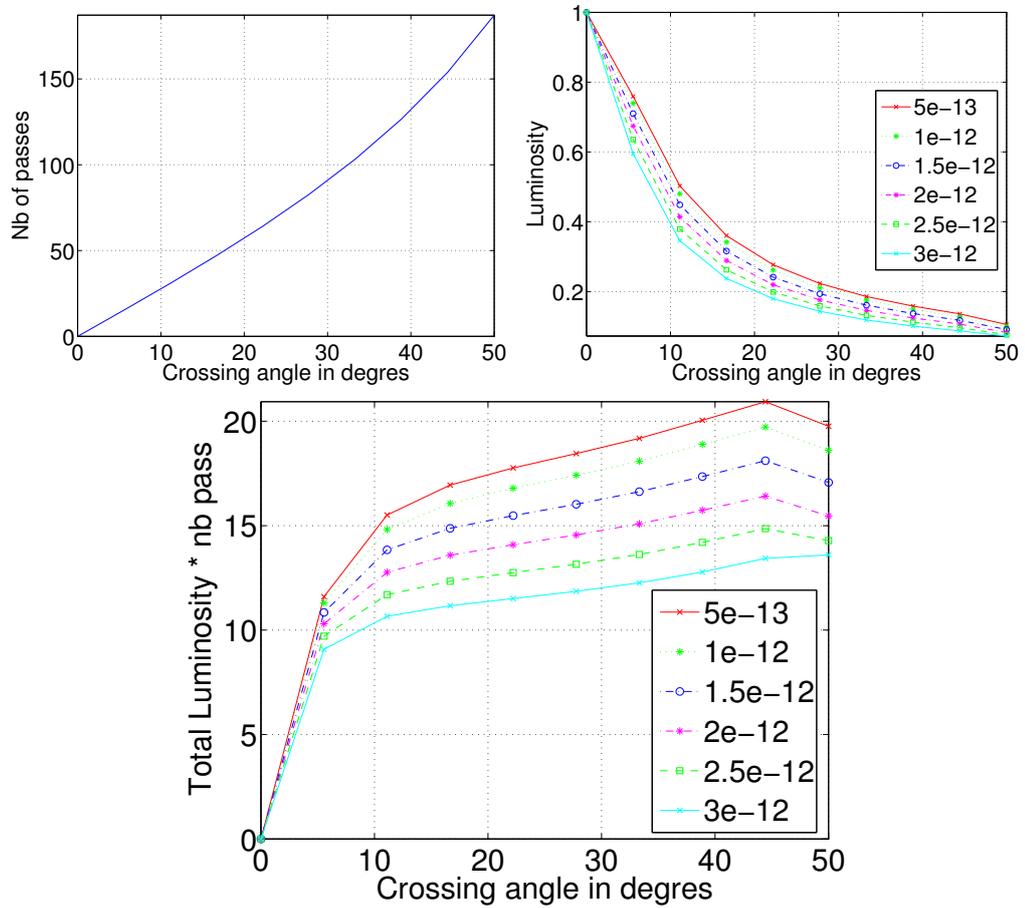
Figure 4.6: (top left) Number of passes possible as a function of the crossing angle. (top right) Luminosity as a function of the crossing angle (normalized to the maximum luminosity) for different laser pulse duration (FWHM laser pulse duration given in the legend in seconds). (bottom) Same figure but summed over the number of passes.

description of the project has been documented in [59]. This proposal was discussed and negotiated for more than a year with our Romanian counterparts and it is now under construction.

Chapter 5

A compact X-rays source: ThomX

The expertise available at LAL in Fabry-Perot cavities makes it an ideal place for the development of a Compact Light Source based on Compton Scattering. This project is called ThomX and it has been described extensively in [60]. When I joined the project it was already under way. My contributions to this project are the optical diagnostics which are documented in [60], the synchronisation which will be discussed in section 6.3 and studies of the beam dynamics in the ThomX ring, including the guidance of a graduate student on that subject [61]. I will also be in charge of the commissioning of the ThomX ring.

5.1   Beam dynamics at ThomX

The ThomX ring will have a circumference of about $16.8\,\text{m}$ [60] and a beam energy of $50\,\text{MeV}$. A fresh beam will be injected every $20\,\text{ms}$ whereas the damping time will be of the order of $0.5\,\text{s}$ to $1\,\text{s}$. This will put the machine in a transitory regime that has not been explored so far. It is therefore important to understand beforehand how each effect in the ring will affect the beam, what will be the competition between these effects and how to optimise the various parameters to maximise the X-ray production.

This work has been done with a graduate student, Illya Drebot, and it is extensively documented in his thesis [61] as well as in [62]. It is briefly summarized here.

One of the key findings is that Compton scattering is not, by far, a dominant effect in the disruption of the beam. Simulations with and without Compton scattering yield very similar results (however our implementation of Compton scattering based on CAIN [63] make simulations with Compton scattering much slower [61]).

When it is injected in the ring the bunch is not matched to the ThomX ring, in particular it is much smaller (longitudinally) than the RF bucket. The first few thousand turns will therefore see the bunch expand to fill its bucket and this effect is amplified under the effect of Coherent Synchrotron Radiation (CSR). One the bunch has expanded and fillets bucket CSR becomes much weaker. This is illustrated on figure 5.1.
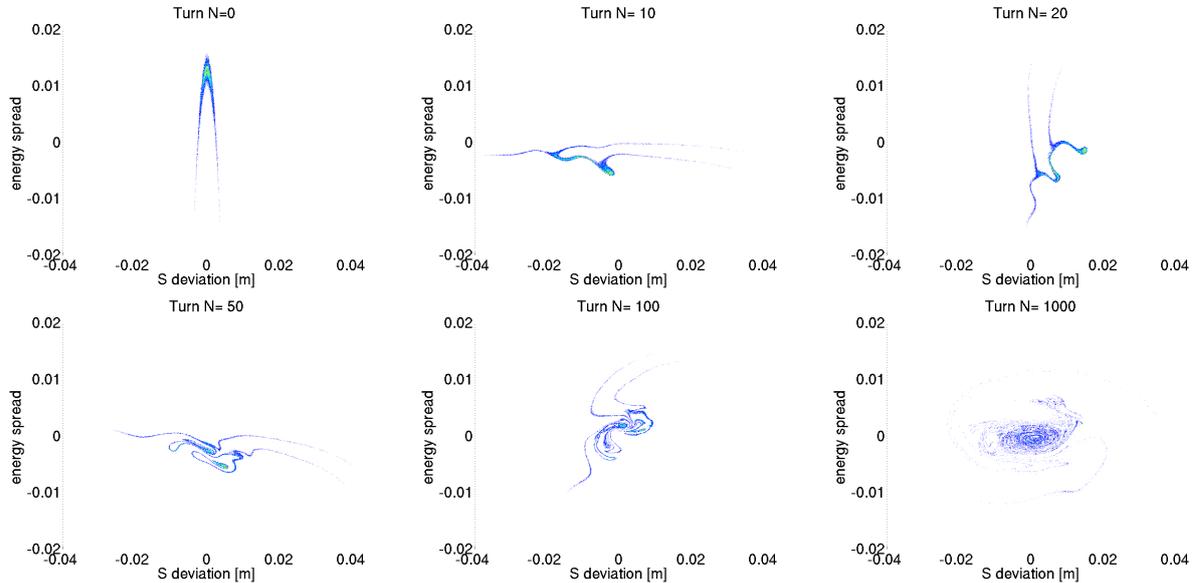

Figure 5.1: Figure taken from [62]. Evolution of the bunch in the longitudinal phase space (energy spread versus longitudinal position) as function of turn number (indicated above each image) after its injection in the ThomX ring. The color of the dots indicate the particles intensity at that location red being the most intense and green more intense than blue.

In some cases the CSR forces will be so disruptive that the bunch will break into two parts as shown on figure 5.2. As CSR depends on the charge, this beam break up effect is more intense at high charge. There is therefore a charge optimum around $0.9\,\mathrm{nC}$ as shown on figure 5.3. These findings are summarized in figure 5.4 where each effect has been turned on and off alternatively to see how they contribute to the reduction of the total X-ray flux.

Figure 5.4 also shows that some mitigation can be achieved by injecting the beam with a slight energy offset and by having a turn by turn feedback on the RF cavity phase (this is described in more details in [61]). Further mitigation strategy should be considered such as injecting a longer bunch in the ring, increasing even further its energy spread or anticipating first order phase corrections (instead of relying on phase feedback only). Unfortunately such studies were not possible over the duration of Illya's thesis but should be investigated soon.
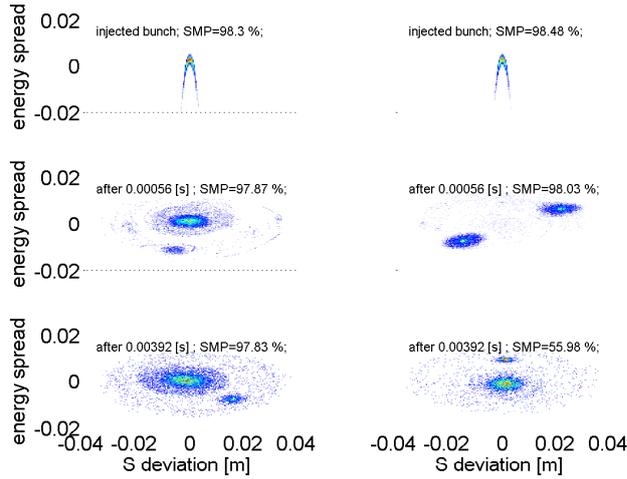
Figure 5.2: Figure taken from [62]. Longitudinal phase space of the bunch (energy spread versus longitudinal position), at injection (top), after 10 000 turns (middle) and after 70 000 turns (bottom) in two cases with the same beam parameters (but different initial random distributions of the macro particles). On the left the bunch is relatively stable and only 2% of the macro particles are lost whereas on the right the bunch is unstable and it is split in less than 10 000 turns, leading to the loss of 44% of the charge. The color of the dots indicate the particles intensity at that location red being the most intense and green more intense than blue.
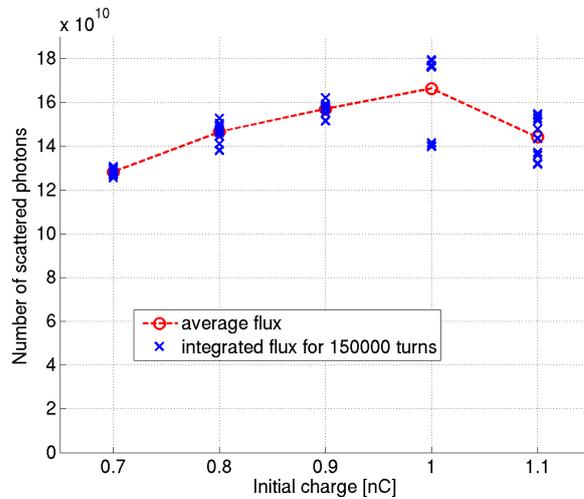

Figure 5.3: Figure taken from [62]. Average photon flux produced by ThomX for 10 simulations of 1500 000 turns each for 5 different initial charges. At 1nC and above during some simulations the beam get partially lost leading to a lower photon yield.
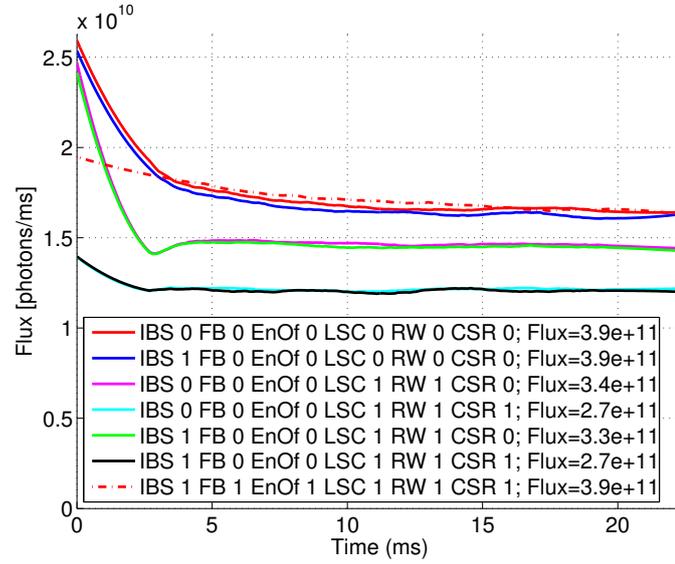
Figure 5.4: Figure taken from [62]. Photon flux as function of the turn number with various effects turned on or off. In the caption, IBS stands for Intrabeam Scattering, FB for longitudinal feedback, EnOf for Energy Offset (to compensate the beam mismatch at injection), LSC for longitudinal space charge, RW for resistive wall effect, CSR for Coherent Synchrotron Radiation. When an effect is followed by a 0 it means that it is turned off. If it is followed by a 1, it means that it is turned on in the simulations. The flux in the caption is given in number of photons (integrated over the duration of the simulation).

Chapter 6

Laser and accelerator synchronisation

Several of the projects on which I worked involved both lasers and accelerators and each time we were faced with the problem of synchronizing them. Here I describe how this was achieved.

6.1 Time reference in accelerators and in lasers

Lasers and accelerators both require to have their own internal clocks.

In the case of lasers the internal clock is the laser cavity which will determine the frequency (repetition rate) at which the pulses are produced. The length of this cavity is determined by the optical path between the mirrors (and the frequency is this length divided by the speed of light). This length (frequency) can be adjusted by having a mirror on a translation stage (long adjustment at slow rate) or a piezoactuator (short adjustments at fast rate).

In the case of accelerators the internal clock is the RF frequency of the accelerating sections or that of the ring cavity (in the case of a circular accelerator). In a ring this frequency may change due to environmental conditions such as minute changes in the temperature of the cooling water. Deviation from that frequency will lead to the beam being out of the RF acceptance and being lost. Examples of accelerator timing systems are given in [64, 65] In most accelerators with both a linac and a ring the linac frequency will follow the ring frequency although this is not always the case (and in particular this is not the case in ThomX).

6.2   The accelerator is the reference clock: Laser-wire

For the ATF laser-wire we had the opportunity to specify the laser we wanted to purchase. Hence we did specify that the laser had to have an adjustable length cavity with a range compatible with the ATF frequency changes, both slow and fast. One of the mirrors had to be mounted on a piezoactuator to follow very accurately the ATF frequency and another had to be adjustable over several millimeters to allow compensation of large frequency changes.

The noise of one electronic device with respect to another is called phase noise. Phase is often given as a power spectrum giving the "Single Side Band phase noise (SSB)" in decibels below the carrier per Hertz (dBc/Hz). The SSB must be integrated in the relevant range of frequencies to estimate its effect. Noise that occurs at too high frequencies will be smoothed out: for example a 1-GHz noise will not appear on a 75-MHz oscillator and similarly noise that is slow compared to the repetition rate of the device can also be ignored as its effect is not visible on a given shot (but it can appear when shots are compared with each others). The low frequency noise often dominates the integral, so a correct determination of the low frequency bound is more important. In the case of ThomX, the linac frequency will be $3\,\mathrm{GHz}$ and the repetition rate will be $50\,\mathrm{Hz}$ so the noise must be integrated between these two bounds.

This integrated phase noise is expressed as a power (with respect to the carrier signal). It is usual to convert this phase noise into a jitter by looking at the jitter induced by such power fluctuation on the nominal signal. Such conversion is obviously dependent on the carrier signal frequency.

The achieve the luminosity required for the ILC we estimated that the litter had to be lower than $1\,\mathrm{ps}$. This was challenging but within the reach of lasers at that time.

6.3   The accelerator and the laser have independent clocks: ThomX and ESCULAP

In ThomX the linac must be at a fixed frequency[1] (the resonance frequency of the RF-gun; $2998\,\mathrm{MHz}$) whereas the ring frequency will have to be adjusted around $500\,\mathrm{MHz}$ with temperature changes. To ensure that the electrons are accelerated in the gun and injected in the ring at the correct phase the trigger signal must be distributed at very specific moment when the phase of the two clocks are at a set coincidence as illustrated in figure 6.1.

---

[1]When I joined the project, the team in charge of the RF gun did not want to take any risk with the gun and thus would not accept any frequency change, even to follow the ring. This position has been revised recently.
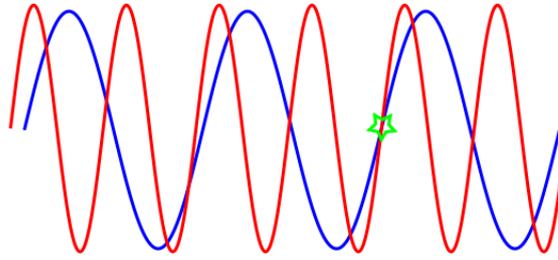
Figure 6.1: When the two clocks do not have the same frequency it is important to find common zero crossing.

A similar problem has been encountered in the ESCULAP project (described in chapter 9.1) where PHIL and Laserix have been designed independently with their own clocks. When they operate together a common trigger must be found.

Let's consider two independent clocks at approximately the same frequency (f_1 and f_2 respectively) but with a small difference ($f_2 = f_1 + \Delta_f$) . Using a frequency mixer it is possible to get the heterodyne frequencies $f_\Sigma = f_1 + f_2$ and $f_\Delta = |f_1 - f_2|$. Using a low pass filter one can keep only the low frequency component f_Δ. This frequency has the property that when it crosses zero both f_1 and f_2 also cross zero. Experimentally we have seen that the isolation between the two clocks can be improved by adding attenuators between the clocks and the mixer. The circuit that can be used for this is shown on figure 6.2.

We can use this property to determine when we want to fire a shot in the accelerator with a fixed phase with respect to both clocks. Despite the propagation of the signal in the cables this fixed phase relation with both will be kept during the pulse propagation.
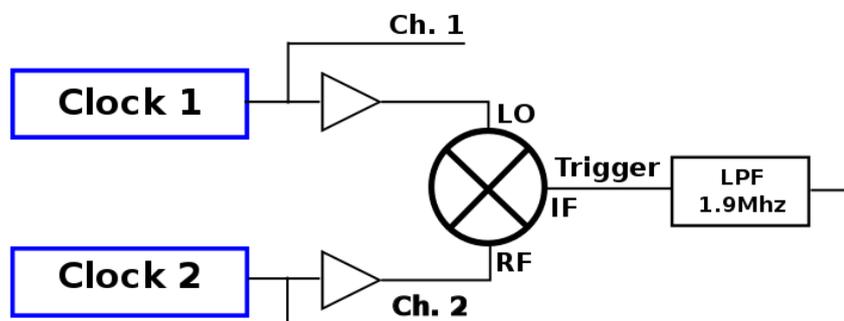

Figure 6.2: A mixer followed by a low pass filter can be used to find the common zero crossing between two clocks.

As the accuracy has to be very important it is important to look at the effect of noise on the cables. A frequency mixer used as a phase detector can deliver a signal of $8\,\mathrm{mV}$

per degree[2], thus a noise of 0.1mV (this is a conservative value) corresponds to 0.0125°. At a frequency of 75 MHz this corresponds to a jitter of 0.42 ps.

Therefore by triggering on the zero crossing at the exit of the phase detector one can be sure to be in a fixed phase relation with both clocks within 0.5 ps. Due to cable length the pulse on which the gun will fire will not be exactly the zero crossing but the gun laser itself has a fixed phase relation with the laser clock so using this setup when the laser fires it is at a fixed phase with respect to both clocks and from this reference point the triggering signal can be distributed to all the systems. The zero crossing at the exit of the low pass filter can be detected by an AD8611 that will generate a TTL pulse with very little noise added. The full setup is shown on figure 6.3. Dephasers can be used to get the correct phase relationship.
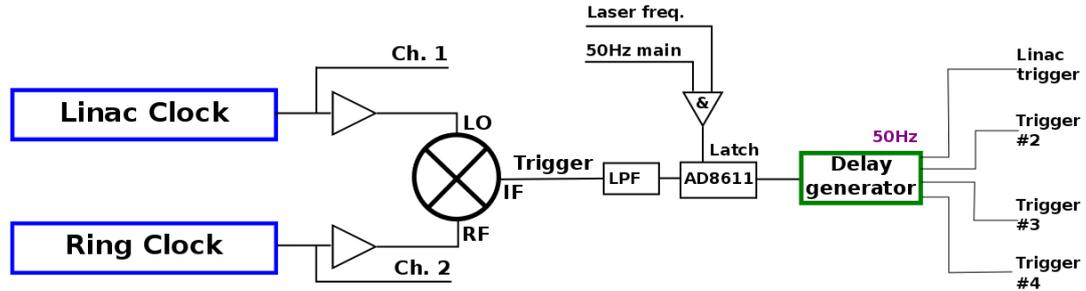

Figure 6.3: Circuit proposed to decide the triggering of the signal distribution on ThomX.

This synchronization scheme has first been tested as part of the ESCULAP project (described in section 9.1) and the results have been presented in conference [66].

Simulations taking into account the effect of the beam jitter with complex electron pulse shapes in the ThomX ring have been reported in [61].

---

[2]Here we use the ZRPD1+ from mini circuits as reference.

Part II

Advanced diagnostics and plasma acceleration

Chapter 7

Single shot emittance measurement

7.1 Motivation

The publications about the dream beams in 2004 [17, 18, 19], the Oxford-Berkeley results in 2006 [20] and the energy doubling experiment at SLAC in 2007 [30] triggered a strong interest for the beams produced by plasma acceleration, both laser-driven and beam-driven.

Starting in 2006 I decided to look at the development of advanced diagnostics to measure some of the parameters of these beams. One of the key difference between conventional beam and those produced by plasma accelerator is the reproducibility: beam produced by plasma accelerators are not as stable as those produced in conventional accelerators.

My focus has been the measurements of the transverse and longitudinal emittance of these beams. The work on transverse emittance is described in this chapter and the work on longitudinal emittance is described in the next one. In chapter 9 I will mention laser-plasma experiments in which I took part.

7.2 Transverse emittance of a laser-driven plasma accelerator

In [20] the transverse size of the beam at the source is limited by the laser size ($r_s < 35\,\mu m$). Its divergence has been measured as less than 2 mrad (r.m.s.). This gives a geometric emittance of 70 µm mrad at 1.0 GeV and a normalized emittance of 35 nm mrad.

Such transverse emittance, if confirmed, would be rather small compared to what is usually produced on conventional linacs.

However the measurement of such emittance is very difficult because, as noted by the authors of [20] the beam has a high energy and is rather unstable and therefore each shot is different.

The emittance of a beam is a measure of its quality (or of the relative movement of the electrons in the beam with respect to each other). It is the product of the beam size by its divergence at a waist and it can therefore be compared to the temperature of a gas (which is also the product of the size [volume] by the divergence [thermal agitation or pressure]).

In conventional accelerators the emittance can be measured in different ways. At low energy single shot emittance measurements can be done using the "pepper-pot" method (or numerous derivatives of it). In the pepper-pot method the beam is sampled by a plate with holes (or slits) located before an imaging screen (usually a fluorescent screen) as shown on figure 7.1. As the size of each hole is well known, the spot size measured on the screen give the divergence of each beam let coming out of the holes. By looking at these local divergences any correlation induced by not being at the waist can be removed and the transverse emittance can be measured (detailed formulas are given for example in [67]).
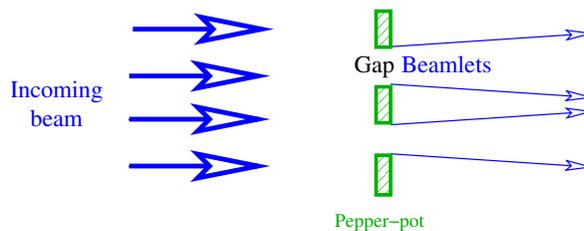

Figure 7.1: Example of a pepper-pot sampling a beam into several beamlets. The transverse emittance is given by using the hole size and the beamlets divergence measured on the screen (image taken from [68]).

At high energy the beam would easily go through the sampling plate used and therefore other methods are favored. Quadrupole scans allow to measure the transverse emittance by looking at beam size variation on a screen with the intensity of a focusing quadrupole is changed. However this requires several shots to be performed consecutively and this is not possible with an accelerator where the beam energy and pointing change from shot to shot.

A variation of the quadrupole scan method is the multiscreen method where the beam size is measured by screens (or laser-wires) in several locations along the beam trajectory. By looking at how the beam size evolves as it propagates and by using the known beam optics it is possible to calculate the beam transverse emittance. As each screen may

significantly scatter the beam this method is usually only used in accelerators where the beam is stable.

As none of the conventional emittance measurement methods were available for laser-plasma accelerators I decided to see how they could be adapted to perform such measurement. The goal being to measure the transverse emittance of high energy (several hundreds MeV) beam in a single shot. This led me to two different developments: extended pepper-pots, described in section 7.3 and Multiple OTR described in section 7.4.

7.3 Extended pepper-pot

A solution to use pepper-pot at high energies would be to increase the thickness of the plate. I decided to investigate this both theoretically and experimentally.

As I did not have any experience with pepper-pot measurements the first step was to perform some conventional pepper-pot measurements. For that purpose I used a particle accelerator available at Oxford: the 1 MeV proton Van De Graaff teaching accelerator and together with undergraduate student Michael McCann we measured the energy of the beam [69]. The pepper-pot pattern we observed is shown on figure 7.2. At the same time, I did some simulations using the GEANT4 software [70] with undergraduate student Joe Hewlett to make sure that such thick pepper-pot would still allow to measure the beam emittance [71].
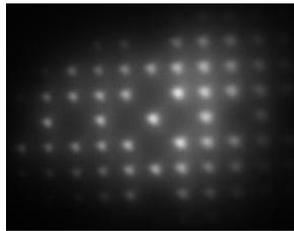

Figure 7.2: Example of pepper-pot measurement using the Oxford teaching accelerator (image taken from [69]).

Building on this initial work we decided to prepare an experimental campaign to test thick pepper-pots at high energy. For these tests we obtained beam time at the Beam Test Facility (BTF) [72, 73, 74] of the Frascati National Laboratory (INFN/LNF).

Our experiment is described in details in [75]. Here is a brief summary of the experiment as taken from that reference: For our experiment the beam line was extended by more than two metres after the final bending magnet. The pepper-pot was fitted on an actuator mounted inside a 4-way cross installed 2.2 m after the bending magnet. The pepper-pot could be inserted when emittance measurement were being made or retracted to allow for other studies to take place. A YAG screen located 230 mm after the pepper-pots was used to ensure proper alignment. The test facility vacuum ended 380 mm after

the pepper-pot with a 50 µm mylar window. The electrons were detected by a gadolinium doped screen ("Lanex regular") produced by Kodak located 200 mm beyond the mylar window. The photons emitted by the lanex screen were reflected by a 45° mirror and recorded by a camera located 672 mm away from the screen. The lens fitted on this camera was focussed on the lanex screen. This arrangement allowed the camera to be out of the accelerator plane and shielded from the radiation by lead bricks. The layout of the experiment is shown on figure 7.3.
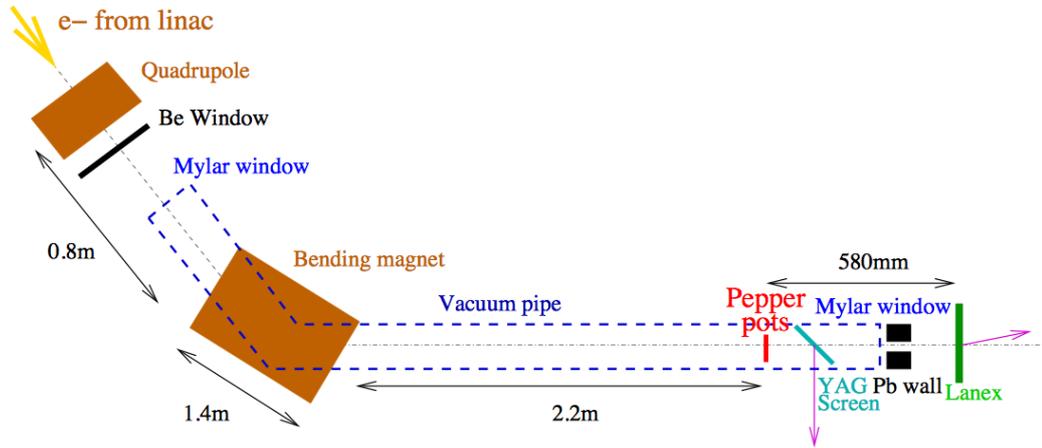

Figure 7.3: Layout of the pepper-pot experiment at the BTF as shown in [75].

A picture of the pepper-pot used is shown on figure 7.4 and example of the data measured during that experiment are shown in figure 7.5.

Figure 7.4: Picture of the pepper-pot used at the BTF as shown in [75].

The success of this experiment led us to plan a similar experiment in the transfer line from the booster to the synchrotron of the DIAMOND Light Source. At that location the beam could reach an energy of up to 3 GeV and we performed experiments at 2 GeV and 3 GeV. The observed pattern and the stability of the measurement are shown on
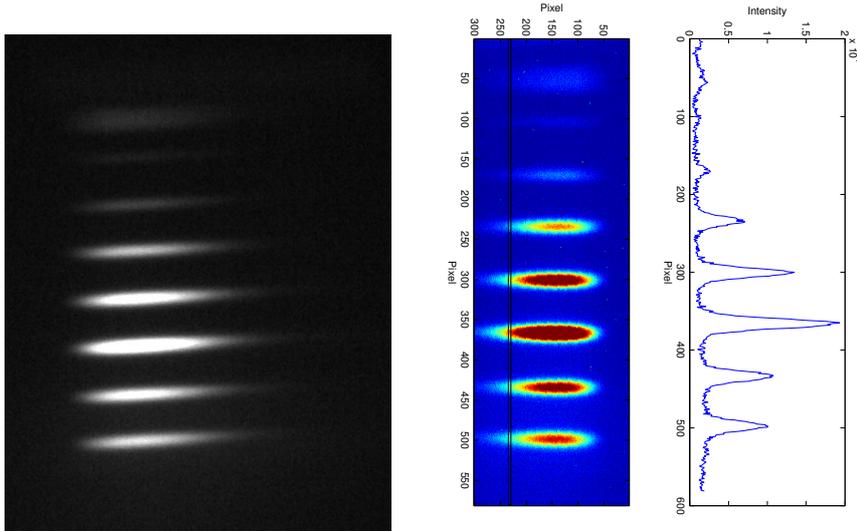
Figure 7.5: Example of pepper-pots measurements similar to those reported in [75]. Left: image recorded by the camera. Right: False colors image and slits profiles.

figure 7.6. These results have been published in [76].

I also investigated how to apply this technique to protons with measurements on LINAC2 at CERN however the lack of time before changing job did not allow me to release the results of these measurements.

One of the concerns with that technique expressed several times during conferences was that the length of the pepper-pot channel might biais the emittance measurement. To validate my approach I made several calculations and GEANT4 simulations. The calculations have been published in [68] and I reproduce below the main arguments taken from [68] and encourage the interested reader to refer to the full publication.

The main problem of using a pepper-pot as diagnostic for transverse emittance measurement of high energy particles, arises from the thickness of material required to give sufficient contrast between the beam passing through the hole and the stopped beam. The thickness of material needed to stop electrons with an energy of several hundreds of MeV is quite large. Although one radiation length is enough to absorb in average all but $1/e$ of the electrons' energy [77], the GEANT4 [70] simulations shown in figure 7.7 indicate that several additional radiation lengths are required to stop most of the electronic shower. Therefore, a pepper-pot able to measure the transverse emittance of a beam of several hundred MeV electrons must have a significant longitudinal extent (figure 7.8) and one may question how the acceptance of the pepper-pot is modified by this length.
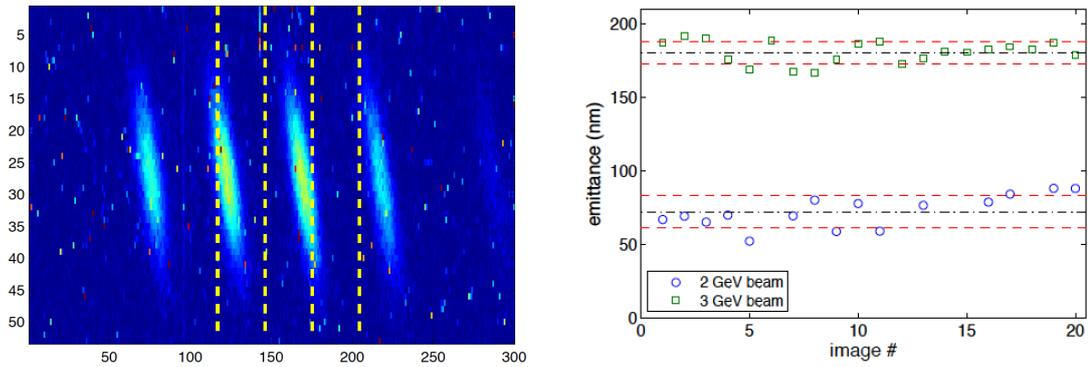
Figure 7.6: Pepper pot measurement at the DIAMOND Light Source as reported in the booster to synchrotron line with a beam energy of 2 GeV and 3 GeV. Left: image recorded by the camera. Right: transverse emittance calculated shot by shot on several images. Images taken from [76].

The figure 7.9 shows how the phase-space evolves as a bunch of particles propagates through a long pepper-pot and figure 7.10 shows GEANT4 simulations validating the work. The conclusions of these calculations were that provided that the parameters are chosen correctly (and the constraints on such choice are not too stringer) it is valid to use an extended pepper-pot to measure the transverse emittance of a high energy beam.

7.4 Multiple OTR measurement to measure the transverse emittance of a beam

As the energy of the beam gets higher the thickness of material required to stop the beam will be larger so a different technique had to be found. I decided to look for a solution to perform multiple screen emittance measurement with each screen setup so that its disturbance of the beam is negligible. This is possible using Optical Transition Radiation (OTR)[78, 79] : as it is a surface effect, it does not depend on the thickness of the material used. The first condition to validate this idea of single shot transverse emittance measurement using multiple OTR screens was to check what would be the impact of several screen on the emittance and, reciprocally what would be the maximum acceptable thickness for such measurement.

I reproduce below the text of an unpublished note written to make the estimates, some of which was latter included in a publication [80]. This note was written with the help of Cyrille Thomas and Riccardo Bartolini who were both at the Diamond Light Source at that time.

For our calculations we use the layout shown on figure 7.11: 3 screens located 0.5 m
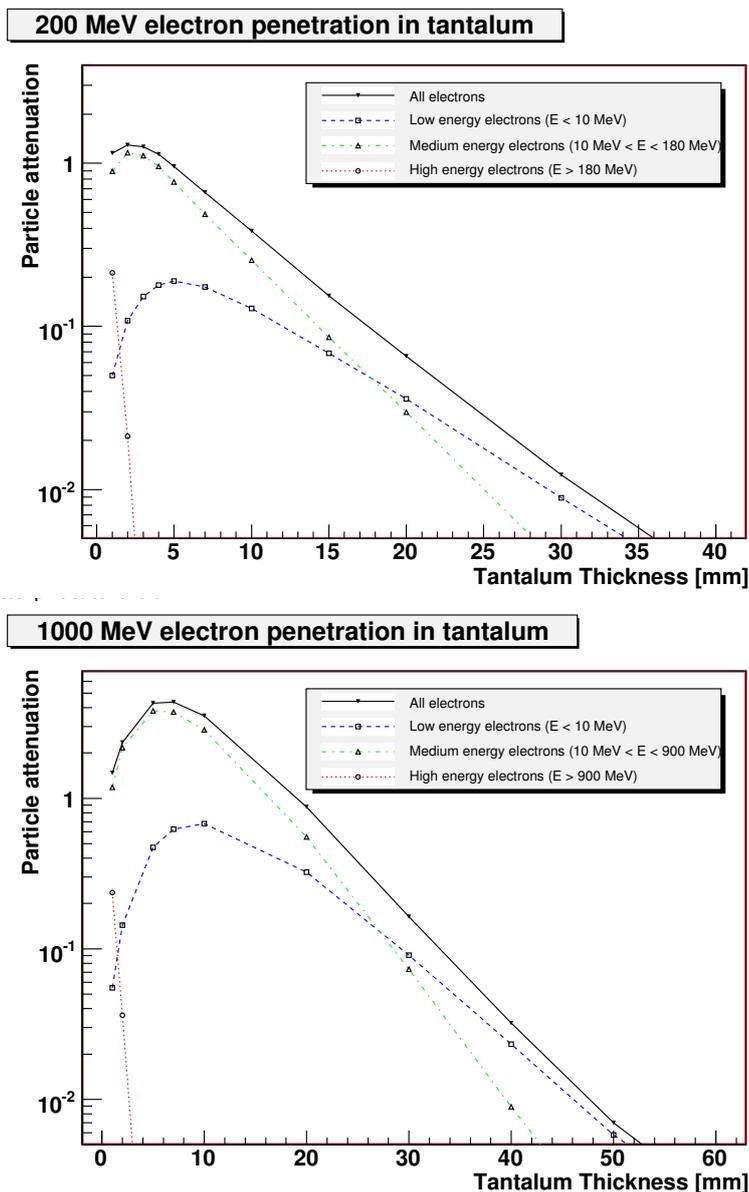
Figure 7.7: GEANT4 [70] simulations of the penetration of high energy electrons in a block of Tantalum. The horizontal axis gives the penetration depth and the vertical axis gives the number of electrons remaining at that depth for one initial electron. The red lines (round markers) correspond to high energy electrons whereas the blue lines (square markers) and the green lines (up-pointing triangular markers) correspond to lower energy particles emitted by the initial particle. The black lines (down-pointing triangular markers) show the total number of electrons remaining. The plot on the top corresponds to 200 MeV electrons and the one on the bottom to 1 GeV electrons. Figure taken from [68].
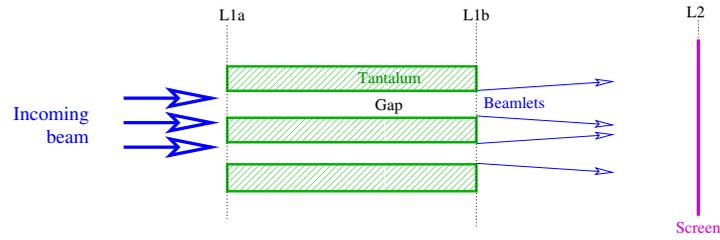
Figure 7.8: Example of a "extended" pepper-pot sampling a beam into several beamlets. The transverse emittance is given by using the hole size and the beamlets divergence measured on the screen (image taken from [68]).
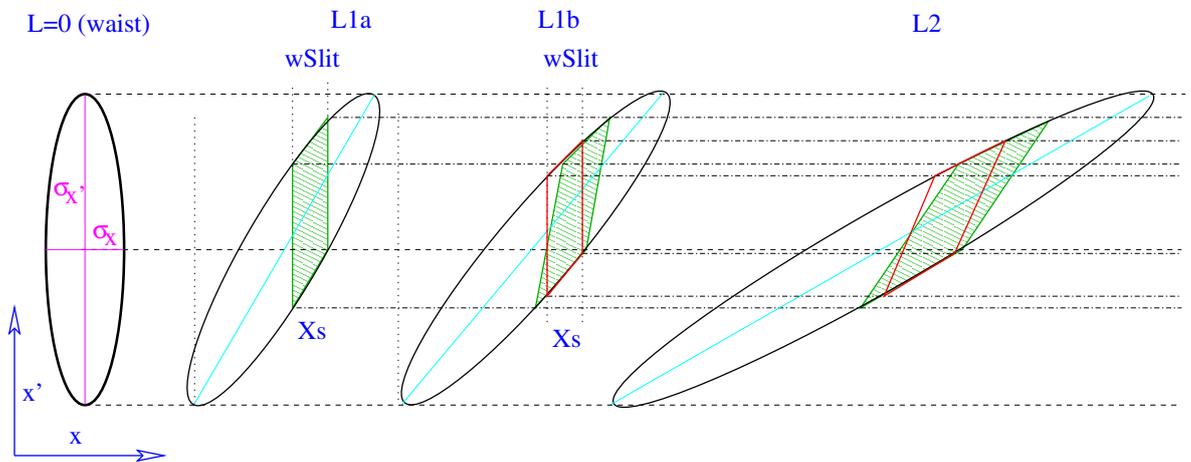

Figure 7.9:   Long pepper-pot: Evolution of the phase-space as the beam drifts. At the source or at a wait ($L = 0$) the phase space of the beam is first represented by an upright ellipse. As the beam drifts the ellipse gets sheared. At L_{1a} the beam enters a slit and thus only the particles in the green area pass the slit. While the beam travels in the slit the ellipse is further sheared, hence at L_{1b}, the exit of the slit, the area of phase space within the slit acceptance (red box) is different from that occupied by the particles sampled at the entrance of the slit. Hence the full acceptance of the slit correspond to the overlap between the green and the red areas. Figure taken from [68]. The variables definition is given in [68].

$\Delta L_{ba} = 10\,\text{mm};\ \frac{\mathcal{A}_s - \mathcal{A}_o}{\mathcal{A}_o} = 4.5\%$ $\Delta L_{ba} = 50\,\text{mm};\ \frac{\mathcal{A}_s - \mathcal{A}_o}{\mathcal{A}_o} = 22.5\%$

$\Delta L_{ba} = 100\,\text{mm};\ \frac{\mathcal{A}_s - \mathcal{A}_o}{\mathcal{A}_o} = 45\%$ $\Delta L_{ba} = 200\,\text{mm};\ \frac{\mathcal{A}_s - \mathcal{A}_o}{\mathcal{A}_o} = 90\%$
$w_{\text{slit}} = 50\,\mu\text{m};\ \sigma_x = 50\,\mu\text{m}\ ;\sigma_{x'} = 0.5\,\text{mrad};$
$L_{1a} = 1\,\text{m};\ L_2 = 1.5\,\text{m};\ 1\,\text{GeV};\ 100\,000\ \text{electrons}$
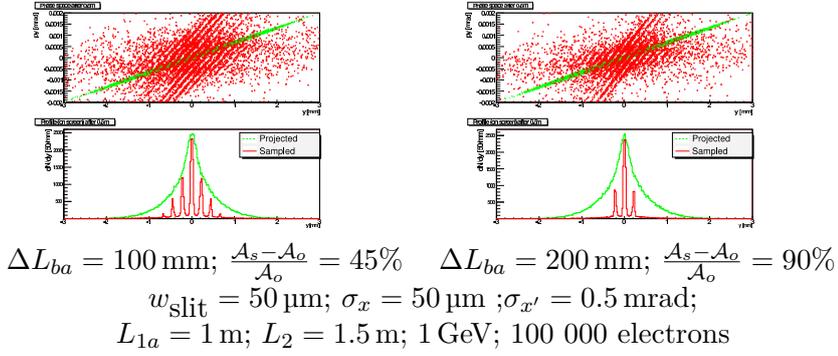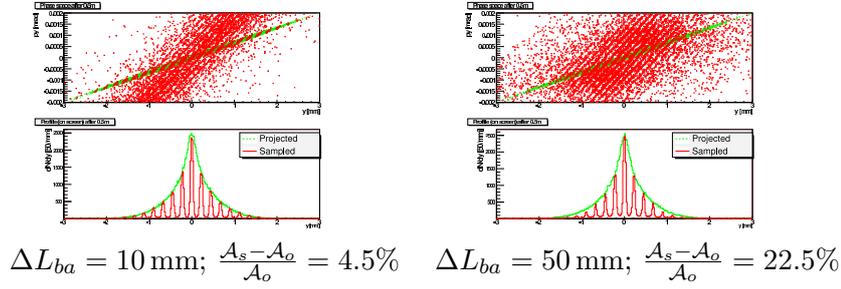
Figure 7.10: Reconstruction of the transverse phase space of a beam sampled by a long pepper-pot. In each pair of plots the top plot shows in green the original phase space of the electrons and in red the phase space of the electrons after the pepper-pot. In each pair the bottom plot shows the projection along the spatial component of the transverse phase space. In all these plots the beam energy is 1 GeV. The slit width is 50 μm, the beam size at the waist is 100 μm with a divergence of 1 mrad and the pepper-pot are located 1 m away from the beam waist. The screen is located 500 mm after the pepper-pot. For each plot 100 000 electrons were simulated with GEANT4. The top left pair of plots corresponds to a pepper-pot length of 10 mm, the top right pair of plots corresponds to a pepper-pot length of 50 mm, the bottom left pair of plots corresponds to a pepper-pot length of 100 mm and the bottom right pair of plots correspond to a pepper-pot length of 200 mm. For each plot the value of $\frac{\mathcal{A}_s - \mathcal{A}_o}{\mathcal{A}_o}$ as defined in [68] is given. High energy photons (X-rays) are not shown on this figure. Figure taken from [68].

apart from each other followed by a 4th screen located 1 m beyond the 3rd screen.
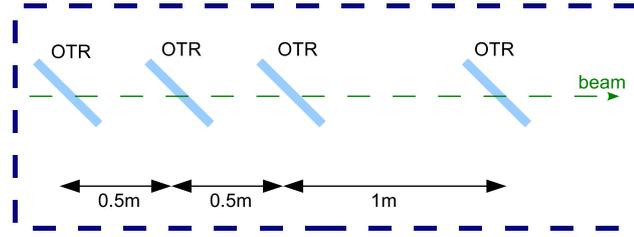

Figure 7.11:   Screen layout used in the calculations of multiple OTR single shot emittance measurement.

7.4.1   Beam propagation in a drift space

In a drift space the beam (σ) size evolves as [81]:

$$\sigma(s) = \sqrt{\epsilon(\beta_0 - 2\alpha_0 s + \gamma_0 s^2)} \tag{7.1}$$

where s is the position in the drift space, α_0, β_0 and γ_0 are the Twiss parameters at $s = 0$ and ϵ is the beam emittance.

When $s = 0$ is a symmetry point (waist), this can be rewritten as

$$\sigma(s) = \sqrt{\epsilon\beta_0 + \frac{\epsilon}{\beta_0}s^2} \tag{7.2}$$

hence

$$\sigma^2(s) = \epsilon\beta_0 + \frac{\epsilon}{\beta_0}s^2 \tag{7.3}$$

By measuring σ with an OTR screen at 3 (or more) locations around a waist it is thus possible to make a parabolic fit giving the Twiss parameters of the beam as well as ϵ and β_0. Equation 7.3 shows that a linear fit of s^2 versus the beam sizes squared will also give the beam emittance.

7.4.2   Beam expansion condition

In such drift space the beam divergence is (with a different sign on either side of the waist)

$$\sigma' = \pm\sqrt{\frac{\epsilon}{\beta}} = \pm\frac{\epsilon}{\sigma_0} \tag{7.4}$$

with σ_0 the beam size at the waist.

The beam size at a given distance s from the waist will be related to the beam size at the waist by the following relation:

$$\begin{aligned}
\frac{\sigma(s)}{\sigma_0} &= \frac{\sqrt{\epsilon\beta_0 + \frac{\epsilon}{\beta_0}s^2}}{\sqrt{\epsilon\beta_0}} \\
&= \sqrt{1 + \frac{s^2}{\beta_0^2}}
\end{aligned} \tag{7.5}$$

Using $\beta_0 = \frac{\sigma_0^2}{\epsilon}$, this becomes:

$$\frac{\sigma(s)}{\sigma_0} = \sqrt{1 + \frac{\epsilon^2 s^2}{\sigma_0^4}} \tag{7.6}$$

Hence for a 1 mm.mrad beam with a 1 mm spot size, the beam will have increased by 10% beam at $s = 0.45$ m and by 20% at $s = 0.66$m. For the same beam with a 5mm spot size, these distances are multiplied by 25 and become $s = 11.46$m and $s = 16.6$m.

7.4.3   Effect of the scattering in the screens on the beam expansion

An electron traversing nuclear matter will be Coulomb scattered. Most of these scattering will be at very small angle but will add up as the electron progresses through the matter. The phenomena is described in details in [77].

For a bunch of electron, the scattering experienced after traversing a layer of thickness x can be approximated by a Gaussian of width[82]:

$$\theta_0 = \frac{13.6 \text{ MeV}}{\beta c p}\sqrt{\frac{x}{X_0}}\left[1 + 0.038 ln\left(\frac{x}{X_0}\right)\right] \tag{7.7}$$

where βc is the velocity of the electrons, p their momentum and X_0 a quantity called the radiation length and which expresses how high energy electrons loose their energy in a given material[1].

---

[1]The radiation length is the mean distance over which a high-energy electron looses all but $1/e$ of its energy by Bremstrahlung[77].

To make it easier to estimate the scattering as a function of the momentum this equation can be rewritten as

$$p\theta_0 = \frac{13.6 \text{ MeV}}{\beta c}\sqrt{\frac{x}{X_0}}\left[1 + 0.038 ln\left(\frac{x}{X_0}\right)\right] \tag{7.8}$$

Table 7.1 shows that the electrons will travel only a small fraction of a radiation length (X_0) in each type of screen considered. A scattering factor $p\theta_0$ of the order of a hundred MeV.mrad means that a beam with an energy of a hundreds MeV will be scattered by about one milliradian. Among the different screens considered, Mylar and Kapton (Polyimide film) introduce the lower scattering and thinner films seems available.

Material	Radiation Length (X_0)	Thickness $10^{-4} X_0$	Scattering $p\theta_0$	Limit σ_0 (eq. 7.13) $\frac{1\text{mm.mrad}}{\theta_0}$
Aluminium (10 μm)	8.9 cm	1.12	139 MeV.mrad	0.9 mm
Aluminium (30 μm)	8.9 cm	3.37	242 MeV.mrad	0.5 mm
Mylar (2 μm)	28.6 cm	0.069	34 MeV.mrad	3.7 mm
Mylar (5 μm)	28.6 cm	0.17	55 MeV.mrad	3.7 mm
Polyimide film (7.5 μm)	28.6 cm	0.26	66 MeV.mrad	1.9 mm
Polyimide film (10 μm)	28.6 cm	0.34	77 MeV.mrad	1.6 mm
Mylar (10 μm)	28.6 cm	0.34	77 MeV.mrad	1.6 mm
Air (2 m), 1 atm.	3 10^4 cm	66.67	1089 MeV.mrad	-
Air (2 m), 0.01 atm.	3 10^6 cm	0.67	107 MeV.mrad	-

Table 7.1: Nuclear properties of various materials [77] for different thicknesses. The last column is for a 500 MeV beam with a transverse emittance of 1.mm.mrad.

When the beam scatters on the screens an additional scattering term is required and equation 7.1 is approximately modified as follow:

$$\sigma(s) = \sqrt{\epsilon(\beta_0 - 2\alpha_0 s + \gamma_0 s^2) + \sum_{i=1}^{N(s)\text{screens}} (s - s_i)\theta_i^2} \tag{7.9}$$

where $N(s)_{\text{screens}}$ is the number of screens located upstream from the position at which the measurement is performed, s_i their position and θ_i the scattering they induce.

Assuming that all screens are made of the same material with a scattering coefficient θ_0, the scattering induced by the first screen will dominate:

$$\sum_{i=1}^{N(s)\text{screens}} (s - s_i)\theta_i \simeq (s - s_1)\theta_0 \tag{7.10}$$

A measurement of the beam size dominated by the term $(s - s_1)\theta_0$ will provide information on the scattering but not on the emittance of the beam. Hence the screens, their position and the beam optics must be chosen so that in all measurements the scattering can be neglected.

This requires:

$$\frac{\epsilon}{\sigma_0} s > N_{\text{screens}}\theta_0(s - s_1) \tag{7.11}$$

where N_{screens} is the total number of screens used.

Assuming that the first screen is close from the waist and hence $s - s_1 \simeq s$, this can be rewritten as:

$$\frac{\epsilon}{\sigma_0} >> N_{\text{screens}}\theta_0 \tag{7.12}$$

$$\sigma_0 << \frac{\epsilon}{N_{\text{screens}}\theta_0} \tag{7.13}$$

Equation 7.13 can be rewritten as

$$\sigma_0 << N_{\text{screens}}\frac{\epsilon_n}{\gamma\frac{p\theta_0}{p}} \tag{7.14}$$

$$\sigma_0 << N_{\text{screens}}\frac{mc\epsilon_n}{p\theta_0} \tag{7.15}$$

where ϵ_n is the normalised emittance, γ the Lorentz transformation factor and c the speed of light.

This shows that the requirement on σ_0 as a function of the normalised emittance and of $p\theta_i$ is independent of the beam energy (but the ease of achieving a given σ_0 may be different).

At 500 MeV a 7.5μm polyimide film screen will induce a scattering $\theta_i = 0.13$mrad. With an emittance $\epsilon = 1$mm.mrad, equation 7.13 requires $\sigma_0 << 7.6$mm. The limit value of σ_0 as given by equation 7.13 assuming $N_{\text{screens}} = 4$ for various screen materials is given in table 7.1.

When the spot size is chosen so that equation 7.13 is satisfied the scattering can be neglected, it is the case with thin Mylar or kapton screens .

7.4.4   Simulations

Mathematica

Simple simulations of such measurement have been done using Mathematica. In these simulations 4 screens were positioned at $s = -0.5m$, $s = 0m$, $s = 0.5m$ and $s = 1.5m$. The propagation of a beam with a given emittance and beta function was then calculated and the size of the beam at each screen was estimated with some noise added. To take into account the limited pixel size the measured beam size was rounded to the size of the pixels.

If the beam optics or the beam energy is not well understood the beam waist may not be positioned exactly where it is expected to be, this was included in our simulations.

Equation 7.2 was fitted to the beam sizes found and from this fit the value of the emittance was deducted. With the beam sizes used it is assumed that the effect of the scattering can be neglected as the natural beam divergence is much bigger than the divergence induced (equation 7.13).

Figure 7.12 shows a few example of such fits.

Figure 7.13 shows the difference between the deducted emittance and the real emittance for several simulation runs.

Figure 7.14 shows the difference between the deducted emittance and the real emittance for several simulation runs where the waist position has been varied. These simulations show when the actual waist is far from $s = 0$ the performances of the fit are significantly degraded.

Geant4

To better simulate the effect of the scattering in the screens we have used the Geant4 Toolkit [70].

We have used the Geant Low Energy Physics processes [83]. These processes are valid from 250 eV to 100 GeV[84] and so completely cover the range of energies we are interested in.

This work was in particular done thanks to the contribution of undergraduate student Joe Hewlett. In our simulations the electrons were fired from a source on screens placed 0.5 m, 1.0 m, 1.5 m and 2.5 m after the source. The initial direction of the electrons was so that they formed a 2 mm waist 1 m after the source. A 10 µm-thick Mylar window was located 1 mm after the electron source.

The position at which the electrons traversed each screen as well as intermediate detectors was recorded. For each simulation more approximately 10 000 electrons were fired.
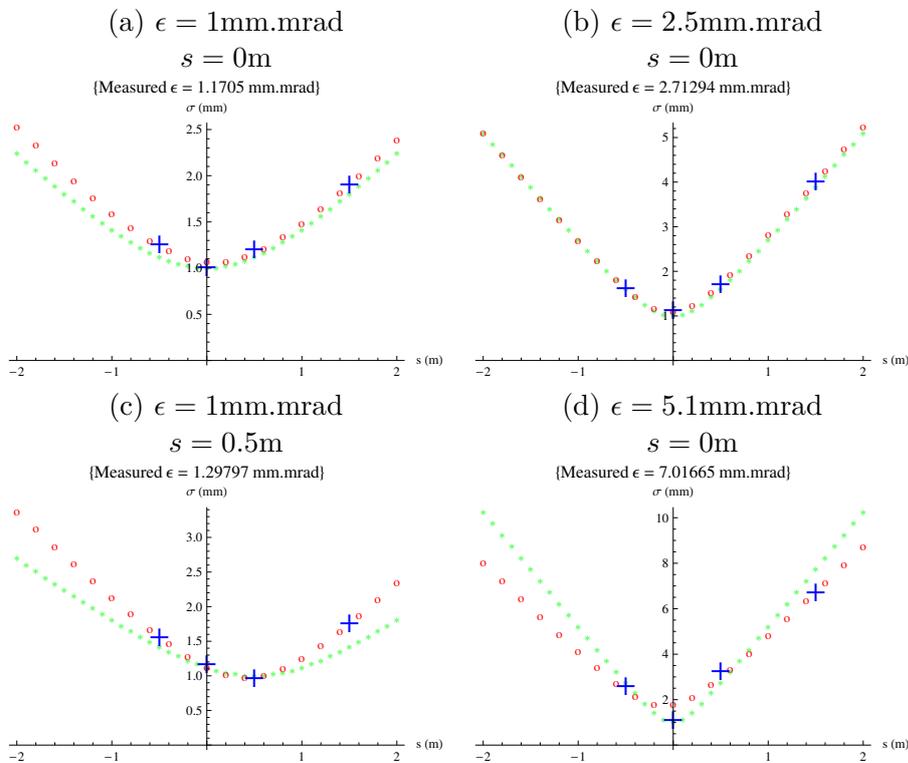
Figure 7.12: Simulated (small green dots), measured (blue crosses) and fitted (red circles) beam sizes (σ) around the waist. The beam transverse emittance (ϵ) and waist offset (s) is indicated above each plot. The waist size is always assumed to be 1 mm and the pixel size $20\mu m$. The screens used are assumed to satisfy equation 7.13 and thus the effect of the scattering is neglected in these plots.
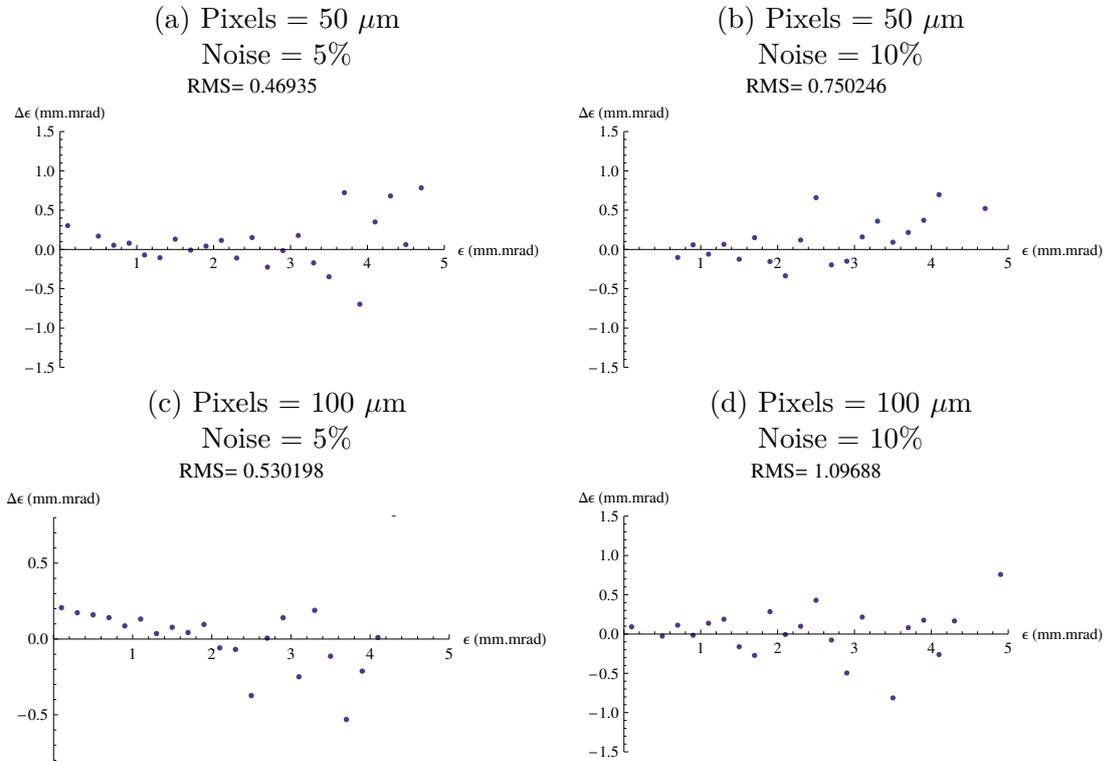
Figure 7.13: Error on the emittance measurement as a function of the beam emittance for beams forming a 1 mm waist at $s = 0$. In plots (a) and (b) the pixel size is 50 μm and in plots (c) and (d) it is 100 μm. For plot (a) and (c) the error on the beam size measurement is 5%, for plot (b) and (d) it is 10%. The screens used are assumed to satisfy equation 7.13 and thus the effect of the scattering is neglected in these plots.
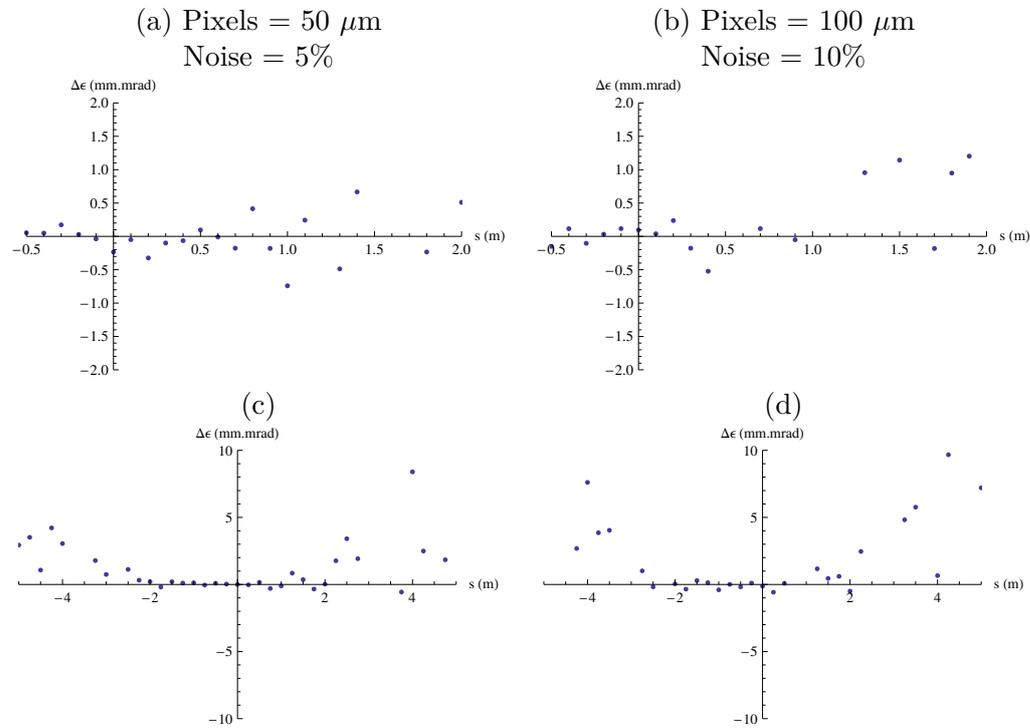
Figure 7.14: Error on the emittance measurement as a function of the position of the beam waist for beams with an emittance of 1 mm.mrad forming a 1 mm waist at the indicated position. In plot (a) and (c) the pixel size is 50 μm and the noise is 5%. In plot (b) and (d) the pixel size is 100 μm and the noise is 10%. Plot (c) and (d) repeat plat (a) and (b) over a longer range. The screens used are assumed to satisfy equation 7.13 and thus the effect of the scattering is neglected in these plots.

Emittance measurement   To study the effect of the scattering in the screens several simulations were done using different materials and thicknesses for the screens. Some of the simulations for beams of 200 MeV are shown in figure 7.15 and for 500 MeV beam in figure 7.16. As one can see on the figures the use of thin Mylar screens leads to better results than with Aluminium. Furthermore thin Mylar films are easier to handle.

The previous studies assumed that the beam waist was located on the second screen. Figure 7.17 shows that the emittance can still be reconstructed with a reasonable accuracy when the waist is elsewhere (between the screens).

Commercially we found some $2\mu m$-thick Mylar coated with a 10nm layer of Aluminium. Neglecting the scattering in the aluminium, the emittance fit can be seen on figure 7.18.

7.4.5   Feasibility of transverse emittance measurement based on multiple OTRs

Based on our study we concluded that introducing simultaneously 4 screens in a beam line could be used to fit the Twiss parameters of an electron beam in a single shot measurement. We have shown that by using $2\mu m$-thick Mylar screen such fit would lead to a measurement of the beam transverse emittance correct within 15% for a 500 MeV beam and within 30% for a 200 MeV beam.

7.4.6   Experimental tests

Following this note we attempted to demonstrate such measurements at the same time than the extended pepper-pot described in section 7.3. The first tests were done at the Beam Test Facility at INFN/LNF (see image 7.19) using the beam line shown on figure 7.4.6. Although this validated the principle the experiment had some data acquisition issue due to computers synchronism and we decided to repeat it at the Diamond Light Source and the results of that experiment have been published in [80].

The most important check to validate our method was to demonstrate that the beam size on the final screen was not affected by the insertion of other screens. This was done by measuring the beam size on the fourth screen (OTR4) with different configurations of the other three screens as shown on figure 7.21. As can be seen on that image no change in beam size was seen in x and a 5% change was seen in y. Using the beam size measured on each of the four screen it was then possible to measure the emittance. The beamline where the screens were installed had a non zero dispersion and this effect had to be taken into account as described in [80]. Using this method we found a transverse emittance $\epsilon_x = 160.1\,\mathrm{nm\,mrad} \pm 11.5\,\mathrm{nm\,mrad}$ in very good agreement with the emittance measured by a quadrupole scan performed immediately after and that gave an emittance of $\epsilon_x = 162\,\mathrm{nm\,mrad}$.
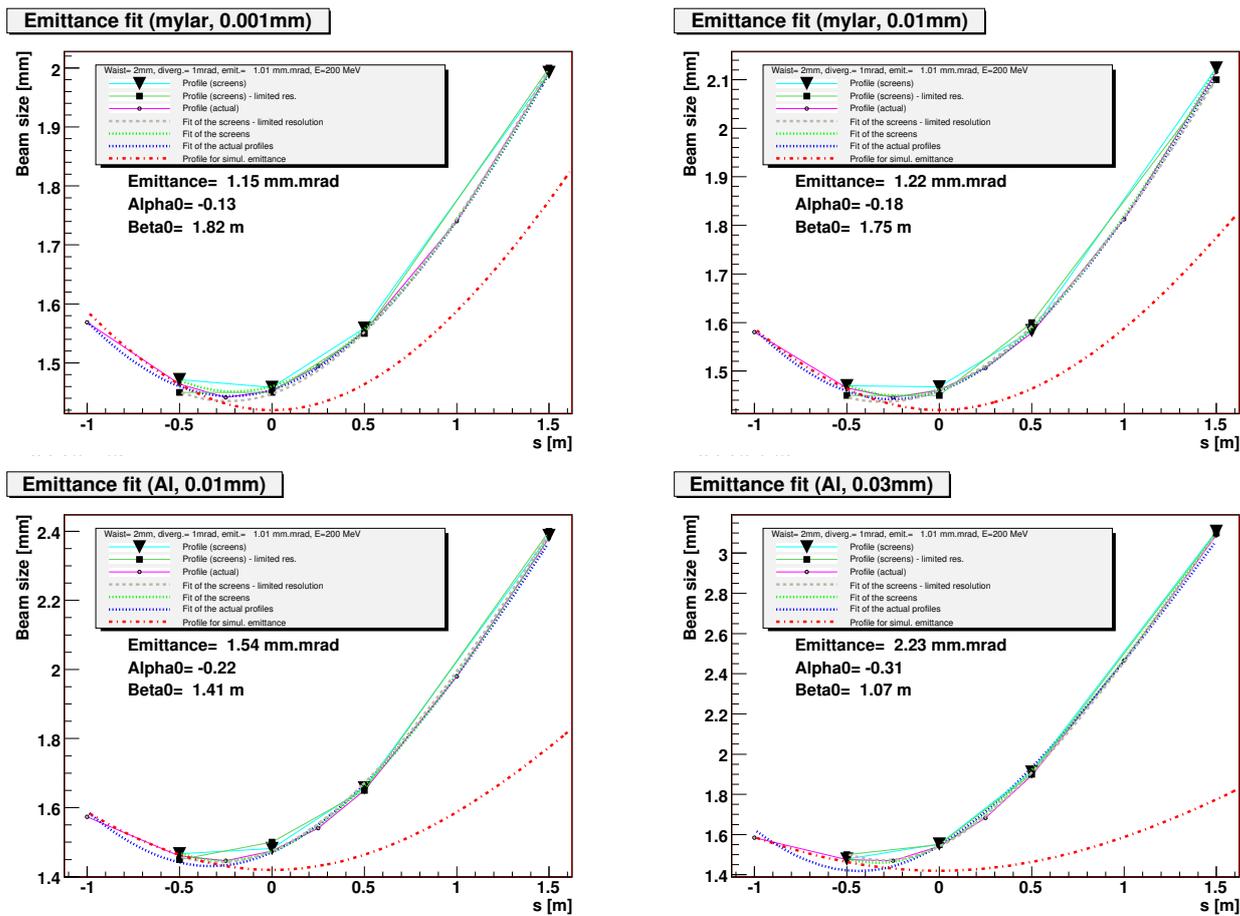
Figure 7.15: Scattering induced in a 200 MeV for various screen material and thickness with an initial emittance of 1mm.mrad. The screens material and thickness is given in the plot title. The black squares show the beam size observed on each screen, the black triangles show the beam size rounded to the nearest 50 μm (to simulate what is observed by a camera with a limited pixel size). The open circles are the position measured at additional intermediate positions. The dashed brown line shows the emittance fit made using the black triangles. The dashed green line shows the emittance fit made using the black square. The dashed green line shows the emittance fit made using the open circles. The dashed red line is the theoretical profile of the beam assuming $\alpha_0 = 0$, $\beta_0 = 2.0m$ and $\epsilon = 1.01mm.mrad$. The values given on the plot below the legend for the emittance, α_0 and β_0 are those extracted from the fit on the beam sizes with limited pixel size.

Figure 7.16:   Scattering induced in a 500 MeV for various screen material and thickness with an initial emittance of 1mm.mrad. The screens material and thickness is given in the plot title. The black squares show the beam size observed on each screen, the black triangles show the beam size rounded to the nearest 50 μm (to simulate what is observed by a camera with a limited pixel size). The open circles are the position measured at additional intermediate positions. The dashed brown line shows the emittance fit made using the black triangles. The dashed green line shows the emittance fit made using the black square. The dashed green line shows the emittance fit made using the open circles. The dashed red line is the theoretical profile of the beam assuming $\alpha_0 = 0$, $\beta_0 = 2.0m$ and $\epsilon = 1.01mm.mrad$. The values given on the plot below the legend for the emittance, α_0 and β_0 are those extracted from the fit on the beam sizes with limited pixel size.

Figure 7.17: Scattering induced in a 500 MeV for $10\mu m$-thick Mylar screens for a 500 MeV beam with an initial emittance of 1mm.mrad when the waist is not located on the second screen. The waist position is given above the plot. The black squares show the beam size observed on each screen, the black triangles show the beam size rounded to the nearest 50 μm (to simulate what is observed by a camera with a limited pixel size). The open circles are the position measured at additional intermediate positions. The dashed brown line shows the emittance fit made using the black triangles. The dashed green line shows the emittance fit made using the black square. The dashed green line shows the emittance fit made using the open circles. The values given on the plot below the legend for the emittance, α_0 and β_0 are those extracted from the fit on the beam sizes with limited pixel size.

Criticism: OTR interferences

When we first proposed this experiment some colleagues warned us that according to [85] we would face difficulties due to interferences between the screens as they were located in the pre-wave zone of each other.

The so-called pre-wave zone is the area located with a distance $L_{\text{pre-wave}} = \lambda\gamma^2$ of a source of radiation produced by electrons. In our case $L_{\text{pre-wave}} \simeq 18\,\text{m}$. In the pre-wave the forward radiation from one screen can interfere with the backward radiation from the downstream screen and this should produced an interference effect. It should be noted that this interference effect is very sensitive to the observed wavelength.

As can be seen on figure 7.22 we did not see this effect. Further worked on these interferences has been presented in 2015 and confirmed that our setup was not subject to such interferences [86] as our images were integrated over a large number of wavelengths.

To put a final conclusion on this matter I also proposed, together with a colleague, another OTR interference experiment [87] that should be conducted in a few months at CLIO and that will study the conditions under which we conditions the pre-wave effect is observable.
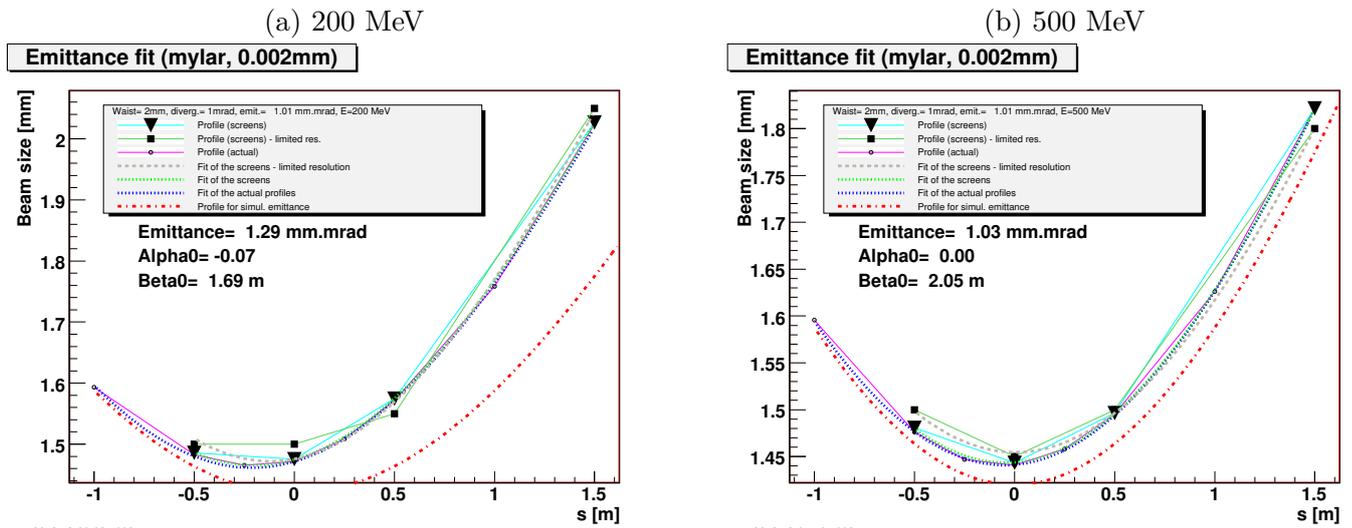
(a) 200 MeV

(b) 500 MeV

Figure 7.18:   Emittance fit using $2\mu m$-thick Mylar screens at 200 MeV (a) and 500 MeV (b). The black squares show the beam size observed on each screen, the black triangles show the beam size rounded to the nearest 50 μm (to simulate what is observed by a camera with a limited pixel size). The open circles are the position measured at additional intermediate positions. The dashed brown line shows the emittance fit made using the black triangles. The dashed green line shows the emittance fit made using the black square. The dashed green line shows the emittance fit made using the open circles. The dashed red line is the theoretical profile of the beam assuming $\alpha_0 = 0$, $\beta_0 = 2.0m$ and $\epsilon = 1.01mm.mrad$. The values given on the plot below the legend for the emittance, α_0 and β_0 are those extracted from the fit on the beam sizes with limited pixel size.


Figure 7.19: The multiple OTR and pepper-pot test beam line during a test installation at the Diamond Light Source before its shipment to Frascati.
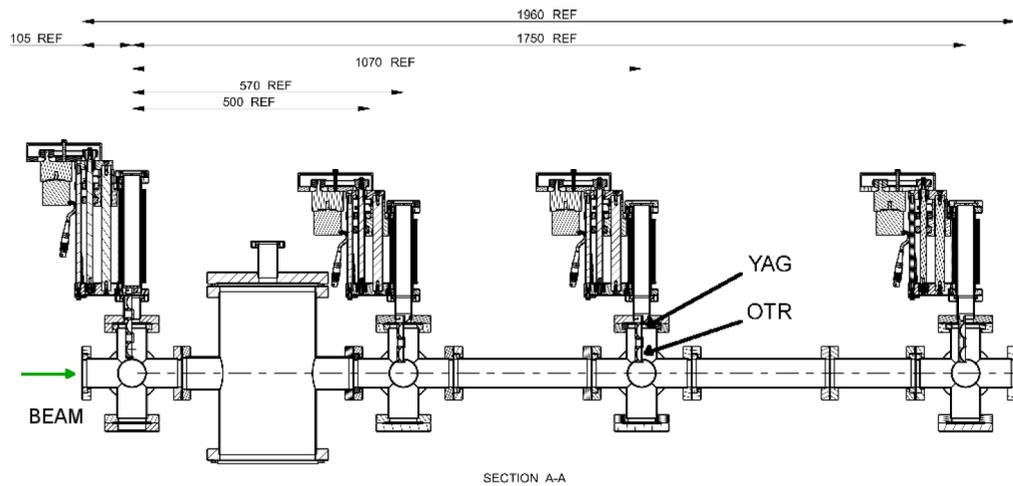
Figure 7.20: Drawing of the multiple OTR and pepper-pot test beam line that has been used both at Frascati's Beam Test Facilty and at the Diamond Light Source. Image taken from [80].
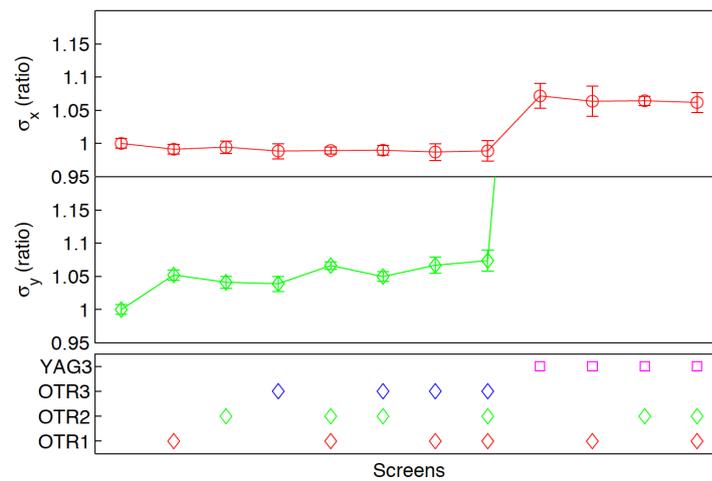

Figure 7.21: Beam size on the fourth OTR screen during the Diamond Tests as function of the screens inserted upstream. We can see that the effect of the upstream screens on the beam size measured on the lat screen is negligible in x and about 5% in y as was expected from our calculations. Image taken from [80].
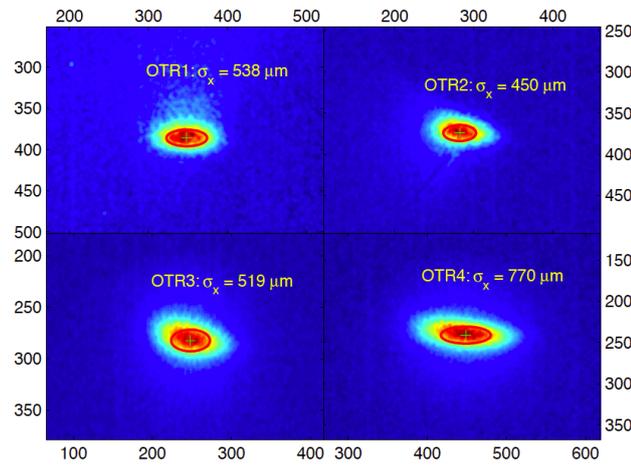
Figure 7.22:   Beam size on the fourth OTR screen during the Diamond Tests as function of the screens inserted upstream. We can see that the effect of the upstream screens on the beam size measured on the lat screen is negligible in x and about 5% in y as was expected from our calculations. Image taken from [80].

7.5   Other techniques: Emulsion based measurement and masked OTR

The initial work on single shot emittance measurement included two other techniques. These techniques were more challenging and have been fully developed following the success of the techniques described above.

7.5.1   Emulsion based emittance measurement

Nuclear emulsions have a resolution of the order a few micrometers per hit that is a factor 10 better than CCD pixels (an example of such image is shown on figure 7.23). Given the low charge and high divergence of the beams produced by laser-driven plasma accelerator the beam reach such density after one or two meters and I investigated with several project students if this could be used to measure the transverse emittance of such beam as shown on figure 7.24.

At first it was difficult to recover the knowledge of the use of emulsions but we soon, together with undergraduate student Ana Simic, were able to observe in a microscope the tracks left by a radioactive source on nuclear emulsions and measure the position of individual hit [88]. Another student, Nick Shipman, [89] showed that by using a technique called "image registration" we would be able to match several plates of emulsions located one after the other and reconstruct correctly the emittance (see figure 7.25) [90].
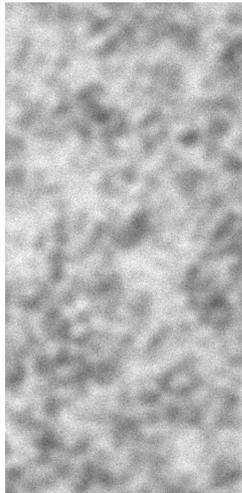
Figure 7.23: Image of electrons on nuclear emulsions. Image taken form [88].
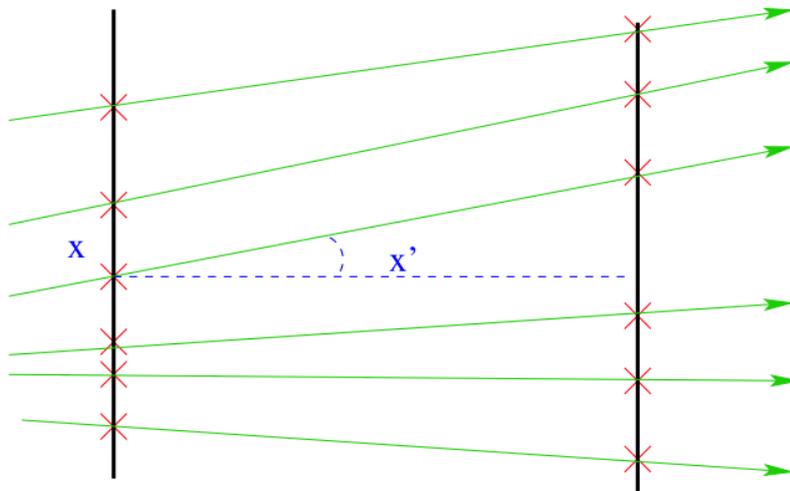
Figure 7.24: Emittance measurement using nuclear emulsions tracking.

The conclusion of this work was that the emulsion technique would be best suited for low density beams.
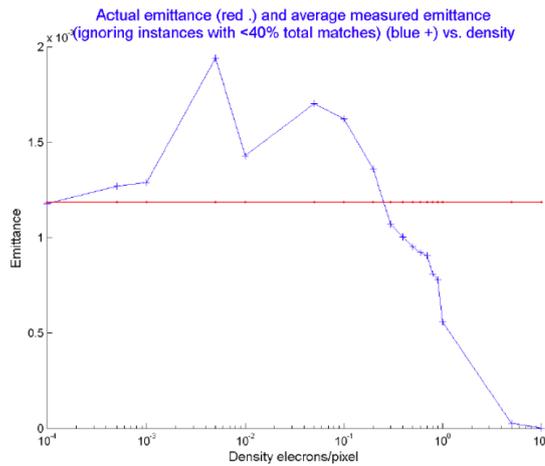
Figure 7.25: Accuracy of the emittance reconstruction depending on the electrons density (simulations taken from [90]).

7.5.2   Masked OTR

Another technique that was investigated is the use of a mask positioned between an optical transition radiation screen and the imaging CCD as shown on figure 7.26.
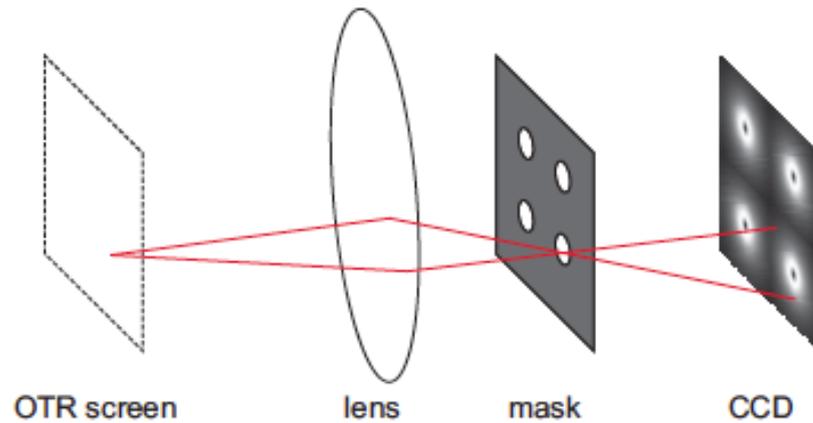

Figure 7.26: Layout of the masked OTR setup as taken from [91].

The principle of this measurement is that when they are produced the OTR photons

take the direction of the incoming electrons. The spread in direction of emission of these photons is therefore dependent on the transverse emittance of the beam. However the energy of the beam will add another smearing factor as the photons are emitted in a $1/\gamma$ cone. The addition of an out of focus masking element should allows to reconstruct this spread in direction of the photons and therefore to measure the quadratic sum of the beam transverse emittance with its energy.

Simulations were done by undergraduate student Bas-Jan Zandt to qualify the processus and they showed very encouraging results as far as energy reconstruction was concerned (see 7.27). However we did not have time to take it further to attempt to measure the energy spectrum or the transverse emittance. We also did not have the opportunity to test these results on a real beam as I stopped that work when I arrived in Orsay.
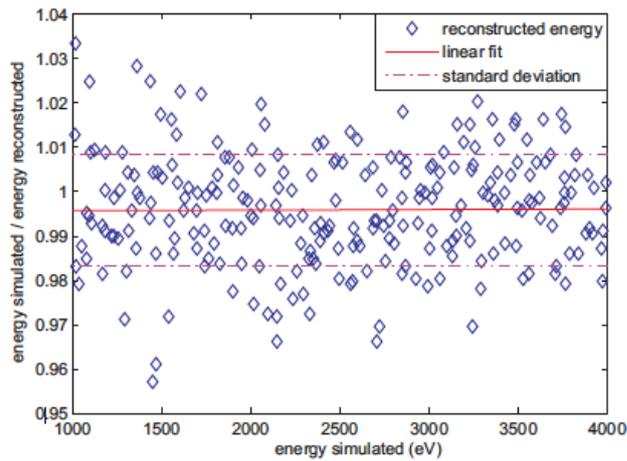

Figure 7.27: Simulations of energy measurements using masked OTR taken from [91].

I am aware that at least another group has demonstrated the use of OTR to measure the transverse emittance of a beam [92].

7.6 Overview of emittance measurement

My work on transverse emittance measurement has led to the conception and on beam demonstration of several single shot transverse emittance measurement diagnostics. The figure 7.28 shows the type of beam parameters where each of these techniques apply. The emulsions can only be used on beams that have a low density as each impact needs to be resolved separately. The pepper-pots can measure higher density beams, but preferably at low energy (up to a few energy). The OTR based method is also for high density beams (when the OTR light is strong enough) and are better suited to high energy as the scattering is inversely proportional to the energy.
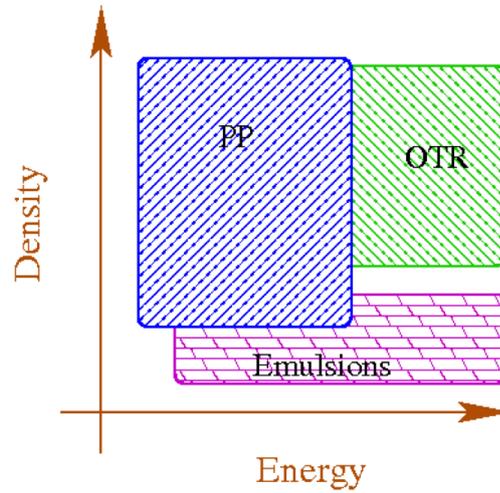
Figure 7.28: Range of applicability of the three techniques discussed in this chapter: the emulsions are better suited to low density beams; the pepper-pots are better suited to high density beams and rather low energy (up to a few GeV) whereas the OTR techniques are better suited to high intensity high energy beam.

Chapter 8

Bunch length measurement

The length of a particle bunch is rather difficult to measure at lepton accelerators where this length is typically less than a millimeter, corresponding to bunch durations much shorter than what can be measured by fast detectors[1]. It is therefore necessary to convert the bunch length into another quantity that can be measured. Coherence is both a motivation and a tool to measure such length. Coherent collective effects such as coherent synchrotron radiation can significantly disrupt a beam. Their dependance on the beam current and not the beam charge means that to control them it is necessary to measure the bunch length instead of simply the bunch charge. As a counterpart, coherent radiation is one of the means of measuring a bunch length.

In plasma acceleration with external injection (such as FACET's E-200 [31], AWAKE [34] or ESCULAP [25]) this bunch length measurement is important to estimate which fraction of the bunch will fit in the acceleration buckets created in the plasma. As with the transverse measurements, at a plasma accelerator it is necessary to make the measurement in a single shot for it to be meaningful.

When the resolution is sufficient the bunch length measurement can become a bunch profile measurement as is the case with the methods based on coherent radiation.

I have worked on one of these techniques using Coherent Smith-Purcell Radiation for several years.

---

[1]Because in lepton accelerators the particles travel at the speed of light there is a direct correlation between bunch length and bunch duration. It results that abusingly the bunch length is often quoted with time units. A bunch duration of $1\,\mathrm{ps}$ corresponds to a bunch length of $0.3\,\mathrm{mm}$.

8.1   Bunch length and bunch profile measurement techniques

Several other techniques allow for bunch length measurements and I will first review them.

8.1.1   Techniques based on current transformers

Bunch charge can be measured using current transformers (CT). Depending on the application, there are several flavors of current transformers : AC-Current Transformers (ACCT), DC-Current Transformers (DCCT), Integrating Current Transformers (ICT),... They all measure the current induced by the beam in a gap of the beam pipe to estimate the beam current. Depending on the signal amplification required the measurement device can be a simple wire connected to an ammeter or a coil with several windings connected to an ammeter or to more complicated electronics. The working principle and an example of current transformer are shown on figure 8.1.

When the time resolution of the current measuring device is good enough and the impedance low enough the current transformer can give information about the variation of the current with them and therefore the bunch length, however this is true only for beams that are at least several centimeters long (nanosecond duration).
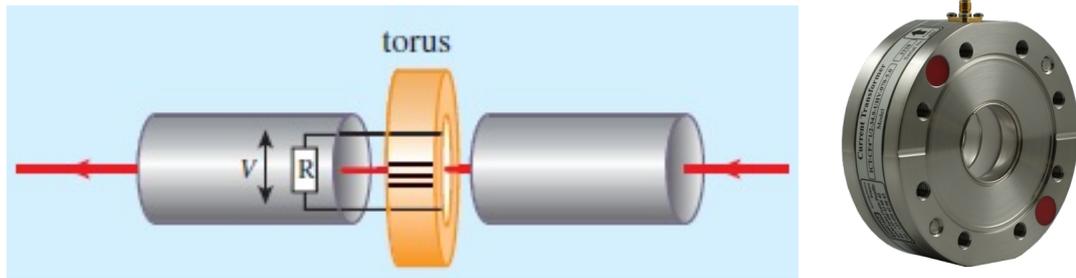

Figure 8.1: (Left) Principle of a current transformer used for beam charge measurement : when the particle beam passes through a torus it induces a current proportional to the beam charge in the torus coil windings, allowing for beam charge measurement. (Right) Example of current transformer as sold by a well-known manufacturer [93].

8.1.2   Techniques based on longitudinal to transverse exchange

For beam with a length in the millimeter range (or below) it is more difficult to measure their length or their profile in the longitudinal direction (that is the direction of propagation) than their transverse properties. Exchanging the longitudinal direction with one of the transverse directions can therefore make this measurement easier.

A **Streak Camera** is a device available commercially that can achieve this fate : in a streak camera a photon beam hits a photocathode and is converted by photoemission in a low energy (keV) electron beam. This electron beam passes between two electrodes to which are applied a high frequency high voltage electric field that will streak the electron beam transversely, the electron deflection being proportional to their arrival time. After the electrodes the electron beam hits a luminescent screen where the transverse profile of the electrons after streaking can be observed. Thus it is possible to obtain the longitudinal profile of the photon beam (convoluted with one of its transverse profile). Commercial streak camera can reach a resolution of about 1 ps on photon beams.

A **Streak Camera combined with a radiation emitting screen**, such as a sapphire screen emitting Cerenkov radiation can be used to image the longitudinal profile of an electron beam with MeV energy or higher. Such method was tested for example at the CANDELA photo injector at LAL [94]. However this method is limited by the spread in the longitudinal profile induced by the screen itself and by the photon beam transport (usually to the outside of the accelerator) and therefore it is not available to measure sub-picoseconds beams.

Streak camera are often used in rings to measure the bunch length using the synchrotron radiation emitted[95, 96].

This can be mitigated by deflecting directly the high energy electrons using a **deflecting RF cavity**. This requires the electric field to be high enough to deflect high energy electrons and to have a high enough frequency to streak significantly the beam. The state of the art in this field has been demonstrated at SLAC recently on both LCLS and FACET accelerators [97], reaching resolutions of 10 fs at 14 GeV and 70 fs at 20 GeV. However the cost of such device, including the associated RF power source is more than a million euros.

A cheaper solution to streak the electrons is to use the so-called **3-phases method** [99, 100] in which one of the accelerating section of the accelerator is dephased to provide a longitudinal streaking effect that can be measured as a variation in the beam energy dispersion. This method has the advantage of being much cheaper but is limited in its resolution by the power of the accelerating cavity and the resolution of the dispersion measurement setup. A resolution of a few picoseconds has been demonstrated experimentally.

8.1.3 Measures based on radiation emitted by the beam

Instead of manipulating the beam to measure it, it is possible to measure the radiation it emits and use it to get information on its longitudinal profile. This is what is done with the streak camera based measurements described above but other methods rely on this technique.

In the **electro-optic sampling** method a birefringent crystal is brought close from the
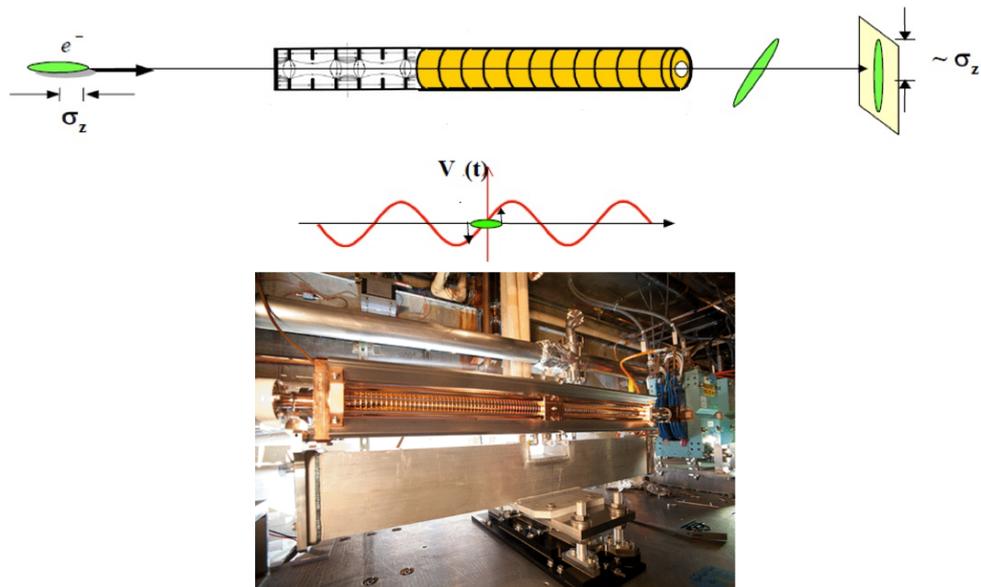
Figure 8.2: Left: The principle of the Transverse deflecting cavity used at SLAC to measure bunches longitudinal profiles (Image taken from [98]). Right: A photo of the FACET transverse deflecting cavity (image taken from [97]).

electron beam and a chirped ultrafast laser pulse[2] is shone on it. The electromagnetic field of the electron beam will induce a change in the refraction index of the crystal in at least one of the polarisation plane. As the laser pulse is chirped a diffraction grating can then be used to measure its longitudinal profile projected on a screen. Thus by comparing the longitudinal profile of the two polarisation components it is possible to deduce the changes that occurred in the crystal as fonction of time and therefore the bunch longitudinal profile. This is a well known technique in optics (for example to measure and profile THz pulses) that has been applied to accelerators by several groups (including, for example, [101, 102, 103]). This technique is illustrated on figure 8.3.

Several techniques rely on the emission of **Coherent radiation** which encodes the bunch length: The electromagnetic spectrum emitted by the electron bunch is modulated by the bunch length. When a photon is emitted in an electron bunch, if the wavelength of that photon is larger than the separation between the emitting electron and another electron it will enhance the probability of emission on that other electron. When N electrons contribute to the emission the probability increases as $N(N-1)$.

It is possible to define the "form factor" ($\mathcal{F}$) of the radiation emitted by an electron bunch as:

---

[2]This means that the photons of the laser pulse have a correlation between wavelength and longitudinal position. This is a common techniques with lasers and can be done, for example, by using a set of diffraction gratings.
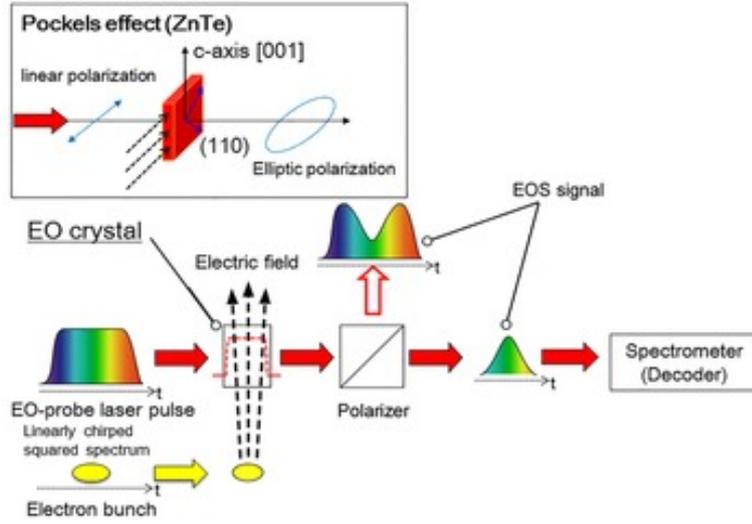
Figure 8.3: Principle of bunch length measurements using electro-optic sampling (taken from [103]

$$\mathcal{F}(\nu) = \left| \int_{-\infty}^{+\infty} S(x) \exp\left(i\frac{2\pi\nu}{c}x \right) dx \right| \times \left| \int_{-\infty}^{+\infty} S(y) \exp\left(i\frac{2\pi\nu}{c}y \right) dy \right| \times \left| \int_{-\infty}^{+\infty} S(z) \exp\left(i\frac{2\pi\nu}{c}z \right) dz \right|$$
(8.1)

where ν is the photons' frequency, $S(x)$, $S(y)$ and $S(z)$ are the profile distribution along x, y and z respectively. And the total radiation intensity I_{tot} emitted for a given radiative phenomena at a given frequency will be:

$$I_{tot}(\nu) = I_1(\nu)\left(N + N(N-1)\mathcal{F}(\nu) \right)$$
(8.2)

where I_1 is the single electron yield for the phenomena and N the number of electrons. This radiation can be used in several different manners to measure the bunch length and its longitudinal profile.

Coherent Transition Radiation (CTR) is emitted when a bunch of charged particles passes through a thin foil. Several groups [104, 105, 106] have studied how to measure the spectrum of the CTR emitted and used it to reconstruct bunch length. The SLAC group [104] uses a KRS-5 prism to disperse the infrared radiation collected and focus it on a detector. The Frascati group [105] uses a Martin-Puplett interferometer to study the THz radiation produced by their CTR screens. These setups are shown on figure 8.4. It should be noted that the methods used by these two groups require a scan of the dispersive element or of the interferometer to measure the radiation spectrum. To overcome this difficulty the DESY group [106] uses several dispersive gratings with several detectors to perform this measurement (see figure 8.5).
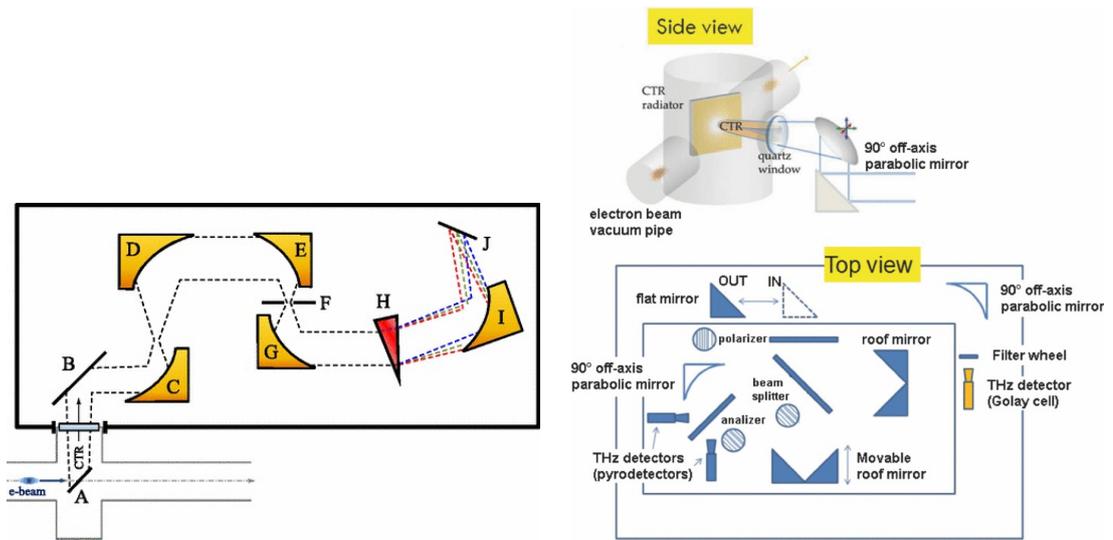
Figure 8.4: Principle of Coherent Transition Radiation measurements at SLAC on LCLS and FACET (left; taken from [104]) and at SPARC (right; taken from [105]).
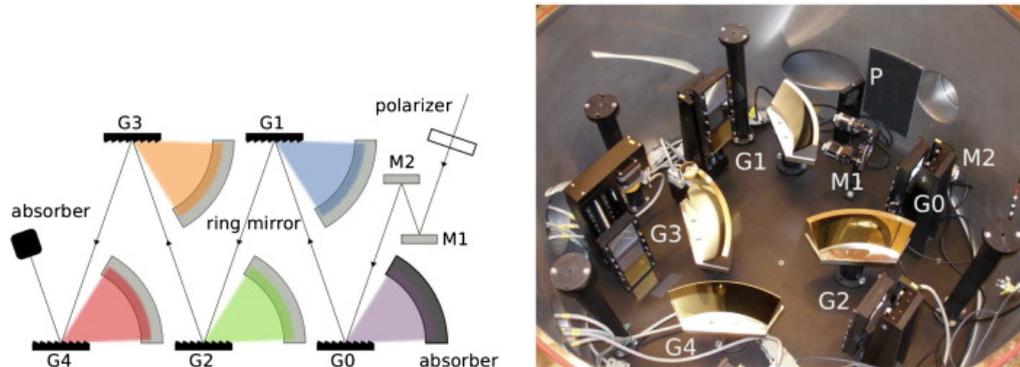

Figure 8.5: The Coherent Transition Radiation single shot setup at DESY (schematic and picture) as reported in [106].

The SLAC group has published their ability to reconstruct 3 fs to 60 fs-long bunches.

Another way to measure the radiation emitted by the bunch is to measure the **Coherent Smith-Purcell Radiation (CSPR)** it emits. CSPR is emitted when a metallic diffraction grating is brought close from the beam. I have worked extensively on CSPR for several years and it is described details in section 8.2.

8.1.4 Comparison of longitudinal bunch measurement techniques

The different longitudinal bunch measurement techniques are summarized in tables 8.1 and 8.2.

From theses tables it appears that there is a wide range of cost and complexity among longitudinal bunch length measurements. The use of RF deflecting cavities is both complex and expensive (the price been dependent on the beam energy and the RF band chosen for the measurement) but it is used at several accelerators as a reference to measure the bunch length[3]. This has triggered research to find cheaper techniques. Electro-optic sampling is a technique that was already available from the optics community, however it is complex as it requires an ultrafast laser that is hardly compatible with an accelerator enclosure and therefore requires to transport the ultrashort laser pulses inside the accelerator enclosure. CTR has the advantage of being even cheaper and less complicated to setup and several groups have investigated it and solved differently the problem of spectrum measurement. CSPR is a less known phenomena and therefore it has been investigated by fewer groups but renewed interest appeared because of its single shot and non-destructive capability.

The interest for Energy Recovery Linac (ERL) may also increase the need for non destructive single shot longitudinal diagnostics: current ERLs have shown that correct operations require a very good understanding of the bunch longitudinal phase space at different locations along the ERL. The availability of a non destructive fast diagnostics would therefore be an advantage for such machine and in particular for the machine that is planned to be built in Orsay.

---

[3]A comparison of Electro-optic sampling, streak cameras and RF deflecting cavities as longitudinal bunch profile diagnostic for FACET has been published in [107].

Name	Main technology	Best resolution	Cost	Availability status
Current transformer	Coil	Limited by electronics $\mathcal{O}$ 100 ps	$\mathcal{O}$ 10k€	Commercially available Commonly used
Streak camera with radiator	Photocathode, High Voltage	Limited by high voltage frequency $\mathcal{O}$ ps	$\mathcal{O}$ 300k€	Camera commercially available Setup: R&D
RF deflector	High power RF + cavity C-band or X-band RF	$\mathcal{O}$ 10 fs	$\mathcal{O}$ 500k€- 2M€ (energy dependent)	R&D product distributed by one manufacturer
3 phases	RF cavities	$\mathcal{O}$ ps	Use linac infrastructure	Commonly used
Electro-optic sampling	Laser Birefringent crystals	$\mathcal{O}$ 50 fs (better res. in optics)	Laser: $\mathcal{O}$ 200k€ Other: $\mathcal{O}$ 50k€	Commonly used in optics
Coherent Transition Radiation	Optics THz filtering	$\mathcal{O}$ 10 fs	$\mathcal{O}$ 50k€	In use at several facilities
Coherent Smith-Purcell Radiation	Diff. gratings THz filtering	$\mathcal{O}$ 50 fs	$\mathcal{O}$ 50k€	R&D

Table 8.1: Comparaison of the properties of the different techniques of longitudinal bunch length and profile measurement

Name	Single shot capability	Beam destruction
Current transformer	Yes	No
Streak camera with radiator	Yes	Radiator dependent Synchrotron radiation: No; Screen: Yes
RF deflector	Partially The phase of the measurement must be checked	Yes
3 phases	No	Yes (beam off-energy)
Electro-optic sampling	Yes	No
Coherent Transition Radiation	Interferometer: No; Multpl. Gratings: Yes	Yes
Coherent Smith-Purcell Radiation	Yes	No

Table 8.2: Comparaison of the capabilities of the different techniques of longitudinal bunch length and profile measurement

8.2 Smith-Purcell Radiation

8.2.1 First observation of Smith-Purcell Radiation

The first observation of what is now called Smith-Purcell Radiation dates back to 1953 when Smith and Purcell reported the observation of visible light from localized surface charges moving across a grating [108]. Their observation was made using 300 keV electrons in a continuous beam. An image of this observation is shown on figure 8.6.
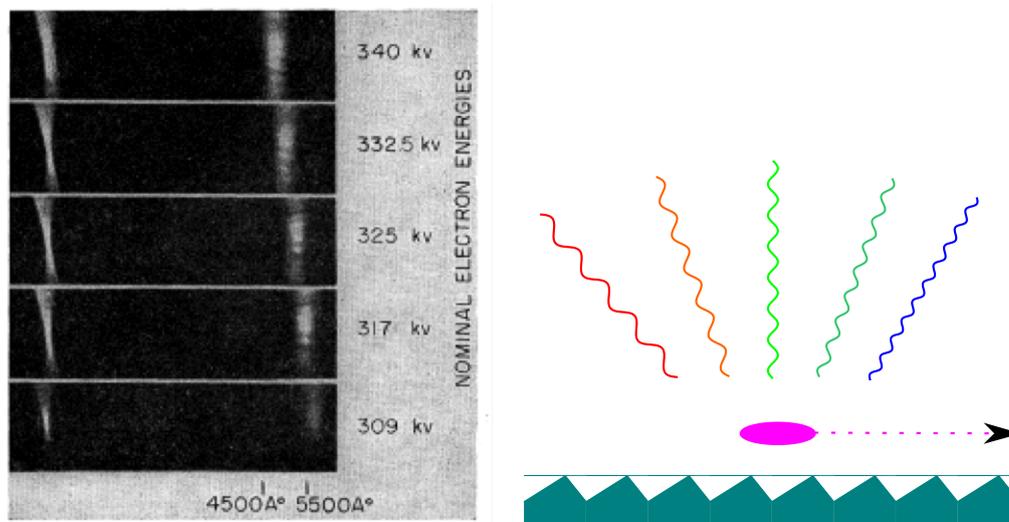

Figure 8.6: Left: Image taken from [108] showing the observation of radiation by Smith and Purcell in 1953. Right: Schematic of Smith-Purcell radiation.

The first observation of Smith-Purcell radiation from relativistic electrons was reported only much later in 1992 [109] and the first observation of Coherent Smith-Purcell Radiation [110] came in 1995 and an image taken from that publication is shown on figure 8.7.

8.2.2 Interpretation of Smith-Purcell Radiation

The phenomena was further studied and several interpretations were proposed:

- According to Ishiguro and Tako's interpretation [111], Smith-Purcell radiation comes from dipole radiation: when an electron beam passes above a grating it induces a current in the grating; the oscillations of this current in the teeth of the grating will create dipole radiation that is emitted. This will later be referred to as the "surface current" interpretation. This interpretation is shown on figure 8.8 (left).
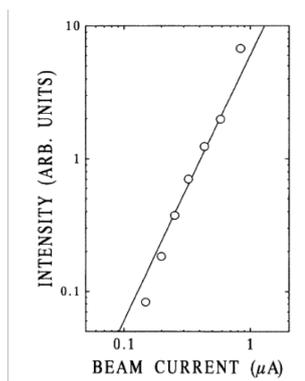
Figure 8.7: Image taken from [110] showing the first observation of Coherent Smith-Purcell Radiation (CSPR): the intensity of the radiation varies exponentially with the current, not linearly.

- Toraldo di Francia proposed a different interpretation [112]: according to him a charged particle in straight uniform motion generates a field that can be expanded into a set of evanescent waves. It is the diffraction of these waves on a diffraction grating that creates the Smith-Purcell radiation. This will later be referred to as the "radiation diffraction" interpretation. This interpretation is shown on figure 8.8 (right).
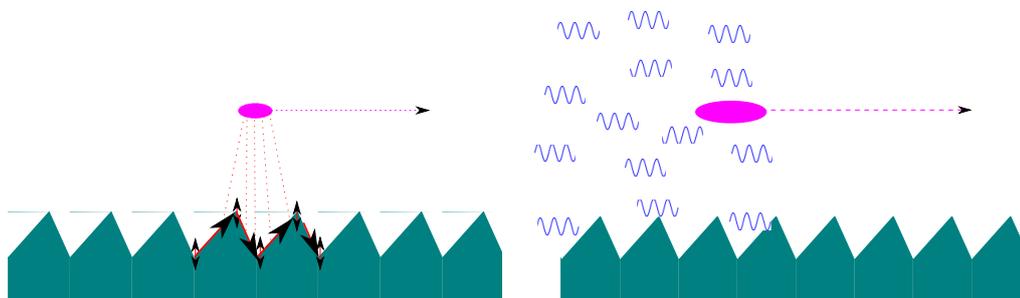

Figure 8.8: The two interpretation of Smith-Purcell radiation: The surface current interpretation as in [111] (left) and the radiation diffraction interpretation as in [112] (right).

Although these interpretations are different, the underlying physics is the same and the interpretations should yield to comparable predictions. A comparison of several Smith-Purcell radiation models has been published in [113] and based on that paper I worked with a student, Maksym Malovitsya, to perform such comparison for parameters relevants to the experiments we were conducting [114]. Our conclusion was that within an order of magnitude all models have to comparable single electron yield as shown on figure 8.9.
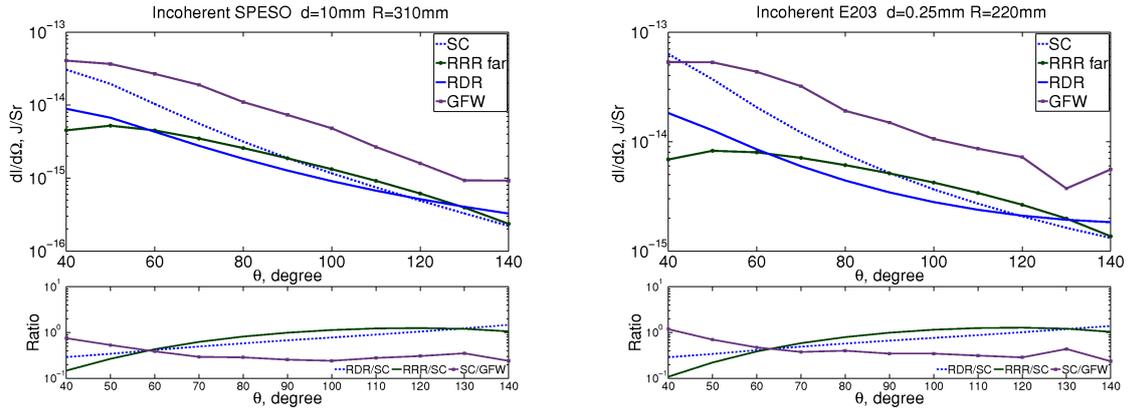
Figure 8.9: Comparison of the single electron yield of different Smith-Purcell Radiation models (as published in [114]): the solid blue line corresponds to the Resonant Diffraction Radiation (RDR) model [113], the green line to the Resonant Reflection Radiation (RRR) model [115], the purple line with square marker label GFW to the Surface Current model as described in [116] and the blue dashed line also to the Surface Current (SC) model described in [116] but with the grating coupling efficiency expression taken from [113]. See [114] for details.

8.2.3 Application of Smith-Purcell Radiation

Smith-Purcell radiation and later CSPR have been seen by many scholars as a potential source of high power infrared radiation, leading for example to a patent to that purpose [117]. As early as 1979, Smith-Purcell radiation has also been seen by some scholars as a promising tool to seed Free Electron Lasers [118, 119, 120, 121, 37] and has been patented [122].

The use of CSPR as a bunch longitudinal profile diagnostic was proposed soon after the first observation of CSPR and it was also patented [123] (for the US only) at that time. More detailed work was published by a different team in 2002 [124, 125] and several key steps were done in the following years [126, 127], including in teams in which I was participating [128, 129, 130, 131].

8.2.4 Theoretical aspects of Smith-Purcell Radiation

The theory of Smith-Purcell radiation has been developed in several publications. The most relevant of them, based on the surface current model, being [116, 132]. The discussion below is based on these articles.

A diffraction grating will reflect light in different directions by interferences between the rays reflected by each surface. As shown on figure 8.11, reflections corresponding to the
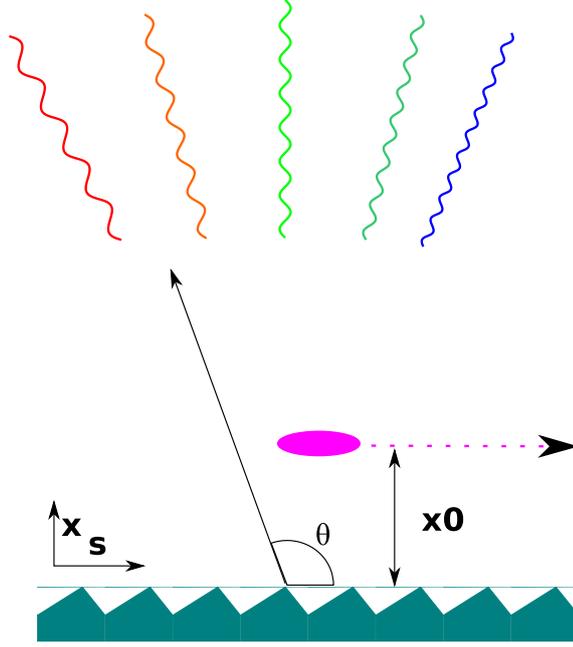
Figure 8.10: Coordinates system used in this chapter. The direction z comes out of the figure plane as is the azimuthal angle ϕ.

simple Snell-Descartes law are called "Order 0". Higher order correspond to interferences between all the teeth (order 1) or part of the teeth.

The coordinate system used in this chapter is shown on figure 8.10.

The relation between the polar angle of observation θ (in the plane perpendicular to the grating surface and passing by the beam), the grating pitch l and the wavelength λ of the emitted radiation is given by

$$\lambda \;=\; \frac{l}{n}\left(\frac{1}{\beta} - \cos\theta\right) \tag{8.3}$$

where n is the radiation order and $\beta = \frac{v}{c}$ is the ratio between the particle speed v and the speed of light c. In lepton accelerator it is often very close to 1. This relation is purely a consequence of the fact that waves emitted by a grating will interfere and in each direction constructive interferences correspond to specific wavelengths.

The intensity of radiation emitted by a single electron (single electron yield), per unit solid angle (Ω) is given by

$$\frac{dI_1}{d\Omega} \;=\; \frac{L}{l^2}\frac{2\pi e^2 n^2 \beta^2}{(1-\beta\cos\theta)^3}R^2 \exp\frac{-2x_0}{\lambda_e} \tag{8.4}$$

86
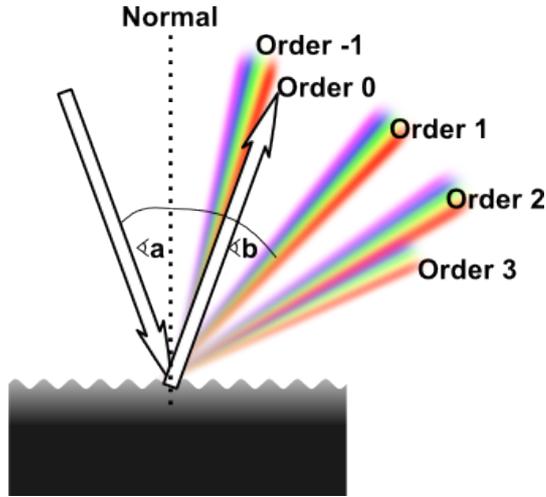
Figure 8.11: The different orders of a grating: order 0 corresponds to a simple reflection, the other orders corresponds to interferences of the wavelengths reflections. Image taken from [133].

where e is the electron charge, L the grating length, x_0 is the beam grating separation, λ_e is the evanescent wavelength of the virtual radiation emitted by the beam and R^2 is a factor reflecting the coupling of the beam with the grating.

The evanescent wavelength is given by

$$\lambda_e = \lambda \frac{\beta\gamma}{2\pi\sqrt{1 + (\beta\gamma\sin\theta\sin\phi)?2}} \tag{8.5}$$

where γ is the Lorentz factor, ϕ is the azimuthal angle (the ascension above or below the plane perpendicular to the grating surface and passing by the beam).

An example of values of single electron yield taken from [134] is shown on figure 8.12.

As discussed above, equation 8.2 applies to Smith-Purcell Radiation and the total radiation intensity emitted from a charged particle bunch of multiplicity N is given by:

$$\frac{dI}{d\Omega} = \frac{dI_1}{d\Omega}[N + N(N-1)\mathcal{F}(\omega)] \tag{8.6}$$

where $\mathcal{F}(\omega)$ is the form factor introduced in equation 8.1.

On figure 8.13 one can see a comparison of different profiles with the same FWHM (5 ps) but with different shapes and how this changes the expected CSPR signal.

One important difference between CSPR and other radiative methods is that the choice of the grating will change the radiation intensity observed at different frequencies. On

87
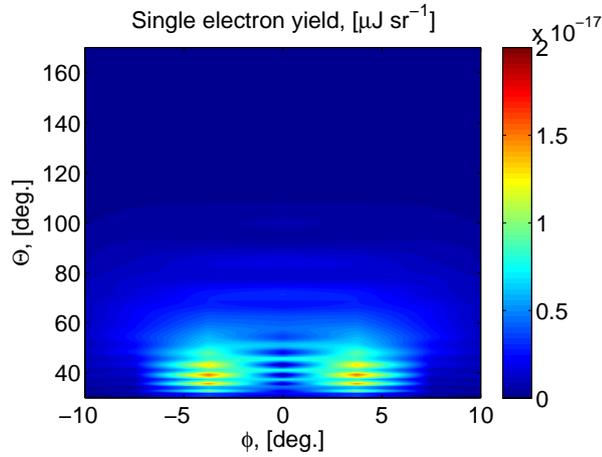
Figure 8.12: Single electron yield of Smith-Purcell radiation for a 40×180 mm^2 grating with a 8 mm pitch and a 30° blaze angle. Image taken from [134].
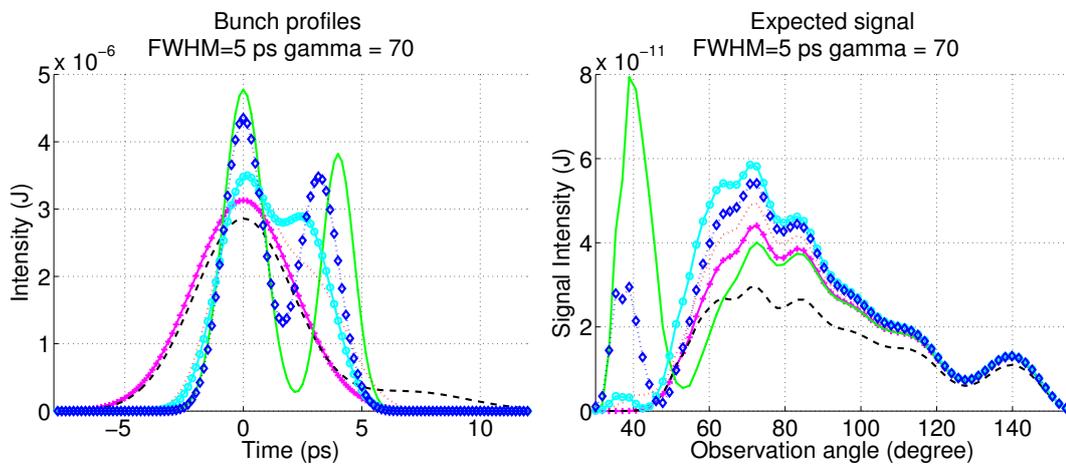
Figure 8.13: Comparison of several bunch profiles with the same FWHM (5 ps) but with different shapes (left) and predicted CSPR signal for each of these profiles (right). The capability to distinguish internal features of the beam and in particular substructures appears clearly. The parameters used for these simulations are based on the experiment done at CLIO (see section 8.3.3).

figure 8.14 one can see the radiation intensities observed for the same bunch profile but with different gratings pitches.
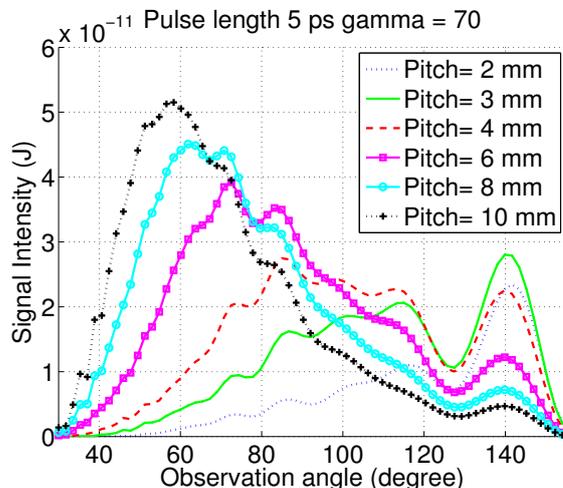
Figure 8.14: Radiation profiles observed for the same pulse but for different grating pitches. The parameters used for these simulations are based on the experiment done at CLIO (see section 8.3.3).

Improving the beam-coupling calculation

The factor R^2 in equation 8.4 is rather complicated to estimate. It has been discussed in details in [135] and an approximate solution has been given for high energy beams in the case of echelette gratings.

The equation 8.3 is very similar the the standard grating equation in the Littrow condition (with the same definition of variables as above) [136]:

$$\lambda = \frac{2l \sin \theta}{n} \tag{8.7}$$

This has led me to study with two students Solène Le Corre [137] and Clément Duval [138] whether it would be possible to benefit from the advanced work done in the field of grating theory [139] to estimate R^2. We produced some predictions but these are rather close to what has been obtained with simulation codes based on [135] and therefore we have not yet been able to distinguish the two approaches. This may become possible at the experiment described in 8.3.3.

It should be noted that with the advent of fast and powerful Particle-in-cell electromagnetic simulation softwares, it becomes possible to simulate the electromagnetic effects that a charged particles beam induces near a grating without relying on the models described above. This is what has been attempted in [140].

8.2.5 Profile recovery

As we can see in equation 8.6, there is a mathematical relation between the form factor and the CSPR intensity at each wavelength. Using relation 8.3 we see that this means that the signal intensity measured at different angles depends on the form factor and therefore encodes the bunch length. Calculating the form factor from the measured signal is therefore rather straightforward.

We have also seen in equation 8.1 that the form factor is strongly related to the bunch longitudinal profile. However the inverse operation is not so easy: some information is lost due to the absolute values in equation 8.1. The knowledge of the form factor alone requires more complicated mathematics to recover the profile.

The Fourier transform of a physical function satisfies the Cauchy-Riemann equations therefore a given real function (the measured form factor) can only be matched to a very limited number of imaginary functions and usually by adding extra conditions there will be only one remaining acceptable imaginary (phase) function. This phase function can be found using a Hilbert transform or the Kramers Kronig (KK) relations.

To recover the phase of a form factor, it must first be written in the following form:

$$log(\mathcal{F}(\omega)) = log(\rho(\omega)) + i\Theta(\omega) \tag{8.8}$$

where $\rho(\omega)$ is the amplitude and $\Theta(\omega)$ the phase associated to this form factor. The function $\rho(\omega)$ is thus the result of the measurement and $\Theta(\omega)$ the information that needs to be recovered.

The Hilbert transform gives then the relation

$$\Theta(\omega_0) = -\frac{1}{\pi} P \int_{-\infty}^{+\infty} \frac{ln(\rho(\omega))}{\omega_0 - \omega} d\omega. \tag{8.9}$$

and the Kramers Kronig relation gives:

$$\Theta(\omega_0) = \frac{2\omega_0}{\pi} P \int_0^{+\infty} \frac{ln(\rho(\omega))}{\omega_0^2 - \omega^2} d\omega \tag{8.10}$$

In most cases the value given by these two methods will be very close.

Before I started working on CSPR an algorithm based on KK was already available [141] for all coherent radiation phenomena. However its implementation for CSPR was sometimes leading to non-sensical results. With a student, Vitalii Khodnevych, we implemented and studied a new phase recovery algorithm based on the Hilbert transform [142]. We extended this work by doing a large number of simulations to also study the precision of this algorithm, how to optimise the position and number of detectors and how noise can affect the quality of the measurement [143]. The main results of this paper are presented below.

To study how profiles shapes match each other we defined a variable by analogy to the standard Full-Width at Half-Maximum (FWHM), this variable called Full-Width at X of the Maximum (FWXM) allows to study the width of a pulse at a certain fraction X of the maximum. The FW0.5M is similar to the usual FWHM. To compare the shape of a reconstructed profile (deco) and its orignal (orig) we define the variable Δ_{FWXM} as follow:

$$\Delta_{FWXM} = \left| \frac{FWXM_{\text{orig}} - FWXM_{\text{reco}}}{FWXM_{\text{orig}}} \right| \tag{8.11}$$

Figure 8.15 for example shows example of simulated profiles correctly reconstructed but also profiles poorly reconstructed. Figure 8.16 studies the impact of the number of detectors of the quality of the reconstruction, showing that there is an optimum at about 3×11 detectors (3 sets of 11 detectors covering different frequency ranges) and figure 8.17 shows that positioning them at constant angle is better than positioning them linearly or logarithmically (in frequency), examples of possible detectors positioning are shown on figure 8.18. Finally we also studied the effect of noise on the measured signal on the quality of the reconstruction 8.19.

Near field, far field and pre-wave effects

As the Smith-Purcell radiation is formed by a grating, there is a formation length and the number of teeth of the grating, the distance between the grating and the detector have to be taken into account. The line width of the radiation is given by the formula:

$$\frac{\delta\lambda}{\lambda} = \frac{l}{nL} \tag{8.12}$$

The effect of the grating-detector distance has been discussed in details in [131].

With a student I also studied the predictions for the pre-wave effect [144] and this work shows that corrections might have to be applied, especially at very high energy. However owing to the non observation of this effect in [80] as discussed in section 7.4.6, experimental verification of the effect of pre-wave interferences and accurate calculation are needed. Experimental attempts will be discussed in section 8.3.2.

8.3 Experimental study of Coherent Smith-Purcell radiation

When I joined the effort at the University of Oxford on CSPR our main goal was to demonstrate that CSPR could be used as a longitudinal profile diagnostic in the sub-picosecond regime. The work would lead to the E-203 collaboration that took data at
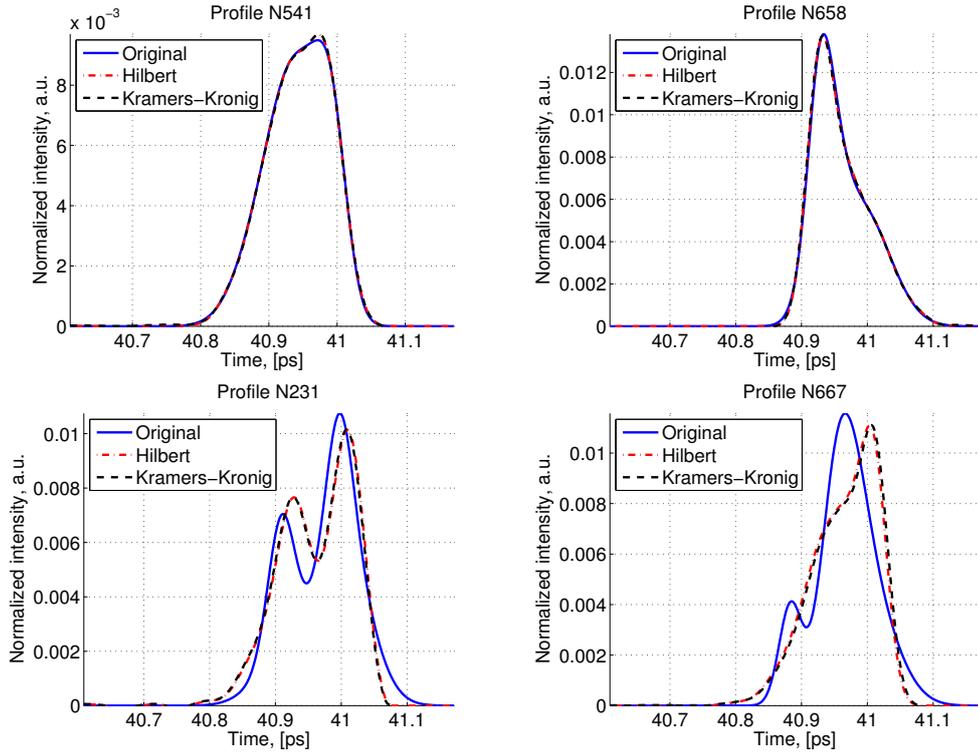
Figure 8.15: Example of profiles correctly reconstructed (upper row) and poorly reconstructed (lower row) as presented in [143]. The original profile is in blue and the profiles reconstructed with the Hilbert transform and the full Kramers-Kronig procedures are in red and black respectively.
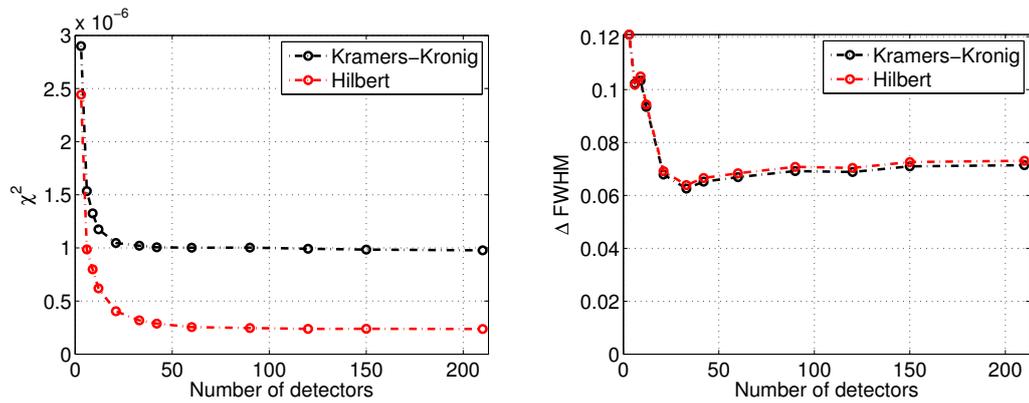
Figure 8.16: Effect of the sampling frequencies (number of detectors) on the χ^2 (left) and Δ_{FWHM} (right) when comparing original an reconstructed profiles, as presented in [143].
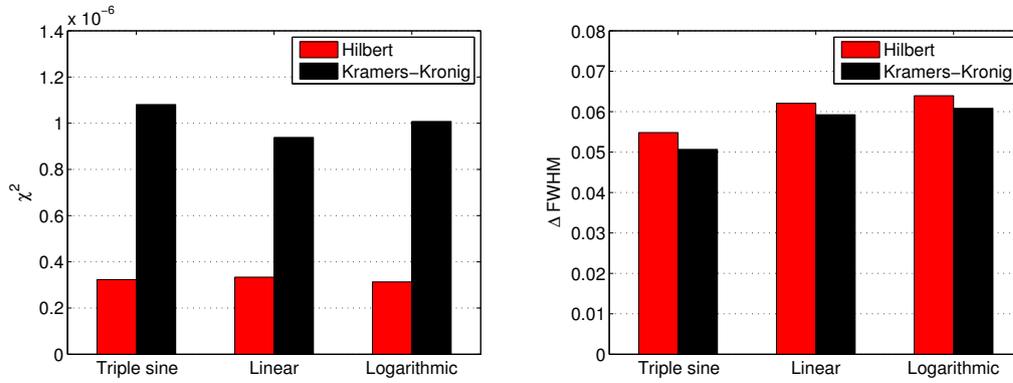
Figure 8.17: Comparison of different samplings methods using the χ^2 criterion (left) and Δ_{FWHM} (right), as presented in [143].
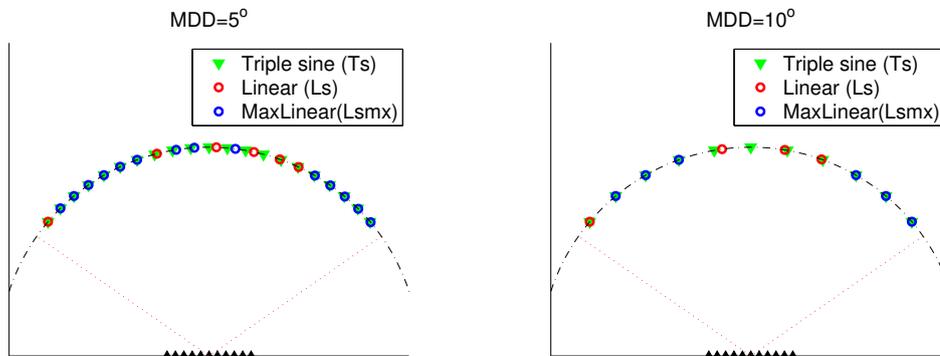
Figure 8.18: Examples of detector positions for different types of sampling for a minimal detector distance of 5° (left) and 10° (right), as presented in [143] .
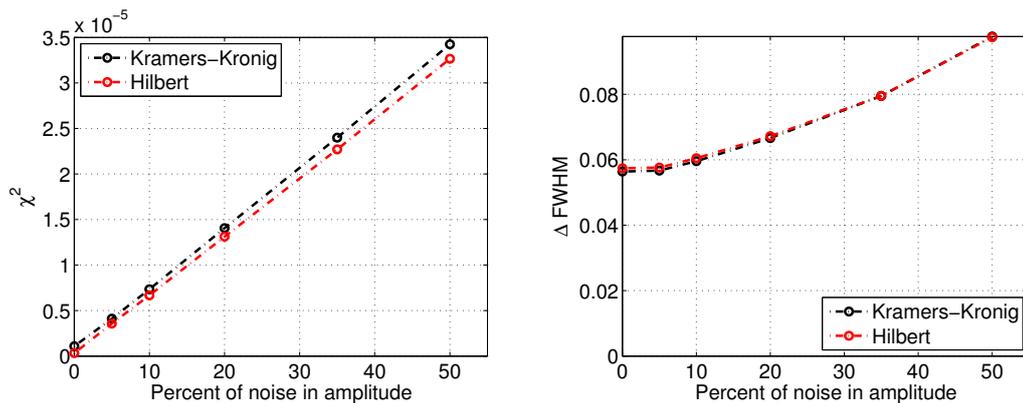
Figure 8.19: Mean χ^2 and Δ_{FWXM} as function of the noise amplitude, as presented in [143]. The interpretation of this figure is that with a 50% noise on our signal we introduce an error on the profile FWHM of about 10%.

SLAC. Later, after I moved to Orsay, I decided to extend this effort to better understand the properties of CSPR using a test setup installed at SOLEIL and called SPESO and to also study how to make CSPR a tool available in accelerators control room, by making experiments on the CLIO accelerator.

8.3.1 Smith-Purcell radiation measurement at FACET: E-203

FACET (Facility for Advanced Accelerator Experimental Tests) was a 20 GeV electron accelerator installed on the SLAC campus in Stanford, California [145]. It had the advantage of being the only test facility offering easy access to sub-picosecond bunches.

In 2010 we proposed to re-use the hardware from a previous experiment [127] to use it at FACET to measure sub-picosecond bunches. This led to the formation of the E-203 collaboration.

The experiment has been described in details in [129]. It consists of a carousel on which 3 different gratings and a blank (a flat grating without teeth) are mounted. This carousel can be moved inside the accelerator vacuum to bring the grating close from the beam. Opposite to the carousel there are 11 silicon windows located every 10° in θ from 40° to 140°. Outside the movable windows waveguide array plates (WAP) filters are used to filter only the radiation at the wavelength expected from the selected grating. After the filters Winston cones concentrate the radiation within their acceptance onto pyroelectric detectors. Several pictures of the E-203 experiment are shown on figure 8.20 and the optical elements are shown on figure 8.21.

The experiment was successful in measuring sub-picosecond bunches [129, 131, 130]. and examples of the profiles measured are shown on figure 8.22.
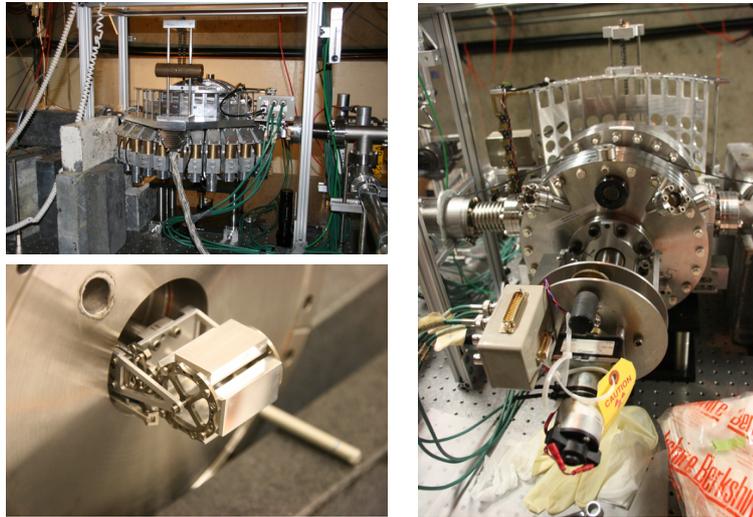
Figure 8.20: The E-203 experiment (during pre-installation tests) seen from the detectors side (top left), from the motors side (right) and the grating's carousel (bottom left). Images taken from [130].
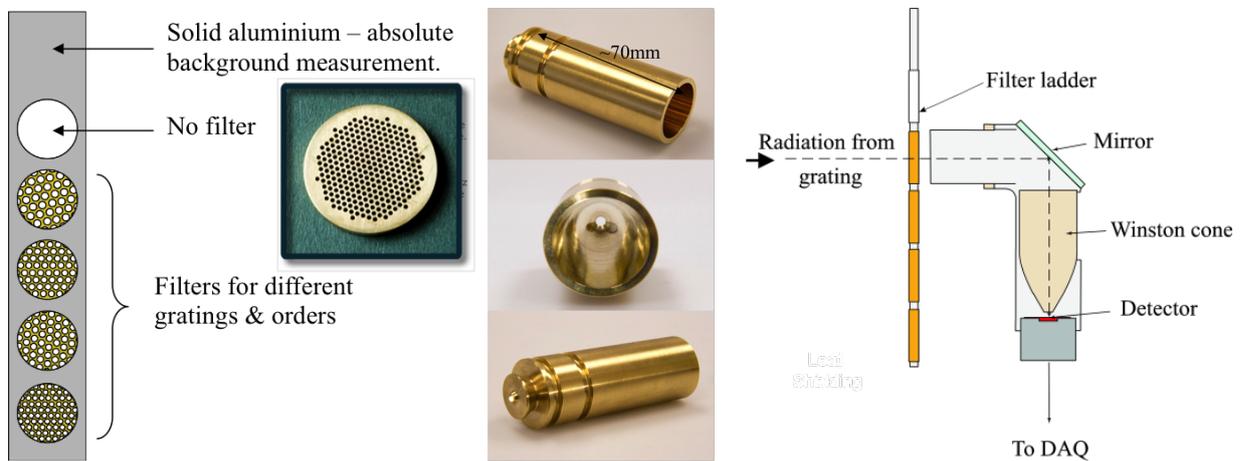
Figure 8.21: The optical parts of the E-203 experiment: (from left to right) the filters, the optical concentrators (winston cones) and the optical assembly (image taken from [131]).
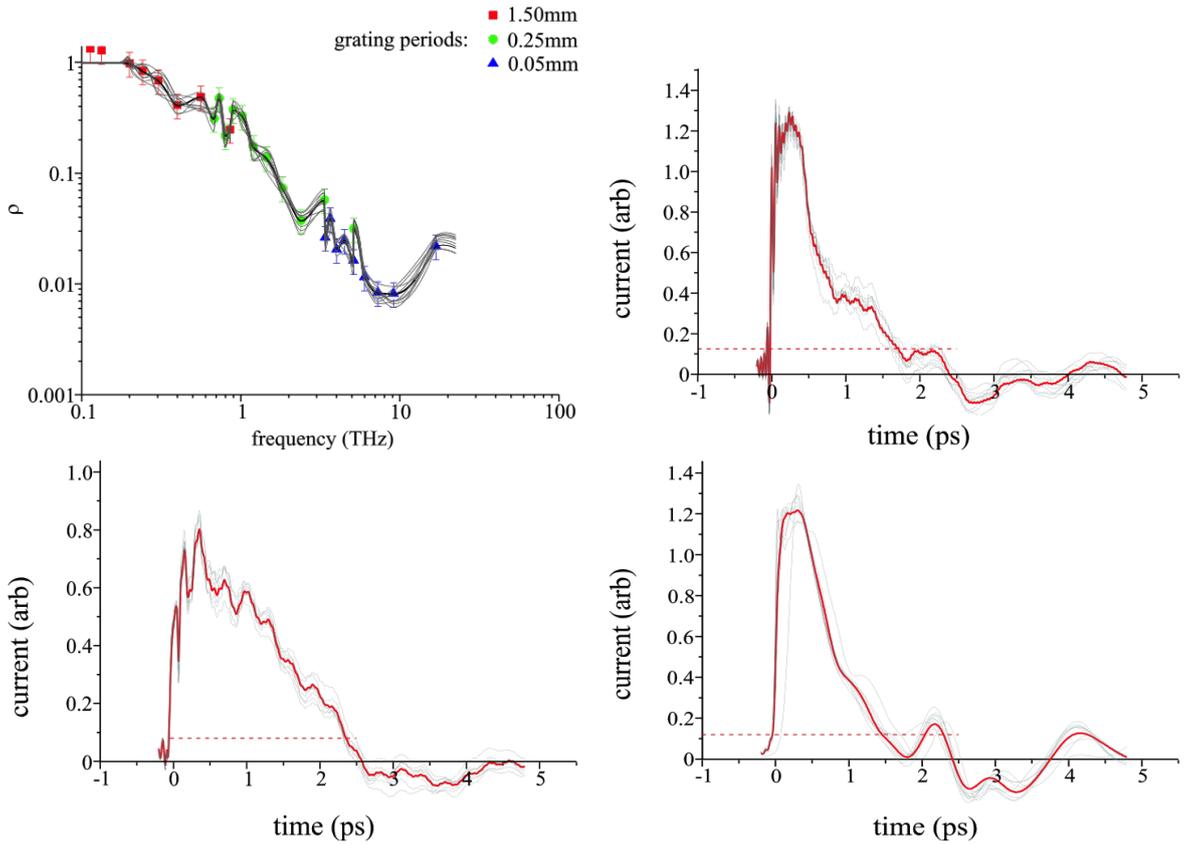
Figure 8.22: Top left: The magnitude of the Fourrier Transform of the time profile of the bunch for a "high compression" run on the 9 April 2013 (see text in [131]). Other plots: bunch profile reconstructed from measurements at different times and with different bunch compression settings (top right: 9 April 2013, high compression; bottom left: 9 April 2013, medium compression; bottom right: 25 june 2013). Plots taken from [131] where more explanations can be found.

Background rejection is an important problem for radiative measurements. Because CSPR uses the dispersion induced by the grating it is less sensitive than other methods but still not immune from background noise. One method to measure the background is to expose a "blank" grating, that is a grating without teeth, to the beam and measure the signal produced. This signal is then considered to be the background.

Another solution could be to measure the two polarisation components of the signal: CSPR is known to be polarized whereas most backgrounds aren't. We verified this with the E-203 apparatus [131] (see figure 8.23) and I worked further on that topic with a student, Solène Le Corre, who had taken part in the experiment [137].
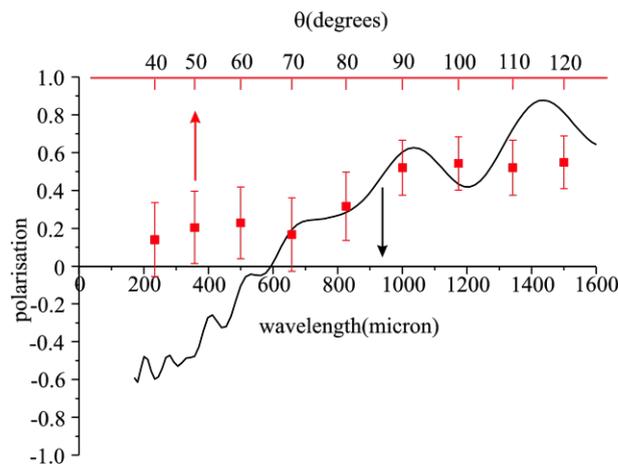
Figure 8.23: The measured degree of polarisation of the grating signal as a function of observation angle. The solid line is the theoretically predicted polarisation of CSPR, as a function of wavelength (see text in [131] for details; plot taken from [131]).

Additional measurements of the polarization and the azimuthal distribution of CSPR have been done by the E-203 experiment and are being analyzed.

8.3.2 Smith-Purcell radiation measurement at SOLEIL: SPESO

Many questions about Coherent Smith-Purcell Radiation arose when we formed the E-203 collaboration and FACET being far from Europe, it was not the best suited place to make detailed comparison between theory and experimental results.

With colleagues from Synchrotron SOLEIL I therefore started another experiment called SPESO (Smith-Purcell Experiment at SOLEIL). SPESO is installed at the end of Helios, the SOLEIL linac. For simplicity reasons SPESO uses a fixed grating on a movable arm. Opposite to this window is a z-cut quartz window (transparent at the wavelengths at which the radiation is expected). In front of that window a set of 3 translation stages and 4 rotation stages allow to move detectors in 3D and mesure the intensity of Smith-Purcell
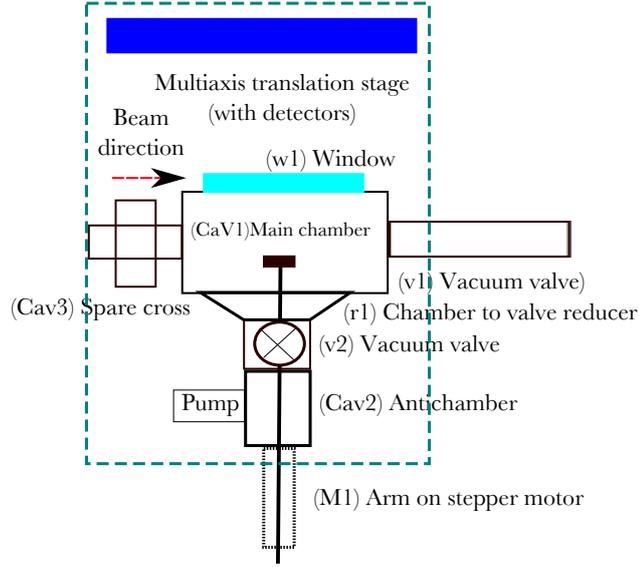
Figure 8.24: The experimental setup of SPESO at the end of the SOLEIL Linac (image taken from [146]).

radiation at different locations. The layout of the experiment is shown on figure 8.24 and a photo is shown on figure 8.25. The experiment has been described in details at [146].

The first SPESO signal was difficult to obtain because the pulse length had been underestimated. After some searching we finally found some signal at wavelength much longer than expected (see figure 8.26). These data allowed us to reconstruct the spectrum emitted by the bunch and its profile (see figure 8.27). These results were reported in [148] where detailed explanations of these figures are available. Discussion with persons who contributed to the commissioning of the linac showed that our measurement is in agreement with the measurements done during the linac commissioning.

The SPESO experiment has been upgraded in 2016 to study the polarisation of the Smith-Purcell radiation. The result has been presented in [147] and is shown in figure 8.28. This result is a surprise to us as we expected almost 100% polarization but it could be compatible with what was observed at FACET (see figure 8.23). The measurement campaign on SPESO is continuing to increase the range of the measurement.

8.3.3 Coherent Smith-Purcell radiation measurement at CLIO.

SPESO is meant to be a test bench to study the properties of Coherent Smith-Purcell Radiation. However to have this diagnostic accepted in control rooms, it is necessary to demonstrate that it can work as a control room tool and produce results quickly.

Figure 8.25: The experimental setup of SPESO at the end of the SOLEIL Linac: left, as it was in 2015 (image taken from [146]) and right with the polarizer installed in 2016 (image taken from [147]). On both images the electrons travels from left to right.
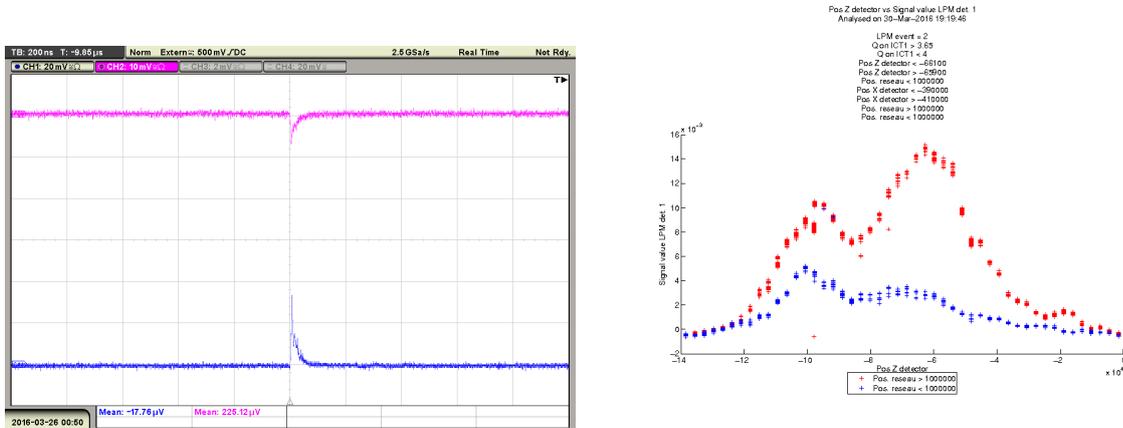
Figure 8.26: Left: Example adapted from [148] of the initial data recorded with the two SPESO detectors (Pink is the Q-band detector and blue is the Ka-band detector, see explanation in [148]). Right: Example taken from [148] of raw signal collected with the the Ka-band detector while the detectors were moving vertically. The red line corresponds to the grating in the inserted position and the blue line to the grating in the retracted position (background).

99
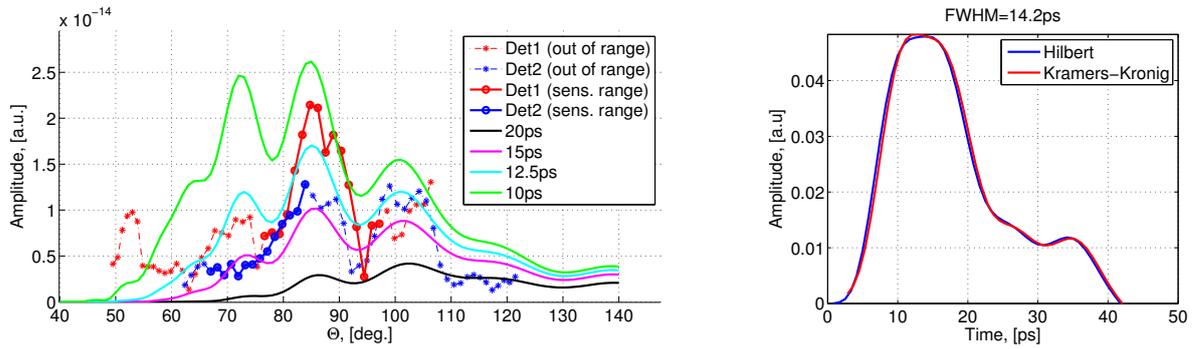
Figure 8.27: Images taken from [148]. Left: Distribution of the signal measured as function of the observation angle. The red dots correspond to the Ka band detector and the blue dots to the Q-band detector. The solid lines correspond to data points at frequencies within the sensitivity range of the detector and the dashed lines to data points at frequencies outside that range. These data are compared to simulations for 4 different bunch FWHM. Right: Bunch profile recovered from the data presented on the left using the method described in [143].
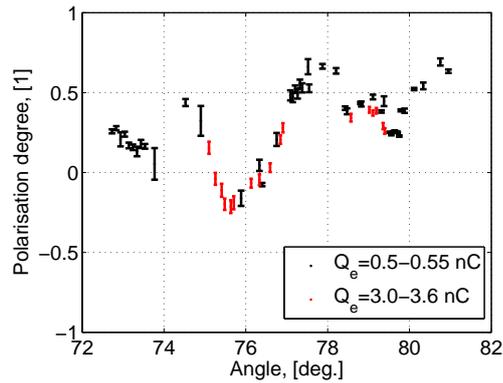
Figure 8.28: Degree of polarisation as function of the longitudinal displacement (along the beam propagation axis). Image taken from [147].

This is the aim of the Smith-Purcell experiment at CLIO. CLIO (Acronym in french for Infrared Laser Center at Orsay - *Centre Laser Infrarouge à Orsay*) is a Free Electron Laser installed in Orsay. It has been described in [149, 150, 151].

Before installing the experiment we studied the dynamics of the beam and the predicted signal [134]. Example of expected signal are shown on figure 8.29. To avoid searching the signal for too long in case the pulse length was very different from the expectations we decided to first measure CTR and made a comparison of expected signal level for CTR and CSPR [152]. On figure 8.30 the single electron yield and the predicted spectrum at CLIO are compared. Our conclusion was that using the CLIO parameters and with a

beam-grating separation of $3\,\mathrm{mm}$ we expect a signal (in the range 0.03-3 THz [0.1 - 10 mm]) of $8.37 \times 10^{-7}\,\mathrm{J}$ for CSPR and $7.35 \times 10^{-8}\,\mathrm{J}$ for CTR. This result was questioned by a few colleagues but finally accepted and confirmed by independent experimental verifications made at another facility by another group [153].
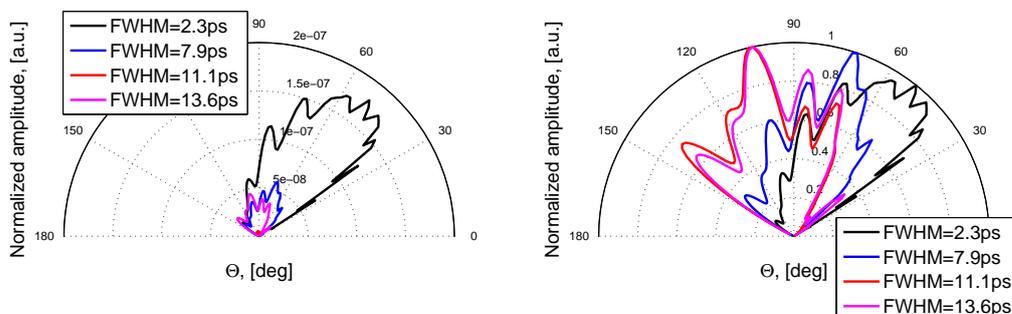
Figure 8.29:   Coherent Smith-Purcell spectrum as a function of the observation angle for different bunch profiles in CLIO. The grating used for these simulations has a pitch of 8 mm and a blaze angle of 30°. The left figure gives the energy distribution, the right figure is normalized so that the maximum amplitude of each line is 1. Image taken from [134].

After a first phase during which we measured CTR to validate the detection chain the experiment has quickly been upgraded with a grating instead of the CTR screen. Unlike the E-203 experiment we use single quartz window to let the radiation out. We also decided to use Off Axis Parabolic mirrors (OAP) instead of Winston cones to focus the radiation of the detectors. Photos of the experiment are shown on figure 8.31 and the experiment has been described in details in [154].

After the publication of [154] further work was done and has been reported in [155]. The figure 8.33 shows form factors that were measured on CLIO and figure 8.34 shows the reconstructed profile.

During the recent runs we took data with two different grating pitches. As the data were taken on different days (at the moment changing the grating requires breaking the vacuum) it is difficult to put them together but the comparisons we did looks promising.

The experiment will be upgraded in a few months so that we will be able to change the grating without breaking the vacuum. We also hope to be able to test strategies were 3 gratings will be exposed at the same time (at different azimuthal angles) to be able to do single shot measurements a scheme showing a transverse view of such layout is shown on figure 8.35.
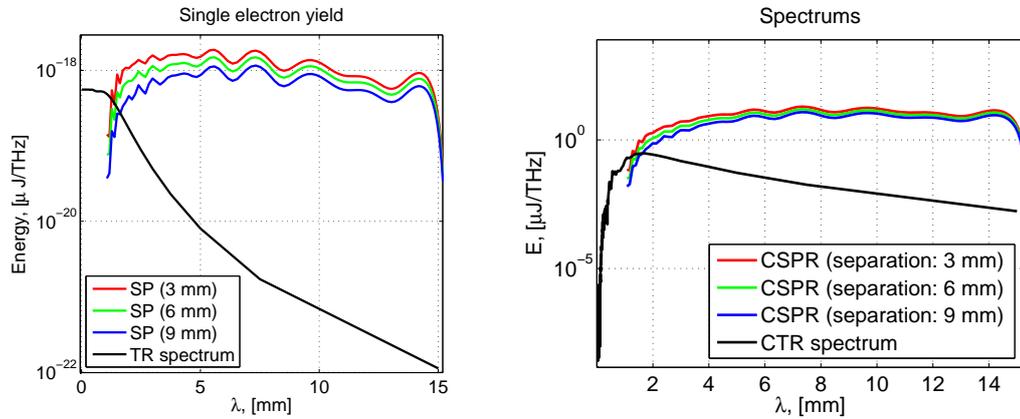
Figure 8.30: Left: Single electron yield for transition radiation (TR) and Smith-Purcell radiation (SP). The screen diameter for transition radiation is 40 mm. The SP single electron yield is presented for different beam-grating separation (3 mm, 6 mm and 9 mm). The grating used here is 40×180 mm^2 with 8 mm pitch and 30° blaze angle. The signal is measured as integrated with a 50 mm diameter parabolic mirror located 300 mm from the beam axis. Right: CSPR and CTR energy density as function of wavelength with the same parameters than on the left figure. Both images are taken from [134].
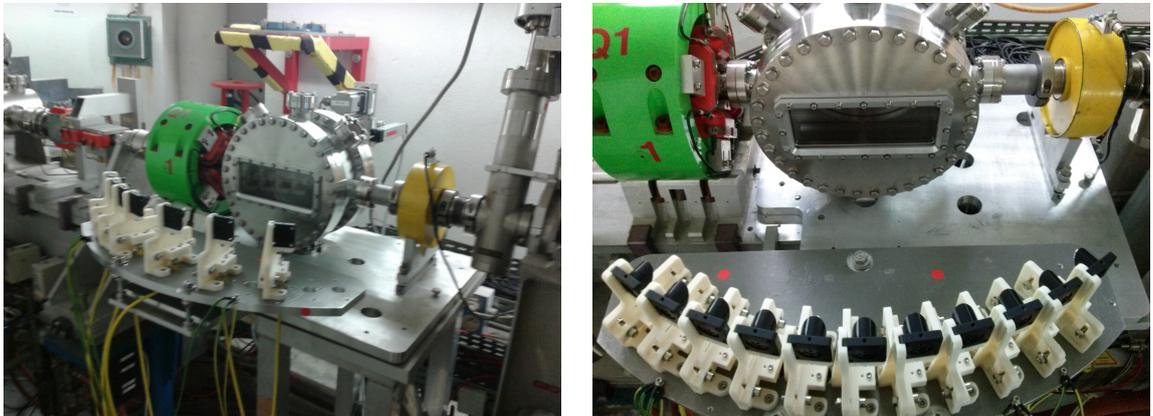
Figure 8.31: The experimental setup for CSPR measurements at CLIO: a set of pyrodectors with off axis parabolic mirrors is placed equidistantly with 7° separation around the window and the experimental chamber with the grating inside (right image taken from [154]). The two images have been taken at different dates and have a different number of detectors.
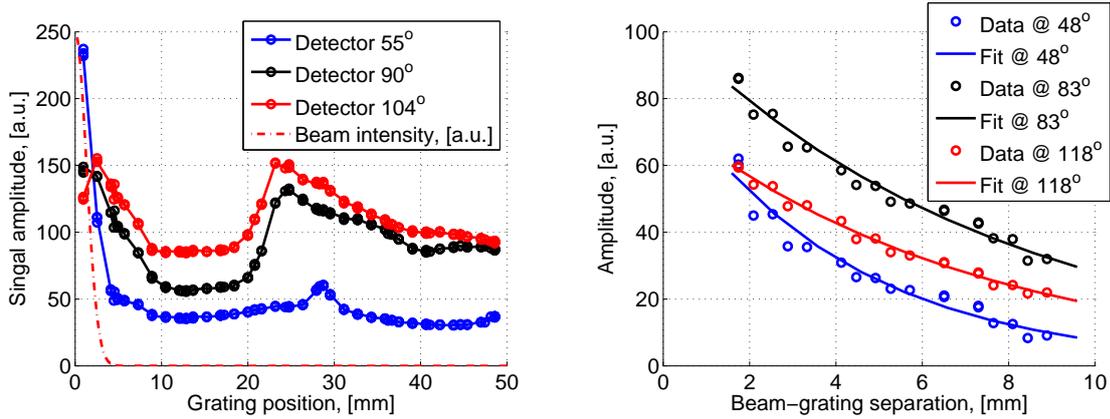
Figure 8.32: Signal amplitude as function of the grating position with respect to the center of the beam for three different detectors angles for a long range (left) and a short range near the beam (right). On the right the data (circles) is compared to a fit (solid line). Images taken form [154]. On the left image the peak between 20 mm and 30 mm is still under investigations.
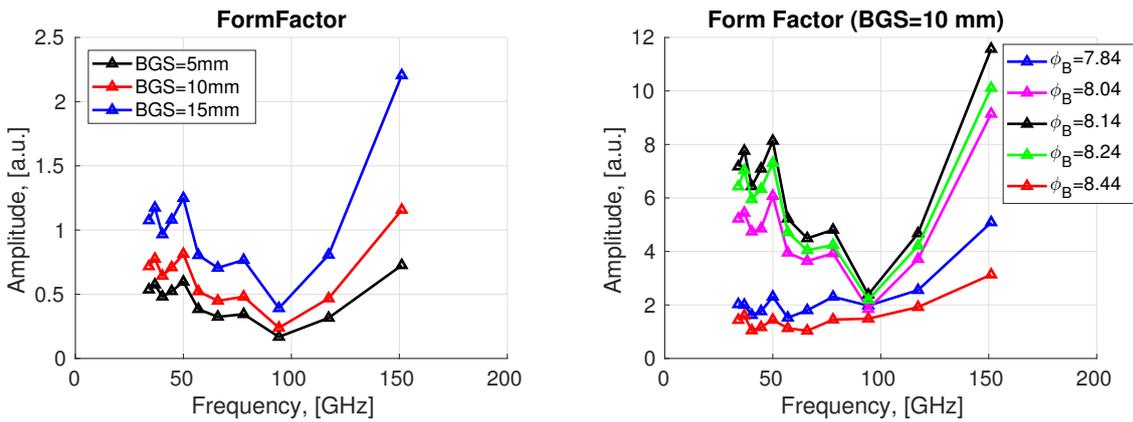
Figure 8.33: Form factor measured at CLIO as reported in [155]. Left: Variation of the form factor when the beam grating separation varies. Right: Variation of the form factor when the buncher phase varies.

8.3.4 Outlook: Application to laser-driven plasma accelerators, ERLs and the ESS

Coherent Smith-Purcell Radiation has the potential to become a single shot diagnostic to measure longitudinal profile.

One of the initial motivation for this diagnostic is to be able to measure the longitudinal profile of beams coming out of plasma accelerators. The very short pulses produced by such accelerator make them a very interesting topic to study and the ESCULAP
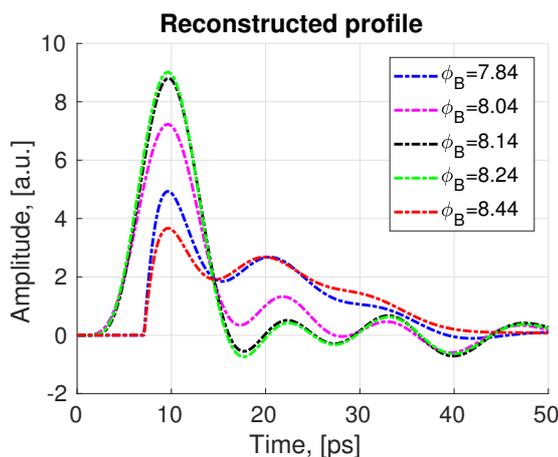
Figure 8.34: Bunche profile reconstructed on CLIO for different buncher phase as reported in [155].
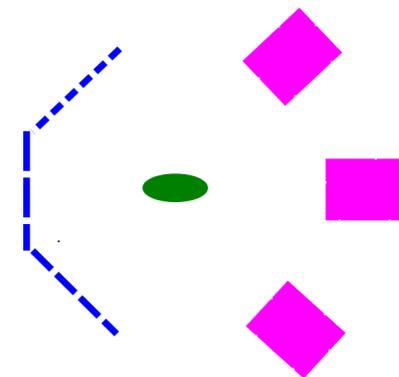
Figure 8.35: Proposed scheme for single show measurement: in the transverse plane three different grating, 60° apart are used to measure three different wavelength ranges from the beam.

facility at LAL (see section 9.1) will offer good testing opportunities. One important question that CSPR should allow to settle on a plasma acceleration experiment is wether the electron pulse has been produced alone or if it accompanied by satellites in the neighboring buckets.

However on the way other applications have appeared. The European Spallation Facility will have ps-bunches in its high energy and their length will have to be measured non destructively. CSPR is well suited for such measure as it is non intercepting and some preliminary studies have been performed [156]. Another location where the non intercepting nature of CSPR combined to the moderate cost of the associated detector can be an advantage is Energy Recovery Linacs (ERL). In an ERL longitudinal deformation of the electron bunch can be amplified at each pass leading to beam disruption. A mon-

104

itor capable of monitoring the bunch profile at several locations without destroying it is therefore important. This can be done by a CSPR monitor.

Chapter 9

Laser-plasma experiments

Recent results of plasma-acceleration experiments, including laser-plasma experiments have been discussed in section 1.4.3. During the past 10 years I have took part in a few laser-driven plasma acceleration experiments [157, 158, 159, 160]. Coming from the conventional accelerators community my contribution has often been on the instrumentation side. I will describe more in details one of them which we are planning at LAL in Orsay.

9.1 ESCULAP

The ESCULAP (ElectronS CoUrts pour l'Accélération Plasma) [25] experiment aims at studying external injection of low energy (10 MeV) electrons in a plasma in the quasilinear regime. This experiment will use the photo injector PHIL [161] and the high power laser LASERIX [162, 163, 164].

The proposed layout of the experiment is shown on figure 9.1 and the most recent description of the experiment is in [165][1].

Preliminary simulations have shown that electrons with an energy of several hundreds of MeV could be produced in such experiment however there are several challenges associated with such experiment:

- Make the high power laser and the accelerator work together with a low jitter between the two machines.

- Compress the electron beam to match it as close as possible to the plasma wavelength.

- Shape the plasma so that it can compress and accelerate the beam.

---

[1]This section is based on text that may also appear in [165].
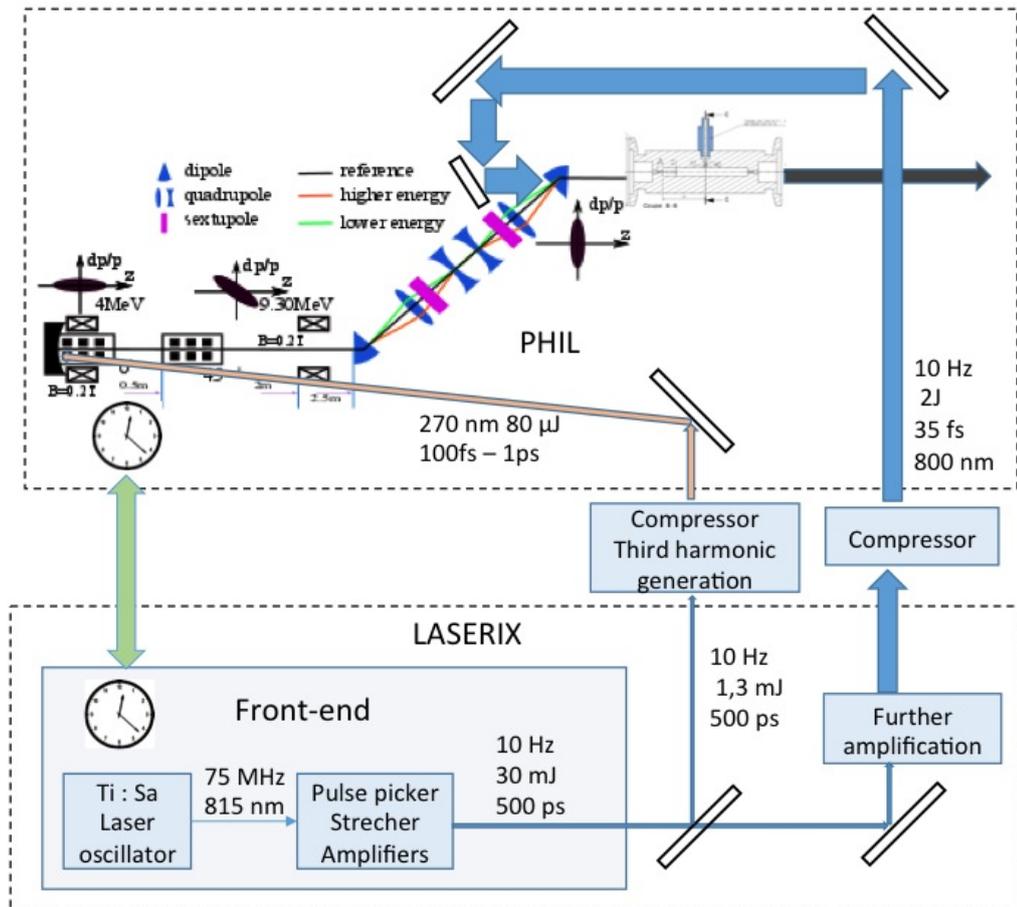
Figure 9.1: The proposed layout for the ESCULAP experiment: the PHIL and Laserix facilities are combined for this external injection laser-driven plasma acceleration experiment as presented in [165].

9.1.1 Simulations

Preliminary simulations of the ESCULAP experiment have been done and reported in [25] and more advanced simulations are under way [166]. The description below is taken mostly from [25].

Plasma acceleration in the linear regime

A high power laser pulse sent in a low density hydrogen or helium gas can ionise it and create a wake characterized by strong electric and magnetic fields. If the pulse is not too intense ($I < 10^{18} \, \text{W/cm}^2$), then the plasma will be weakly driven by the laser pulse, this is called the linear regime [167, 168].

In such conditions we can use or define the following quantities:

- Maximum Accelerating field $E_0 = \frac{2\pi m_e c^2}{e \lambda_p}$ hence

$$E_0[GV/m] = 96.2\sqrt{n_e[10^{18} \, \text{cm}^{-3}]}$$

- Longitudinal accelerating field

$$E_{0z} = \frac{\eta}{4} a_0^2 \cos(k_p d_l) \exp(-\frac{2\rho^2}{w_z^2}) \times E_0$$

- Radial accelerating field

$$E_{0r} = \frac{\rho}{k_p w_z^2} \eta a_0^2 \sin(k_p d_l) \exp(-\frac{2\rho^2}{w_z^2}) \times E_0$$

with m_e the electron mass, e the electron charge, λ the laser wavelength (in our case $\lambda = 0.8 \, \mu\text{m}$), n_e the plasma density, λ_p the plasma wavelength ($\lambda_p = \lambda \times \sqrt{\frac{n_c}{n_e}}$) , k_p the plasma wave number, η the laser-plasma coupling, a_0 the plasma relativistic limit, d_l the laser distance behind the pulse, ρ the radial distance and w_z the laser waist radius at position z (and w_0 is the waist at $z = 0$, the focal point).

Therefore a density of $4 \times 10^{17} \, \text{cm}^{-3}$ will give a maximum longitudinal accelerating field of more than $10 \, \text{GV/m}$. This corresponds to a plasma wavelength of about $50 \, \mu\text{m}$ (that is about $180 \, \text{fs}$). It is important to note also that the radial accelerating field can take either positive or a negative value, that is, it can be either focussing or defocussing.

With a 2 Joules laser focused on a $55 \, \mu\text{m}$ waist we get a Rayleigh length of about $1 \, \text{cm}$. This will give a sufficient length to compress and accelerate the electrons. These electrons must also be focussed in a comparable volume.

Expected electrons distributions

For our simulations we have considered electrons with an energy of 9.5 MeV focussed on a low density H_2 plasma. At the entrance of the plasma the electrons have a transverse size of 170 µm, they are converging with an half-angle of 3 mrad and the FWHM duration of the bunch is 75 fs. The total length of the plasma cell considered is 9 cm but the cell has been designed so that it has a varying pressure according to the profile shown on figure 9.2.
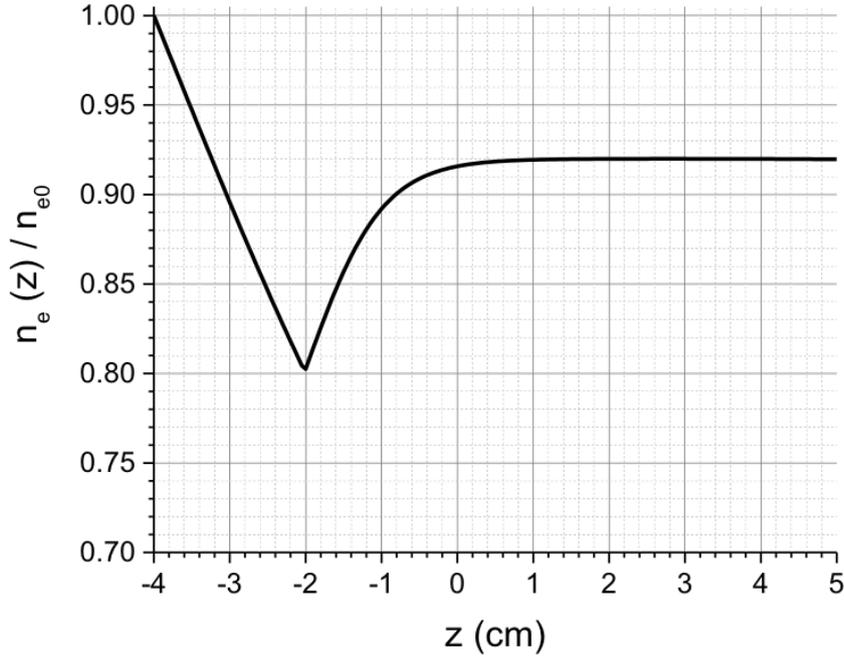
Figure 9.2: Density profile along the plasma axis. The maximum density, n_{e0} is $4 \times 10^{17} \, \text{cm}^{-3}$. Figure taken from [25].

The simulations were done using an adapted version of the numerical code WAKE-EP [169].

The aim of this special density profile is to achieve a radial and longitudinal compression of the electron bunch before its acceleration. The first part of the density profile (decreasing pressure gradient) will keep all the electron together in the focussing phase of the plasma wake. As the electrons have a relatively low γ the difference in accelerating gradient experienced between the head and the tail of the bunch will compress them all together. Once this is achieved the second part of the density profile (increasing pressure gradient) will keep the bunch together at the back of the wave to accelerate them with

110

(a) (b) (c) (d)
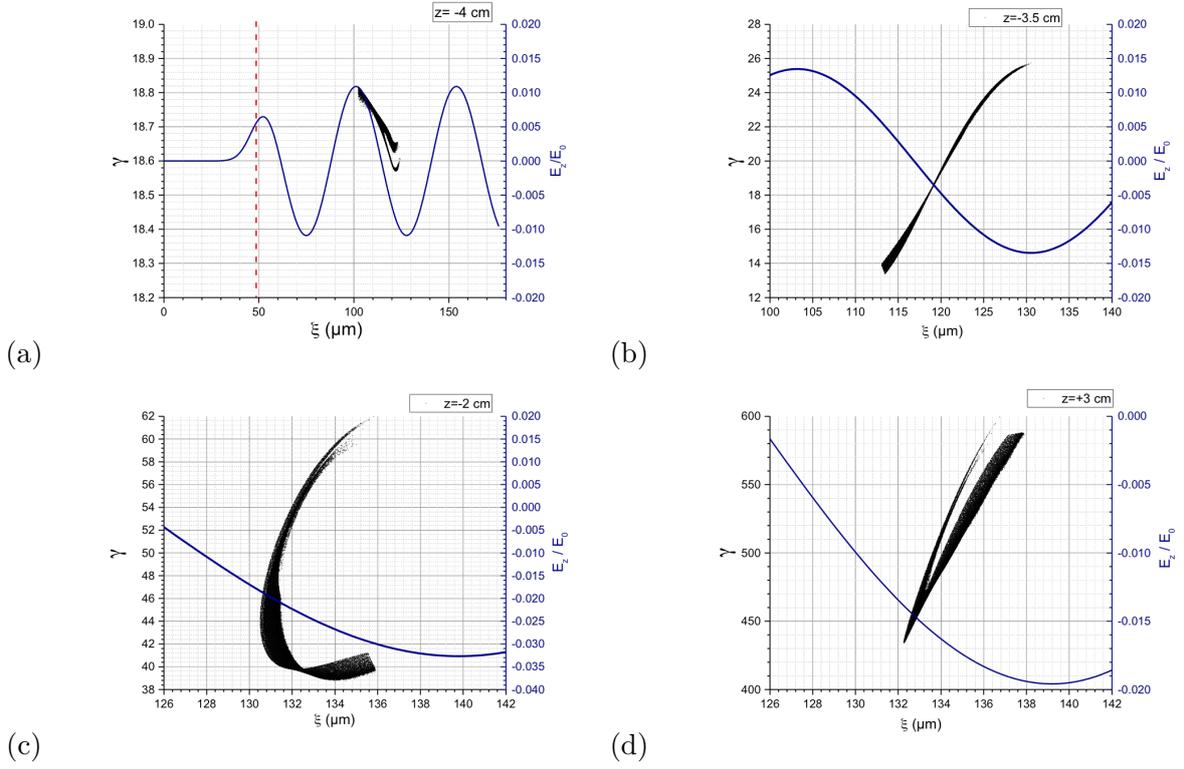
Figure 9.3: Lorentz factor of the electrons (black and left vertical axis) and longitudinal accelerating field divided by $E_0 = mc\omega_p/e = 608\,\text{MV/cm}$ (blue and right vertical axis), versus the distance behind the laser pulse ξ at different z positions in the plasma. Figure taken from [25].

the highest field.

On figure 9.3 (a) one can see the distribution of the electrons (in black) and of the laser wake (in blue) at $z = -4\,\text{cm}$, the entrance of the plasma cell. We can see that at injection the electron bunch (coming from a conventional accelerator simulated using ASTRA [170]) have a large time spread and a small energy spread. As they progress through the decreasing gradient ramp the trailing electrons will experience a higher accelerating field than the electrons at the front. As at these energy they are barely relativistic this difference will result in these electrons almost catching up with the leading one and the beam will get compressed in time. This is illustrated by figure 9.3 (b-c). On figure 9.3 (b) one can see that the distance between the leading and trailing electrons has significantly reduced and the trailing electrons have now more energy than the leading ones. On figure 9.3 (c) the trailing electrons are even overtaking the leading ones and the bunch is compressed in only a few micrometers. It is important to note that this compression completely erases the initial energy spread of the bunch and its time spread. Once this process is over, after $z = -2\,\text{cm}$, the increase in plasma density

111
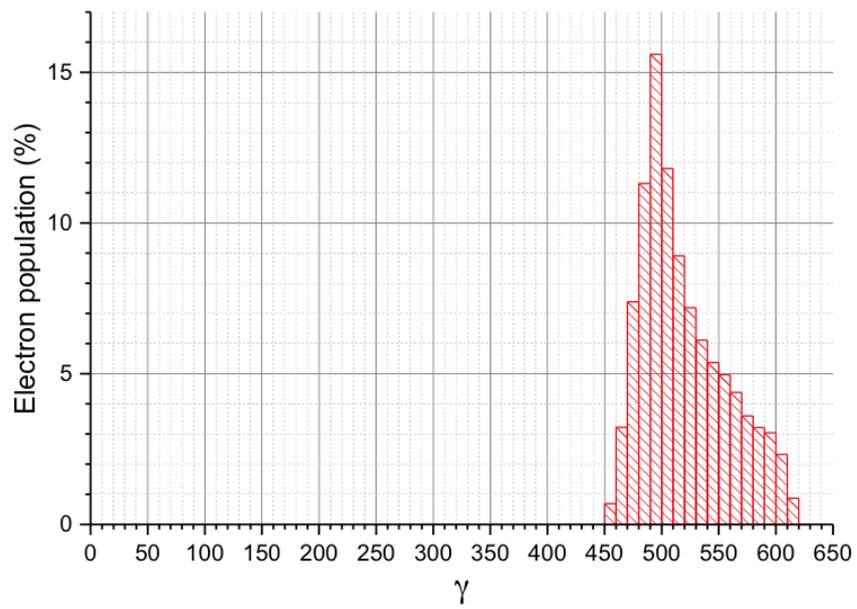
Figure 9.4: Energy distribution at the end of the acceleration process. Figure taken from [25].

and in laser intensity will significantly accelerate the electrons. On figure 9.3 (d) one can see that at the end of the accelerating process the electrons reach a Lorentz factor γ of about 500 with slightly more than 15% energy spread (figure 9.4).

9.1.2 Synchronisation between PHIL and Laserix

For this experiment to be possible the two machines, PHIL and LASERIX must fire at the same time. It was first attempted to directly use LASERIX as clock source for PHIL but this did not work. Therefore I proposed to use the same synchronization scheme for ESCULAP than for ThomX. This scheme has already been discussed in section 6.3. Extensive tests have been made and reported in [66].

The layout specific to ESCULAP is shown in figure 9.5. An example of jitter measurement is shown on figure 9.6 and the trend of the jitter over several minutes is shown on figure 9.7.
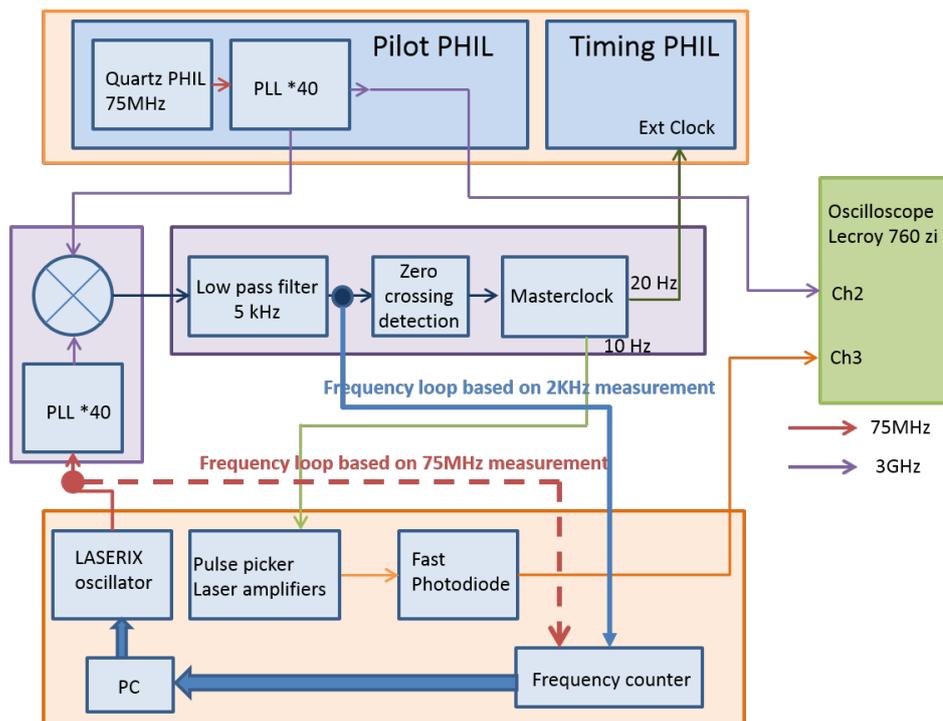
Figure 9.5: The ESCULAP synchronization scheme, combining the current LASERIX synchronization system (at the bottom) and the PHIL synchronization system (at the top). The system used to synchronize the two facilities is shown in the middle. Figure taken from [66].
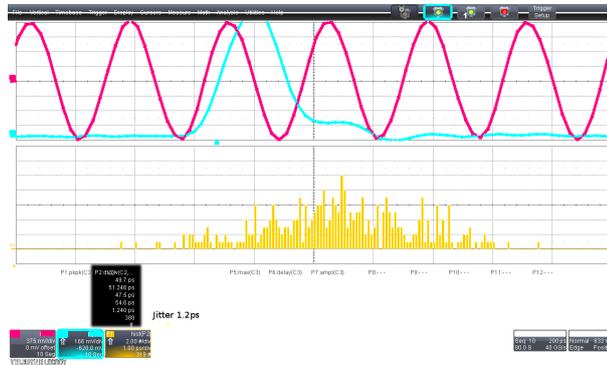
Figure 9.6: Example of jitter measurement between the signal coming from a photodiode recording the LASERIX laser pulse (in light blue) and the signal coming from the 3 GHz RF of PHIL (in red). An ultra-fast scope is used to measure the time between the rise of the photodiode signal above a predefined level and the zero crossing of the RF. The jitter of this measurement is considered to be the jitter between the two machines. Figure taken from [66].
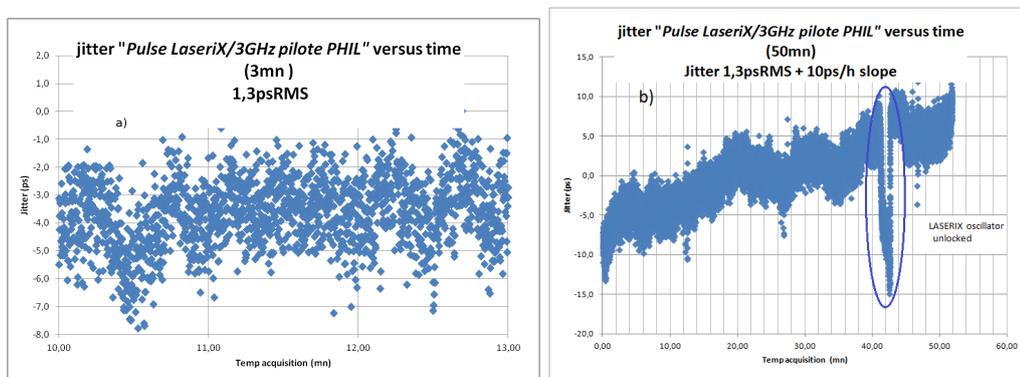
Figure 9.7: Jitter between the photodiode signal from the laser pulse and the 3 GHz from the PHIL RF. On the left figure, the data are recorded during 50 min. On the right figure the data are recorded during 3 min. The drop on the right image is due to a safety stop of the frequency feedback. Figure taken from [66].

114

9.1.3 Compression of the electron bunch

The current beam specifications of the PHIL accelerator are far from those needed for ESCULAP. To reach these performances a compression dogleg chicane will be necessary. This has been studied extensively by graduate student Ke WANG and reported in [171], the layout of this dogleg is shown on figure 9.8. The principle of a compression chicane is to use the beam chirp induced by RF cavities. Dipole magnets are used to disperse the beam according to this chirp. Optical components (quadrupole magnets and sextupole magnets) then give a different travel length depending on the beam energy and a final dipole gather all the electrons back together with a much shorter time spread than before the chicane.
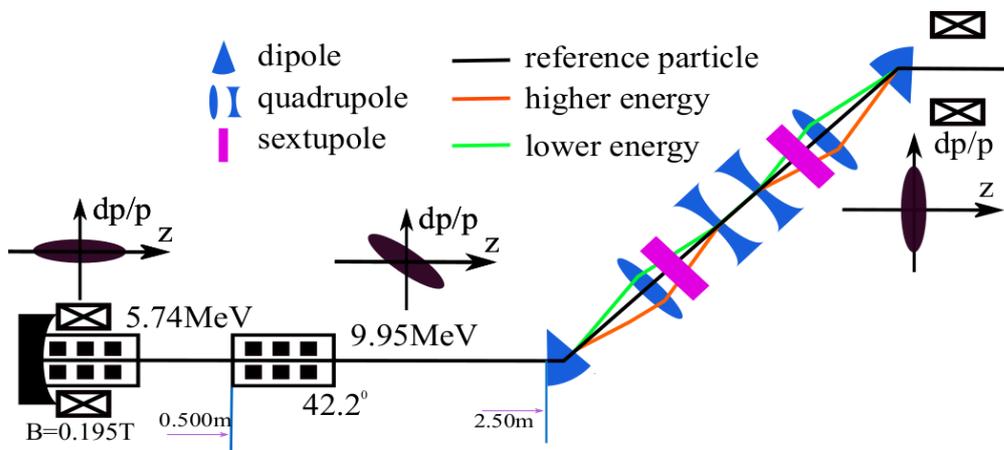
Figure 9.8: Figure taken from [171].

It has been shown in [171] that bunch length much shorter than 150 fs FWHM can be achieved (with the effects of space-charge and Coherent Synchrotron Radiation taken into account), therefore fulfilling our needs for ESCULAP.

9.1.4 The plasma cell

The next challenge to be addressed is to vary the plasma density along the beam axis to match (or come close from) the density profile shown on figure 9.2. Given the low energy at which we will perform the experiments this shaping will be rather important. Several strategies are currently being investigated: either by shaping the channel in which the gas will propagate or by using different gas inlets at different pressures. A preliminary design of such cell is shown on figure 9.9.

The gas pressures required to get the densities we need are at the limit between molecular and viscous flow, making simulations more difficult. We are therefore considering

increase the cell dimensions to be in viscous flow, easier to simulate. This work is in progress.
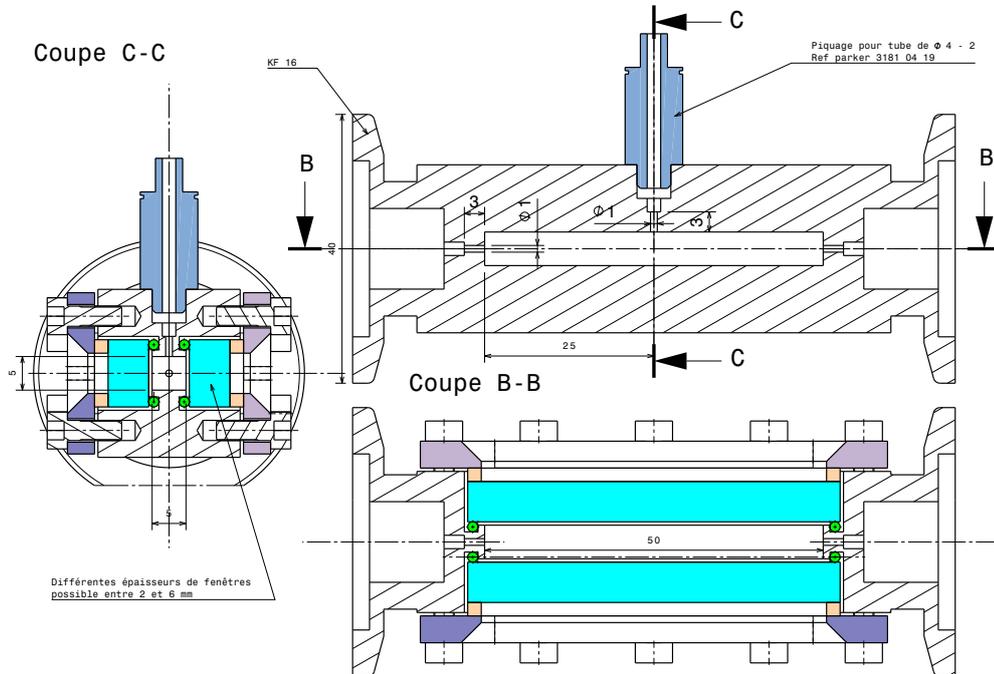
Figure 9.9: Preliminary design of a plasma cell for ESCULAP.

The design phase of ESCULAP should be completed in the coming months and then we hope to move onto the construction of the facility.

9.2 APOLLON and EuPraxia

The ESCULAP experiment is one small contribution among many to the field of plasma acceleration. I am also contributing to two other initiatives of larger amplitude. Near Orsay the multi-petawatt laser APOLLON will soon deliver its first beam and I contribute to the conception of the Long Focal Area where laser-driven plasma acceleration will take place. At the European level the Eupraxia [172] consortium in which I contribute aims at demonstrating practical applications of plasma accelerators, both as a light source and as a tool for high energy physics.

116

9.3 Perspectives and limitations of plasma acceleration as a particle source

The success reported in 2004 and 2006 have set very high expectations of what could be done with plasma accelerators. Two directions were foreseen: Free Electron Lasers and Particle Colliders. More than 10 years later the progress has been slower than expected.

The low emittance and high peak current of the bunch produced by plasma accelerators made them a choice candidate as a source for Free Electron Lasers. However to date no group has achieved this. Although the beam has several desirable qualities its phase space is not match to the requirements of a Free Electron Laser and the shot to shot instabilities of such beam make such matching difficult. Several groups are working on this and are regularly reporting progress.

For a collider the main issue is to reach the beam energy of interest to High Energy Physics. A scheme has been proposed where the beam accelerated by a plasma accelerator is injected in another one [27] but staging experiments are still at an early stage. The large shot to shot instability and the large beam energy spread will also have to be addressed.

The work done at FACET on beam driven acceleration is now pursued at CERN by the AWAKE project [34] where protons will be used to accelerate electrons with a very favorable transformer ratio. This could be used to build a lepton collider with hundreds of GeV in the center of mass.

One should remember that the evolution of particle accelerators has been driven both by user needs but also by what was technologically feasible. The applications of plasma accelerators will benefit from the high accelerating gradients but will have to take into account the limitations of these beams.

Part III

Conclusions

Chapter 10

Sharing the knowledge

I am writing this manuscript as a formal examination to be allowed to direct researches ("Habilitation à diriger des recherches"). During my career so far I have had many opportunities to work with students from all ages. Working with interns or PhD student has always been a pleasure. As much as possible, I have tried to mention their name in this document where I cited work to which their contributed, however I could not mention all of them. Students always bring a fresh look on a problem, sometimes triggering questions on results that were taken for granted. Some students are quick to grab the tasks they have to do and some need more help. On several occasions I have had the pleasure to meet again a former student a few years later at CERN or at a conference and it is always interesting to see what they have become.

The work we do as a researcher can not be dissociated from teaching. At every stage of my career from my graduate studies until now I have been involved in some sort of teaching. Teaching is a good opportunity to revisit our understanding of the underlying physics and the questions asked by the student sometimes shed a completely different light on a well-understood problem.

While I am teaching I like to check that the student are following the lecture by asking quick questions (quizz) every few minutes to check that the notion I just covered was well understood. I noticed that this gives me a better feeling for the level of the students and the parts of the course that need improvement.

Tutorials are always an opportunity to check what individual students have understood. The size of the classes I have taught in tutorials varied from two to forty students, depending on the University, but each time I tried to identify the students who were lacking behind and when possible I discussed with them their difficulties.

To further the awareness of undergraduate students in Europe about particle accelerators and the associated physics, I am coordinating the preparation of a Massive Online Open Course (MOOC) on particle accelerator science and engineering as part of the European Union H2020 project ARIES (Accelerator Research and Innovation for European Science

and Society). This MOOC will make it possible for all students across Europe to learn about particle accelerators even for those from Universities far from accelerator centers. It is expected to be available online around 2019 or 2020.

Finally as a researcher I always keep in mind that I need to inform our society about the work I do (and that is paid for by taxpayers). This is not a new idea, one of the founders of CNRS (Jean Perrin) already had the idea that science had to be shared with the public and he contributed to the foundation of a science museum in Paris ("Palais de la découverte" at the same time to achieve this goal [173]. I regularly give presentation to schools or to the general public about physics in general and more specifically about accelerators when the opportunity arises (see [174] for example). I have had the opportunity to give general public presentations about accelerators in all countries where I worked, including Japan. I also contribute regularly to science magazine for high school students (for example in [175, 176]).

Comparing my experience of publicizing Science to the public in France and in the UK is very interesting: in both country I have been invited several times to the parliament (about four times in six year in each country) to speak of science (and once to the prime minister's residence in the UK). In the UK this was always in my capacity of scientist to present what I was working on and why it needs to be funded. In France, it was always in personal capacity to talk about the societal and ethical implications of science (see for example [177]). This difference can also be found, when engaging with the public: in the UK I had to explain what the science I am doing is worth to the society whereas in France the questions the public asks are more focussed on how it works and what we could do with the potential discovery or how dangerous science can be. This sheds an interesting light on the concerns of both societies.

Chapter 11

Outlook

It has been more than twenty years since I first set foot in a research laboratory as a project student. For me it has been exciting and challenging. I have worked in countries that are very different from each other and found that this has been a very enriching endeavor.

Despite the regular work done by scientists, science progresses by steps: new machines are the trigger for new discoveries. However these machines have to be built part by part, day after day. The efforts I joined when I arrived in France are about to bring their fruits: in the coming months or years, the compact X-ray source ThomX should see its first electrons and the Petawaatt laser APOLLON its first photons at about the same time we expect to accelerate the first electrons on ESCULAP. This will be challenging (and the start of these large projects within a few months of each other will make it even more challenging).

Each of the experiments I have worked on has been an opportunity to learn new techniques and meet new people, students and faculty members.

My initial interest was in High Energy Physics and the lepton sub-structure but then I realized that the current colliders would be limited in their discovery reach and I oriented my research toward new, more powerful machines. This has led me to the R&D on new acceleration techniques.

What will be next? I do not know but I am sure that it will be interesting!

Chapter 12

Acknowledgements

Bibliography

[1] William Crookes. V. the bakerian lecture.—on the illumination of lines of molecular pressure, and the trajectory of molecules. *Philosophical Transactions of the Royal Society of London*, 170:135–164, 1879.

[2] E. Rutherford. Retardation of the α particle from radium in passing through matter. *Philosophical Magazine*, 12(68):134–146, 1906.

[3] H. Geiger and E. Marsden. On a diffuse reflection of the α-particles. *Proceedings of the Royal Society of London A: Mathematical, Physical and Engineering Sciences*, 82(557):495–500, 1909.

[4] Professor Sir E. Ruthefrod F.R.S. Li. collision of α particles with light atoms i. hydrogen. *Philosophical Magazine Series 6*, 37(222):537–561, 1919.

[5] Professor Sir E. Rutherford F.R.S. Liv. collision of α particles with light atoms. iv. an anomalous effect in nitrogen. *Philosophical Magazine Series 6*, 37(222):581–587, 1919.

[6] Rolf Wideröe. Über ein neues prinzip zur herstellung hoher spannungen. *Archiv für Elektrotechnik*, 21(4):387–406, 1928.

[7] J. D. Cockcroft and E. T. S. Walton. Experiments with high velocity positive ions. (i) further developments in the method of obtaining high velocity positive ions. *Proceedings of the Royal Society of London A: Mathematical, Physical and Engineering Sciences*, 136(830):619–630, 1932.

[8] J. D. Cockcroft and E. T. S. Walton. Experiments with high velocity positive ions. ii. the disintegration of elements by high velocity protons. *Proceedings of the Royal Society of London A: Mathematical, Physical and Engineering Sciences*, 137(831):229–242, 1932.

[9] Pierre Marin. *Un demi-siècle d'accélérateurs de particules*. Editions du Dauphin, Paris, 2009.

[10] V. Shiltsev. The first colliders: AdA, VEP-1 and Princeton-Stanford. In *Chapter 2.1 for 'Accelerators for the XXI century' book (Eds. O.Bruning and S.Myers)*. 2013.

[11] Lightsources.org. http://www.lightsources.org/light-source-facility-information.

[12] Lia Merminga. Energy Recovery Linacs. *Conf. Proc.*, C070625:22, 2007. [,22(2007)].

[13] Erk Jensen, Oliver Brüning, Rama Calaga, Karl Schirm, Roberto Torres-Sanchez, Alessandra Valloni, Kurt Aulenbacher, Alex Bogacz, Andrew Hutton, and Max Klein. Plans for an ERL Test Facility at CERN. In *Proceedings, 27th Linear Accelerator Conference, LINAC2014*, page THPP031, 2014.

[14] T. Tajima & J. M. Dawson. Laser electron accelerator. *Phys. Rev. Lett.*, 43:267–270, 1979.

[15] C. E. Clayton, K. A. Marsh, A. Dyson, M. Everett, A. Lal, W. P. Leemans, R. Williams, and C. Joshi. Ultrahigh-gradient acceleration of injected electrons by laser-excited relativistic electron plasma waves. *Phys. Rev. Lett.*, 70:37–40, Jan 1993.

[16] F. Amiranoff, S. Baton, D. Bernard, B. Cros, D. Descamps, F. Dorchies, F. Jacquet, V. Malka, J. R. Marquès, G. Matthieussent, P. Miné, A. Modena, P. Mora, J. Morillo, and Z. Najmudin. Observation of laser wakefield acceleration of electrons. *Phys. Rev. Lett.*, 81:995–998, Aug 1998.

[17] J. Faure et al. A laser-plasma accelerator producing monoenergetic electron beams. *Nature*, 431:541–544, 2004.

[18] C. G. R. Geddes et al. High-quality electron beams from a laser wakefield accelerator using plasma-channel guiding. *Nature*, 431:538–541, 2004.

[19] S. P. D. Mangles et al. Monoenergetic beams of relativistic electrons from intense laser-plasma interactions. *Nature*, 431:535–538, 2004.

[20] W. P. Leemans S. M. Hooker et al. Gev electron beams from a centimetre-scale accelerator. *Nature Physics*, 2:696–699, 2006.

[21] W. P. Leemans, A. J. Gonsalves, H.-S. Mao, K. Nakamura, C. Benedetti, C. B. Schroeder, Cs. Tóth, J. Daniels, D. E. Mittelberger, S. S. Bulanov, J.-L. Vay, C. G. R. Geddes, and E. Esarey. Multi-gev electron beams from capillary-discharge-guided subpetawatt laser pulses in the self-trapping regime. *Phys. Rev. Lett.*, 113:245002, Dec 2014.

[22] S. M. Hooker. Developments in laser-driven plasma accelerators. *Nat Photon*, 7(10):775–782, 10 2013.

[23] Andrea R. Rossi, Alberto Bacci, Marco Belleveglia, Enrica Chiadroni, Alessandro Cianchi, Giampiero Di Pirro, Massimo Ferrario, Alessandro Gallo, Giancarlo Gatti, Cesare Maroli, Andrea Mostacci, Vittoria Petrillo, Luca Serafini, Paolo Tomassini, and Cristina Vaccarezza. The external-injection experiment at the sparc_lab facility. *Nuclear Instruments and Methods in Physics Research Section*

A: Accelerators, Spectrometers, Detectors and Associated Equipment, 740:60 – 66, 2014. Proceedings of the first European Advanced Accelerator Concepts Workshop 2013.

[24] U. Dorda et al. SINBAD—The accelerator R&D; facility under construction at DESY. *Nucl. Instrum. Meth.*, A829:233–236, 2016.

[25] Nicolas Delerue, Christelle Bruni, Stéphane Jenzer, Sophie Kazamias, Bruno Lucas, Gilles Maynard, and Moana Pittman. Simulations of the Acceleration of Externally Injected Electrons in a Plasma Excited in the Linear Regime. In *IPAC'16, WEPMY0003*, 2016.

[26] S. Steinke, J. van Tilborg, C. Benedetti, C. G. R. Geddes, C. B. Schroeder, J. Daniels, K. K. Swanson, A. J. Gonsalves, K. Nakamura, N. H. Matlis, B. H. Shaw, E. Esarey, and W. P. Leemans. Multistage coupling of independent laser-plasma accelerators. *Nature*, 530(7589):190–193, 02 2016.

[27] C. B. Schroeder, E. Esarey, C. G. R. Geddes, C. Benedetti, and W. P. Leemans. Physics considerations for laser-plasma linear colliders. *Phys. Rev. ST Accel. Beams*, 13:101301, Oct 2010.

[28] R. A. Snavely, M. H. Key, S. P. Hatchett, T. E. Cowan, M. Roth, T. W. Phillips, M. A. Stoyer, E. A. Henry, T. C. Sangster, M. S. Singh, S. C. Wilks, A. MacKinnon, A. Offenberger, D. M. Pennington, K. Yasuike, A. B. Langdon, B. F. Lasinski, J. Johnson, M. D. Perry, and E. M. Campbell. Intense high-energy proton beams from petawatt-laser irradiation of solids. *Phys. Rev. Lett.*, 85:2945–2948, Oct 2000.

[29] Andrea Macchi, Marco Borghesi, and Matteo Passoni. Ion acceleration by super-intense laser-plasma interaction. *Rev. Mod. Phys.*, 85:751–793, May 2013.

[30] Ian Blumenfeld, Christopher E. Clayton, Franz-Josef Decker, Mark J. Hogan, Chengkun Huang, Rasmus Ischebeck, Richard Iverson, Chandrashekhar Joshi, Thomas Katsouleas, Neil Kirby, Wei Lu, Kenneth A. Marsh, Warren B. Mori, Patric Muggli, Erdem Oz, Robert H. Siemann, Dieter Walz, and Miaomiao Zhou. Energy doubling of 42[thinsp]gev electrons in a metre-scale plasma wakefield accelerator. *Nature*, 445(7129):741–744, 02 2007.

[31] M. Litos, E. Adli, W. An, C. I. Clarke, C. E. Clayton, S. Corde, J. P. Delahaye, R. J. England, A. S. Fisher, J. Frederico, S. Gessner, S. Z. Green, M. J. Hogan, C. Joshi, W. Lu, K. A. Marsh, W. B. Mori, P. Muggli, N. Vafaei-Najafabadi, D. Walz, G. White, Z. Wu, V. Yakimenko, and G. Yocky. High-efficiency acceleration of an electron beam in a plasma wakefield accelerator. *Nature*, 515(7525):92–95, 11 2014.

[32] S. Corde, E. Adli, J. M. Allen, W. An, C. I. Clarke, C. E. Clayton, J. P. Delahaye, J. Frederico, S. Gessner, S. Z. Green, M. J. Hogan, C. Joshi, N. Lipkowitz, M. Litos, W. Lu, K. A. Marsh, W. B. Mori, M. Schmeltz, N. Vafaei-Najafabadi, D. Walz,

V. Yakimenko, and G. Yocky. Multi-gigaelectronvolt acceleration of positrons in a self-loaded plasma wakefield. *Nature*, 524(7566):442–445, 08 2015.

[33] M. Ferrario, D. Alesini, M. Anania, A. Bacci, M. Bellaveglia, O. Bogdanov, R. Boni, M. Castellano, E. Chiadroni, A. Cianchi, S.B. Dabagov, C. De Martinis, D. Di Giovenale, G. Di Pirro, U. Dosselli, A. Drago, A. Esposito, R. Faccini, A. Gallo, M. Gambaccini, C. Gatti, G. Gatti, A. Ghigo, D. Giulietti, A. Ligidov, P. Londrillo, S. Lupi, A. Mostacci, E. Pace, L. Palumbo, V. Petrillo, R. Pompili, A.R. Rossi, L. Serafini, B. Spataro, P. Tomassini, G. Turchetti, C. Vaccarezza, F. Villa, G. Dattoli, E. Di Palma, L. Giannessi, A. Petralia, C. Ronsivalle, I. Spassovsky, V. Surrenti, L. Gizzi, L. Labate, T. Levato, and J.V. Rau. Sparc_lab present and future. *Nuclear Instruments and Methods in Physics Research Section B: Beam Interactions with Materials and Atoms*, 309:183 – 188, 2013. The 5th International Conference 'Channeling 2012', 'Charged Neutral Particles Channeling Phenomena' September 23-28,2012, Alghero (Sardinia), Italy.

[34] Allen Caldwell, Konstantin Lotov, Alexander Pukhov, and Frank Simon. Proton-driven plasma-wakefield acceleration. *Nat Phys*, 5(5):363–367, 05 2009.

[35] P Muggli, E Adli, R Apsimon, F Asmus, R Baartman, A-M Bachmann, M Barros Marin, F Batsch, J Bauche, V K Berglyd Olsen, M Bernardini, B Biskup, E Blanco Vinuela, A Boccardi, T Bogey, T Bohl, C Bracco, F Braunmuller, S Burger, G Burt, S Bustamante, B Buttenschön, A Butterworth, A Caldwell, M Cascella, E Chevallay, M Chung, H Damerau, L Deacon, A Dexter, P Dirksen, S Doebert, J Farmer, V Fedosseev, T Feniet, G Fior, R Fiorito, R Fonseca, F Friebel, P Gander, S Gessner, I Gorgisyan, A A Gorn, O Grulke, E Gschwendtner, A Guerrero, J Hansen, C Hessler, W Hofle, J Holloway, M Hüther, M Ibison, M R Islam, L Jensen, S Jolly, M Kasim, F Keeble, S-Y Kim, F Kraus, A Lasheen, T Lefevre, G LeGodec, Y Li, S Liu, N Lopes, K V Lotov, M Martyanov, S Mazzoni, D Medina Godoy, O Mete, V A Minakov, R Mompo, J Moody, M T Moreira, J Mitchell, C Mutin, P Norreys, E Öz, E Ozturk, W Pauw, A Pardons, C Pasquino, K Pepitone, A Petrenko, S Pitmann, G Plyushchev, A Pukhov, K Rieger, H Ruhl, J Schmidt, I A Shalimova, E Shaposhnikova, P Sherwood, L Silva, A P Sosedkin, R Speroni, R I Spitsyn, K Szczurek, J Thomas, P V Tuev, M Turner, V Verzilov, J Vieira, H Vincke, C P Welsch, B Williamson, M Wing, G Xia, H Zhang, and The AWAKE collaboration. Awake readiness for the study of the seeded self-modulation of a 400 gev proton bunch. *Plasma Physics and Controlled Fusion*, 60(1):014046, 2018.

[36] Christopher M. S. Sears, Eric Colby, R. J. England, Rasmus Ischebeck, Christopher McGuinness, Janice Nelson, Robert Noble, Robert H. Siemann, James Spencer, Dieter Walz, Tomas Plettner, and Robert L. Byer. Phase stable net acceleration of electrons from a two-stage optical accelerator. *Phys. Rev. ST Accel. Beams*, 11:101301, Oct 2008.

[37] P Rullhusen, X Artru, and P Dhez. *Novel radiation sources using relativistic electrons: from infrared to x-rays*. Synchrotr Radiat. Techniques Appl. World Scientific, Singapore, 1998.

[38] Avinash Puntambekar et al. ILC Reference Design Report: ILC Global Design Effort and World Wide Study. 2007.

[39] R Alley, D Arnett, E Bong, W Colocho, J Frisch, S Horton-Smith, W Inman, K Jobe, T Kotseroglou, D McCormick, J Nelson, M Scheeff, S Wagner, and M.C Ross. Proceedings of the sixth international conference on instrumentation for experiments at e+ e- colliders a laser-based beam profile monitor for the slc/sld interaction region. *Nuclear Instruments and Methods in Physics Research Section A: Accelerators, Spectrometers, Detectors and Associated Equipment*, 379(3):363 – 365, 1996.

[40] Y. Liu, A. Aleksandrov, S. Assadi, W. Blokland, C. Deibele, W. Grice, C. Long, T. Pelaia, and A. Webster. Laser wire beam profile monitor in the spallation neutron source (sns) superconducting linac. *Nuclear Instruments and Methods in Physics Research Section A: Accelerators, Spectrometers, Detectors and Associated Equipment*, 612(2):241 – 253, 2010.

[41] David Lee, Jürgen Pozimski, Peter Savage, and Christoph Gabor. A Laser-Based Beam Profile Measuring Instrument for the Front End Test Stand at RAL. In *Particle accelerator. Proceedings, 23rd Conference, PAC'09, Vancouver, Canada, May 4-8, 2009*, page TH5RFP051, 2010.

[42] Zemax LLC. Zemax, optical design software. http://www.zemax.com.

[43] Nicolas Delerue et al. Status of the ATF extraction line laser-wire. *ArXiV physics/0601123*, 2005.

[44] Stewart T. Boogert, Grahame A. Blair, Gary Boorman, Alessio Bosco, Lawrence C. Deacon, Pavel Karataev, Alexander Aryshev, Masafumi Fukuda, Nobihiro Terunuma, Junji Urakawa, Laura Corner, Nicolas Delerue, Brian Foster, David Howell, Myriam Newman, Rohan Senanayake, Roman Walczak, and Fred Ganaway. Micron-scale laser-wire scanner for the kek accelerator test facility extraction line. *Phys. Rev. ST Accel. Beams*, 13:122801, Dec 2010.

[45] J. Urakawa et al. Recent Results on KEK/ATF Damping Ring. In *Proceedings, 17th International Conference on High-Energy Accelerators, HEACC 1998: Dubna, Russian Federation, September 07–12, 1998*, pages 117–119, 1998.

[46] S. Dixit et al. A study of laser system requirements for application in beam diagnostics and polarimetry at the ILC. *Conf. Proc.*, C060626:741–743, 2006. [,741(2006)].

[47] Y. Zaouter, E. Mottay, L. Corner, and N. Delerue. Ultrafast amplified fiber laser for laser-wire measurements in particle accelerators, 2008.

131

[48] Laurence Nevay, Grahame A. Blair, Stewart Boogert, Laura Corner, Nicolas Delerue, David Howell, Myriam Newman, Roman Walczak, and Benjamin Rosenberger. Development of a Photonic Crystal Fibre Laser Amplifier for Particle Beam Diagnostics. In *Particle accelerator. Proceedings, 23rd Conference, PAC'09, Vancouver, Canada, May 4-8, 2009*, page TH5RFP098, 2010.

[49] S. Baudrand et al. A High Precision Fabry-Perot Cavity Polarimeter at HERA. *JINST*, 5:P06005, 2010.

[50] J. Bonis et al. Non-planar four-mirror optical cavity for high intensity gamma ray flux production by pulsed laser beam Compton scattering off GeV-electrons. *JINST*, 7:P01017, 2012.

[51] Nicolas Delerue et al. High flux polarized gamma rays production: first measurements with a four-mirror cavity at the ATF. *Conf. Proc.*, C110904:1446–1448, 2011.

[52] T. Akagi et al. Production of gamma rays by pulsed laser beam Compton scattering off GeV-electrons using a non-planar four-mirror optical cavity. *JINST*, 7:P01021, 2012.

[53] Iryna Chaikovska. *Polarized positron sources for the future linear colliders*. PhD thesis, U. Paris-Sud 11, Dept. Phys., Orsay, 2012.

[54] Pierre Favier. *These.* PhD thesis, Université Paris-Saclay, 2017.

[55] I. Chaikovska, K. Cassou, R. Chiche, R. Cizeron, P. Cornebise, N. Delerue, D. Jehanno, F. Labaye, R. Marie, A. Martens, Y. Peinaud, V. Soskov, A. Variola, F. Zomer, E. Cormier, J. Lhermite, V. Dolique, R. Flaminio, C. Michel, L. Pinard, B. Sassolas, T. Akagi, S. Araki, Y. Honda, T. Omori, N. Terunuma, J. Urakawa, S. Miyoshi, T. Takahashi, and H. Yoshitama. High flux circularly polarized gamma beam factory: coupling a fabry-perot optical cavity with an electron storage ring. *Scientific Reports*, 6:36569 EP –, 11 2016.

[56] I. Chaikovska, C. Bruni, N. Delerue, A. Variola, F. Zomer, K. Kubo, T. Naito, T. Omori, N. Terunuma, and J. Urakawa. Effect of Compton Scattering on the Electron Beam Dynamics at the ATF Damping Ring. *Conf. Proc.*, C110904:2127–2129, 2011.

[57] K. Kubo et al. Extremely low vertical emittance beam in accelerator test facility at KEK. *Phys. Rev. Lett.*, 88:194801, 2002.

[58] K. Dupraz et al. Design and optimization of a highly efficient optical multipass system for γ-ray beam production from electron laser beam Compton scattering. *Phys. Rev. ST Accel. Beams*, 17(3):033501, 2014.

[59] O. Adriani et al. Technical Design Report EuroGammaS proposal for the ELI-NP Gamma beam System. 2014.

[60] Variola et. al. ThomX TDR. *LAL/RT 14-21 SOLEIL/SOU-RA-3269*, 2014.

[61] Illya Drebot. *Electron beam dynamics with and without Compton back scattering.* Theses, Université Paris Sud - Paris XI, November 2013.

[62] N. Delerue, C. Bruni, I Chaikovska, I. Drebot, M. Jacquet, A. Variola, F. Zomer, and A. Loulergue. Effect of Beam Dynamics Processes in the Low Energy Ring ThomX. In *Proceedings, 5th International Particle Accelerator Conference (IPAC 2014): Dresden, Germany, June 15-20, 2014*, page WEPRO001, 2014.

[63] K. Yokoya T. Tauchi and P. Chen. Cain. *Part. Acc.*, 41(29), 1993.

[64] T. Naito, H. Hayano, T. Korhonen, S. Takeda, and J. Urakawa. Timing system of the ATF. In *International Conference on Accelerator and Large Experimental Physics Control Systems (ICALEPCS 97) Beijing, China, November 3-7, 1997*, 1997.

[65] T. Naito, H. Hayano, and J. Urakawa. Timing system for multibunch - multitrain operation at ATF - DR. In *Accelerator science and technology. 12th Symposium, SAST'99, Wako, Japan, October 27-29, 1999*, pages 552–554, 1999.

[66] Nicolas Delerue et al. Synchronization of a Photo-Injector and a High Power Laser With Independent Clocks. In *Proceedings, 8th International Particle Accelerator Conference (IPAC 2017): Copenhagen, Denmark, May 14-19, 2017*, page THPAB093, 2017.

[67] M. Zhang. Emittance formula for slits and pepper-pot measurement. *Fermilab-TM-1988, October*, 1996.

[68] Nicolas Delerue. Single Shot Transverse Emittance Measurement of multi-MeV Electron Beams Using a Long Pepper-Pot. *Nucl. Instrum. Meth.*, A644:1–10, 2011.

[69] M. McCann. Measuring low energy beam emittance using the pepper pot method. *Summer internship report*, 2007.

[70] S. Agostinelli et al. Geant4: A simulation toolkit. *Nucl. Instrum. Meth.*, A506:250–303, 2003.

[71] J. Hewlett. Pepperpot report. *Summer internship report*, 2007.

[72] A. Ghigo, G. Mazzitelli, F. Sannibale, P. Valente, and G. Vignola. Commissioning of the DAFNE beam test facility. *Nucl. Instrum. Meth.*, A515:524–542, 2003.

[73] B. Buonomo, G. Mazzitelli, and P. Valente. Performance and upgrade of the DAFNE Beam Test Facility (BTF). *IEEE Trans. Nucl. Sci.*, 52:824–829, 2005.

[74] P. Valente, B. Buonomo, and G. Mazzitelli. Diagnostics and upgrade of the DAFNE Beam Test Facility (BTF). *Nucl. Phys. Proc. Suppl.*, 150:362–365, 2006. [,362(2006)].

[75] Nicolas Delerue et al. Single-Shot Emittance Measurement of a 508MeV Electron Beam Using the Pepper-Pot Method. In *Particle accelerator. Proceedings, 23rd Conference, PAC'09, Vancouver, Canada, May 4-8, 2009*, page TH5RFP065, 2010.

[76] C. Thomas, N. Delerue, and R. Bartolini. Single shot 3 GeV electron transverse emittance with a pepper-pot. *Nuclear Instruments and Methods in Physics Research Section A: Accelerators, Spectrometers, Detectors and Associated Equipment*, 729:554–556, 2013.

[77] W. M. Yao et al. Review of particle physics. *J. Phys.*, G33:1–1232, 2006.

[78] MA Tordeux and J Papadacci. Electron beam transverse emittance measurement using optical transition radiation interferometry. *EPAC 1996 - TUP013L*, 1996. EPAC 1996.

[79] K. T. McDonald and D. P. Russell. Methods of emittance measurement. *Lect. Notes Phys.*, 343:122–132, 1989.

[80] C Thomas, N Delerue, and R Bartolini. Single shot transverse emittance measurement from otr screens in a drift transport section. *Journal of Instrumentation*, 6(07):P07004, 2011.

[81] J. Rossbach and P. Schüser. Basic course on accelerator optics. *CERN Accelerator School*, CERN 94-01, 1994.

[82] Gerald R. Lynch and Orin I. Dahl. Approximations to multiple Coulomb scattering. *Nucl. Instrum. Meth.*, B58:6–10, 1991.

[83] J. Apostolakis et al. Geant4 low energy electromagnetic models for electrons and photons. CERN-OPEN-99-034.

[84] S. Chauvie et al. Geant4 low energy electromagnetic physics. Prepared for CHEP'01: Computing in High-Energy Physics and Nuclear, Beijing, China, 3-7 Sep 2001.

[85] V.A Verzilov. Transition radiation in the pre-wave zone. *Physics Letters A*, 273(1–2):135 – 140, 2000.

[86] M. Bergamaschi et al. Experimental study of optical transition radiation interference. In *RREPS'15*, volume Oral presentation of *RREPA*, https://indico.cern.ch/event/378549/contributions/1803855/, 2015.

[87] S. V. Trofymenko, N. F. Shul'ga, N. Delerue, S. Jenzer, V. Khodnevych, and A. Migayron. Proposal to observe half-bare electrons on a 45-MeV linac. *J. Phys. Conf. Ser.*, 874(1):012076, 2017.

[88] A. Simic. Electron tracking in nuclear emulsions. *Summer internship report*, 2007.

[89] N. Shipman. Using phase correlation for image registration. *Summer internship report*, 2008.

[90] N. Shipman. Study of emulsions data taken at the btf. *Summer internship report*, 2009.

[91] B.-J. Zandt. Otr simulations and measurements. *Project internship report*, 2008.

[92] F. G. Bisesto, M. P. Anania, A. Cianchi, E. Chiadroni, A. Curcio, M. Ferrario, R. Pompili, and A. Zigler. Innovative single-shot diagnostics for electrons from laser wakefield acceleration at FLAME. *J. Phys. Conf. Ser.*, 874(1):012035, 2017.

[93] Bergoz http://www.bergoz.com/ict-bcm-ihr.

[94] G. Devanz, B. Leblond, B. Mouton, and C. Travier. Bunch length measurement on CANDELA photoinjector. *Conf. Proc.*, C9608262:761–763, 1996.

[95] C. M. Thomas and G. Rehm. Diamond optical diagnostics: First streak camera measurements. *Conf. Proc.*, C060626:1112–1114, 2006. [,1112(2006)].

[96] M.-E. Couprie R. Nagaoka D. Pedeau M. Labat, L. Cassinari. Streak camera measurements of the soleil bunch length. In *Proceedings, DIPAC 2007*, page wepb05, 2007.

[97] Valery A. Dolgashev, Gordon Bowden, Yuantao Ding, Paul Emma, Patrick Krejcik, James Lewandowski, Cecile Limborg, Michael Litos, Juwen Wang, and Dao Xiang. Design and application of multimegawatt x-band deflectors for femtosecond electron beam diagnostics. *Phys. Rev. ST Accel. Beams*, 17:102801, Oct 2014.

[98] TCAV Group SLAC. https://portal.slac.stanford.edu/sites/ard_public/facet/facilities/Pages/TCAV.aspx.

[99] F. Glotin, J.-M. Berset, R. Chaput, D. A. Jaroszynski, J.-M. Ortéga, and R. Prazérès. Bunch length measurements on CLIO. *Nuclear Instruments and Methods in Physics Research A*, 341:49–53, March 1994.

[100] Thomas Vinatier, Christelle Bruni, Sophie Chancé, and Patrick Puzo. Length Measurement of High-brightness Electron Beam thanks to the 3-Phase Method. In *Proceedings, 5th International Particle Accelerator Conference (IPAC 2014): Dresden, Germany, June 15-20, 2014*, page THPME095, 2014.

[101] X. Yan, A. M. MacLeod, W. A. Gillespie, G. M. H. Knippels, D. Oepts, A. F. G. van der Meer, and W. Seidel. Subpicosecond electro-optic measurement of relativistic electron pulses. *Phys. Rev. Lett.*, 85:3404–3407, Oct 2000.

[102] Y Parc, Changbum Kim, Jung Yun Huang, Jangho Park, Taiha Joo, and In Soo Ko. A study of electro-optical crystal as a diagnostic tool for low energy electron beam. *JOURNAL-KOREAN PHYSICAL SOCIETY*, 50(5):1390, 2007.

[103] H. Tomizawa, T. Sato, K. Ogawa, K. Togawa, T. Tanaka, T. Hara, M. Yabashi, H. Tanaka, T. Ishikawa, T. Togashi, and et al. Stabilization of a high-order harmonic generation seeded extreme ultraviolet free electron laser by time-

synchronization control with electro-optic sampling. *High Power Laser Science and Engineering*, 3, 2015.

[104] T. J Maxwell, C. Beherens, Y. Ding, A. S. Fisher, J. Frisch, Z. Huang, and H. Loos. Coherent Radiation Spectroscopy of Few-Femtosecond Electron Bunches Using a Middle-Infrared Prism Spectrometer. *Phys. Rev. Lett.*, 111(18):184801, 2013.

[105] E. Chiadroni, M. Bellaveglia, P. Calvani, M. Castellano, L. Catani, A. Cianchi, G. Di Pirro, M. Ferrario, G. Gatti, O. Limaj, S. Lupi, B. Marchetti, A. Mostacci, E. Pace, L. Palumbo, C. Ronsivalle, R. Pompili, and C. Vaccarezza. Characterization of the thz radiation source at the frascati linear accelerator. *Review of Scientific Instruments*, 84(2):022703, 2013.

[106] Stephan Wesch, Bernhard Schmidt, Christopher Behrens, Hossein Delsim-Hashemi, and Peter Schmuser. A Multi-Channel THz and Infrared Spectrometer for Femtosecond Electron Bunch Diagnostics by Single-Shot Spectroscopy of Coherent Radiation. *Nucl. Instrum. Meth.*, A665:40–47, 2011.

[107] M. D. Litos, M. R. Bionta, V. A. Dolgashev, R. J. England, D. Fritz, S. Gilevich, Ph. Hering, and M. J. Hogan. Evaluation of Temporal Diagnostic Techniques for Two-Bunch FACET Beam. *Conf. Proc.*, C110328:568–570, 2011.

[108] S. J. Smith and E. M. Purcell. Visible light from localized surface charges moving across a grating. *Phys. Rev.*, 92:1069–1069, Nov 1953.

[109] G. Doucas, J. H. Mulvey, M. Omori, J. Walsh, and M. F. Kimmitt. First observation of smith-purcell radiation from relativistic electrons. *Phys. Rev. Lett.*, 69:1761–1764, Sep 1992.

[110] K. Ishi, Y. Shibata, T. Takahashi, S. Hasebe, M. Ikezawa, K. Takami, T. Matsuyama, K. Kobayashi, and Y. Fujita. Observation of coherent smith-purcell radiation from short-bunched electrons. *Phys. Rev. E*, 51:R5212–R5215, Jun 1995.

[111] K. Ishiguro and T. Tako. An Estimation of Smith-Purcell Effect as the Light Source in the Infra-red Region. *Optica Acta*, 8:25–31, 1961.

[112] G. Toraldo di Francia. On the theory of some Čerenkovian effects. *Il Nuovo Cimento*, 16:61–77, April 1960.

[113] D. V. Karlovets and A. P. Potylitsyn. Comparison of smith-purcell radiation models and criteria for their verification. *Phys. Rev. ST Accel. Beams*, 9:080701, Aug 2006.

[114] M.S. Malovytsia and N. Delerue. Comparison of the Smith-purcell Radiation Yield for Different Models . In *IPAC2016*, Proceedings of IPAC2016, page MOPMB004, Busan, South Korea, May 2016.

[115] D.V. Karlovets and A.P. Potylitsyn. Smith-purcell radiation in the ?pre-wave? zone. *JETP Letters*, 84(9):489–493, 2007.

[116] J. H. Brownell, J. Walsh, and G. Doucas. Spontaneous Smith-Purcell radiation described through induced surface currents. *Phys. Rev. E*, 57:1075–1080, Jan 1998.

[117] C.A. Ekdahl. High power microwave generator, June 24 1986. US Patent 4,596,967.

[118] J. M. Wachtel. Free-electron lasers using the smith-purcell effect. *Journal of Applied Physics*, 50(1):49–56, 1979.

[119] Levi Schächter and Amiram Ron. Smith-purcell free-electron laser. *Phys. Rev. A*, 40:876–896, Jul 1989.

[120] H. L. Andrews and C. A. Brau. Gain of a smith-purcell free-electron laser. *Phys. Rev. ST Accel. Beams*, 7:070701, Jul 2004.

[121] J. Gardelle, P. Modin, and J. T. Donohue. Start current and gain measurements for a smith-purcell free-electron laser. *Phys. Rev. Lett.*, 105:224801, Nov 2010.

[122] C. Brau, C. Boulware, and H. Andrews. Smith-purcell free electron laser and method of operating same, March 23 2006. US Patent App. 11/172,429.

[123] D.C. Nguyen. Measuring short electron bunch lengths using coherent smith-purcell radiation, March 30 1999. US Patent 5,889,797.

[124] A. Doria, G.P. Gallerano, E. Giovenale, G. Messina, G. Doucas, M.F. Kimmitt, H.L. Andrews, and J.H. Brownell. Can coherent smith–purcell radiation be used to determine the shape of an electron bunch? *Nuclear Instruments and Methods in Physics Research Section A: Accelerators, Spectrometers, Detectors and Associated Equipment*, 483(1):263 – 267, 2002. Proceedings of the 23rd International Free Electron Laser Confere nce and 8th FEL Users Workshop.

[125] G. Doucas, M. F. Kimmitt, A. Doria, G. P. Gallerano, E. Giovenale, G. Messina, H. L. Andrews, and J. H. Brownell. Determination of longitudinal bunch shape by means of coherent smith-purcell radiation. *Phys. Rev. ST Accel. Beams*, 5:072802, Jul 2002.

[126] G. Doucas et al. Longitudinal electron bunch profile diagnostics at 45-MeV using coherent Smith-Purcell radiation. *Phys. Rev. ST Accel. Beams*, 9:092801, 2006.

[127] V. et al. Blackmore. First measurements of the longitudinal bunch profile of a 28.5 GeV beam using coherent Smith-Purcell radiation. *Phys. Rev. ST Accel. Beams*, 12:032803, Mar 2009.

[128] Nicolas Delerue, George Doucas, Ewen Maclean, and Armin Reichold. Longitudinal bunch profile diagnostics in the 50fs range using coherent Smith-Purcell radiation. 2009.

[129] R Bartolini, C Clarke, N Delerue, G Doucas, and A Reichold. Electron bunch profile reconstruction in the few fs regime using coherent Smith-Purcell radiation. *Journal of Instrumentation*, 7(01):P01009, 2012.

137

[130] H.L. Andrews, F. Bakkali Taheri, J. Barros, R. Bartolini, L. Cassinari, C. Clarke, S. Le Corre, N. Delerue, G. Doucas, N. Fuster-Martinez, I. Konoplev, M. Labat, C. Perry, A. Reichold, S. Stevenson, and M. Vieille Grosjean. Longitudinal profile monitors using coherent Smith-Purcell radiation. In Jens Osterhoff Arnd E. Specka Ralph Assmann, Massimo Ferrario, editor, *1st European Advanced Accelerator Concepts Workshop (EAAC2013)*, volume 740, pages 212–215, La Biodola, Italy, June 2013. Elsevier.

[131] L. Andrews, H. F. Bakkali Taheri, J. Barros, R. Bartolini, V. Bharadwaj, C. Clarke, N. Delerue, G. Doucas, N. Fuster-Martinez, M. Vieille-Grosjean, V. Konoplev, I. M. Labat, S. Le Corre, C. Perry, A. Reichold, and S. Stevenson. Reconstruction of the time profile of 20.35 gev, subpicosecond long electron bunches by means of coherent smith-purcell radiation. *Phys. Rev. ST Accel. Beams*, 17:052802, May 2014.

[132] J H Brownell, G Doucas, M F Kimmitt, J H Mulvey, M Omori, and J E Walsh. The angular distribution of the power produced by smith-purcell radiation. *Journal of Physics D: Applied Physics*, 30(17):2478, 1997.

[133] http://www.tau.ac.il/ phchlab/. Spectrum of the hydrogen atom.

[134] N. Delerue, S. Jenzer, V. Khodnevych, J-P. Berthet, F. Glotin, J-M. Ortega, and R. Prazeres. Study of Short Bunches at the Free Electron Laser CLIO. In *IPAC2016*, Proceedings of IPAC2016, page MOPMB005, Busan, South Korea, May 2016.

[135] J. H. Brownell and G. Doucas. Role of the grating profile in Smith-Purcell radiation at high energies. *Phys. Rev. ST Accel. Beams*, 8:091301, 2005.

[136] C. A. J. Palmer and Loewen E. *Diffraction grating handbook*. Newport Corporation, 2005.

[137] Solène Le Corre. Study of the polarization of smith-purcell radiation. Master's thesis, ENS Lyon, 2012.

[138] Clément Duval. Simulation of smith-purcell radiation following a van den berg approach. Master's thesis, ENS Lyon, 2016.

[139] D.A. Zhuravlev. E. g. loewen and e. popov diffraction gratings and their applications (marcel dekker, new york, 1997). *Optics and Spectroscopy*, 88(1):143–144, 2000.

[140] F. Bakkali Taheri, G. Doucas, I.V. Konoplev, A. Reichold, S.R. Stevenson, H.I. Andrews, R. Bartolini, V. Bharadwaj, C.I. Clarke, N. Delerue, N. Fuster Martinez, D.A. Smith, and P. Stoltz. Spectra of Coherent Smith-Purcell Radiation Observed from Short Electron Bunches: Numerical and Experimental Studies. In *IPAC 13 - 4th International Particle Accelerator Conference*, pages 801–803, Shanghai,

China, May 2013. Joint Accelerator Conferences Website. MOPWA056 - ISBN978-3-95450-122-9.

[141] O. Grimm and P. Schmüser. Principles of longitudinal beam diagnostics with coherent radiation. *TESLA FEL note*, page 03, 2006.

[142] N. Delerue, J. Barros, M. Vieille-Grosjean, O. Bezshyyko, V. Khodnevych, and T. Shevchenko. Study of phase reconstruction techniques applied to Smith-Purcell radiation measurements. In *IPAC'14 - THPME088*, 2014.

[143] Nicolas Delerue, Joanna Barros, Oleg Bezshyyko, and Vitalii Khodnevych. Study of Phase Reconstruction Techniques applied to Smith-Purcell Radiation Measurements. *ArXiV*, 2015.

[144] Maksym Malovystia. Simulation of the smith-purcell radiation and designing stepper motor control system. Technical report, LIA IDEATE France-Ukraine, 2015.

[145] J. Amann et al. Facility for Advanced Accelerator Experimental Tests at SLAC (FACET) Conceptual Design Report. 2009.

[146] N. Delerue, J. Barros, S. Jenzer, M. Vieille Grosjean, L. Cassinari, M. Labat, G. Doucas, I.V. Konoplev, A. Reichold, A. Faus-Golfe, N. Fuster Martinez, and J. Resta-Lopez. Presentation of the Smith-Purcell Experiment at SOLEIL. In *IBIC 2013 - TUPC37*, 2013.

[147] Nicolas Delerue, Joanna Barros, Nicolas Hubert, Stéphane Jenzer, Vitalii Khodnevych, Marie Labat, and Maksym Malovytsia. Ipac 17 soleil. page MOPMB002, 2017.

[148] Nicolas Delerue, Joanna Barros, Nicolas Hubert, Stéphane Jenzer, Vitalii Khodnevych, Marie Labat, and Maksym Malovytsia. First Measurements of Coherent Smith-Purcell Radiation in the SOLEIL Linac. In *Proceedings, 7th International Particle Accelerator Conference (IPAC 2016): Busan, Korea, May 8-13, 2016*, page MOPMB002, 2016.

[149] M. Ageron et al. Study report on free electron laser project with 3-GHz HF Linear Accelerator (Collaboration For An Infrared Laser at Orsay). *LAL-RT-89-04*, 1989.

[150] J.C. Bourdon, R. Belbeoch, M. C. Bernard, P. Brunet, B. Leblond, M. Omeich, E. Plouviez, J. Rodier, R. Chaput, M. Bergher, and J.M. Ortega. Commissioning the Clio injection system. In *Free Electron Laser International Conference 12*, volume 304, pages 322–328, Paris, France, September 1990. Elsevier.

[151] F. Glotin et al. First lasing of the CLIO FEL. *Conf. Proc.*, C920324:620–622, 1992.

[152] N. Delerue, V. Khodnevych, and O. Bezshyyko. Comparison of Coherent Smith-Purcell Radiation and Coherent Transition Radiation. In *IPAC2016*, Proceedings of IPAC2016, page MOPMB003, Busan, South Korea, May 2016.

[153] A. Aryshev, A. Potylitsyn, G. Naumenko, M. Shevelev, K. Lekomtsev, L. Sukhikh, P. Karataev, Y. Honda, N. Terunuma, and J. Urakawa. Monochromaticity of coherent smith-purcell radiation from finite size grating. *Phys. Rev. Accel. Beams*, 20:024701, Feb 2017.

[154] Nicolas Delerue and Vitalii Khodnevych. Ipac 17 clio. 2017.

[155] Vitalii Hodnevych. Clio report. Master's thesis, Unpublished, 2017.

[156] J. Barros, N. Delerue, M. Vieille-Grosjean, I. Dolenc Kittelmann, and C. Thomas. On the suitability of longitudinal profile measurements using coherent Smith-Purcell radiation for high current proton beams. In *IPAC'14 - THPME089*, 2014.

[157] T. P. A. Ibbotson et al. Laser-wakefield acceleration of electron beams in a low density plasma channel. *Phys. Rev. ST Accel. Beams*, 13:031301, 2010.

[158] S. Kneip et al. Near-GeV Acceleration of Electrons by a Nonlinear Plasma Wave Driven by a Self-Guided Laser Pulse. *Phys. Rev. Lett.*, 103:035002, 2009.

[159] Antoine Chancé, Olivier Delferrière, Jérôme Schwindling, Christelle Bruni, Nicolas Delerue, Arnd Specka, Brgitte Cros, Gillies Maynard, Bhooshan S. Paradkar, and Patrick Mora. Transport line for a multi-staged laser-plasma acceleration: DACTOMUS. *Nucl. Instrum. Meth.*, A740:158–164, 2014.

[160] Brigitte Cros et al. Electron Injector for Multi-Stage Laser-Driven Plasma Accelerators. In *Proceedings, 8th International Particle Accelerator Conference (IPAC 2017): Copenhagen, Denmark, May 14-19, 2017*, page WEPVA001, 2017.

[161] M Alves, C Arnault, D Auguste, J L Babigeon, F Blot, J Brossard, C Bruni, S Cavalier, J N Cayla, V Chaumat, J Collin, M Dehamme, M Demarest, J P Dugal, M Elkhaldi, I Falleau, A Gonnin, M Jore, E Jules, B Leluan, P Lepercq, F Letellier, E Mandag, J C Marrucho, B Mercier, E Mistretta, C Prevost, R Roux, V Soskov, A Toutain, A Variola, O Vitez, and H Monard. Phil photoinjector test line. *Journal of Instrumentation*, 8(01):T01001, 2013.

[162] Fabien Ple, Moana Pittman, Gerard Jamelot, and Jean-Paul Chambaret. Design and demonstration of a high-energy booster amplifier for a high-repetition rate petawatt class laser system. *Opt. Lett.*, 32(3):238–240, Feb 2007.

[163] Daniel Zimmer, Bernhard Zielbauer, Moana Pittman, Olivier Guilbaud, Jamil Habib, Sophie Kazamias, David Ros, Vincent Bagnoud, and Thomas Kuehl. Optimization of a tabletop high-repetition-rate soft x-ray laser pumped in double-pulse single-beam grazing incidence. *Opt. Lett.*, 35(4):450–452, Feb 2010.

[164] Olivier Delmas, Moana Pittman, Kevin Cassou, Olivier Guilbaud, Sophie Kazamias, Gabriel V. Cojocaru, Olivier Neveu, Julien Demailly, Elsa Baynard, Daniel Ursescu, and David Ros. Q-switched laser-assisted grazing incidence pumping (qa-grip) for efficient soft x-ray laser generation. *Opt. Lett.*, 39(21):6102–6105, Nov 2014.

[165] Nicolas Delerue. The esculap project at orsay. In *EAAC*, 2017.

[166] Viacheslav Kubytskyi et al. Modelling of laser-plasma acceleration of relativistic electrons in the frame of esculap project. In *EAAC*, 2017.

[167] L. M. Gorbunov and V. I. Kirsanov. Excitation of plasma waves by an electromagnetic. *JETP*, 66:290, 1987.

[168] P. Sprangle, E. Esarey, A. Ting, and G. Joyce. Laser wakefield acceleration and relativistic optical guiding. *Applied Physics Letters*, 53(22):2146–2148, 1988.

[169] B. S. Paradkar, B. Cros, P. Mora, and G. Maynard. Numerical modeling of multi-gev laser wakefield electron acceleration inside a dielectric capillary tube. *Physics of Plasmas*, 20(8), 2013.

[170] Klaus Floettmann. Astra - a space charge tracking algorithm.

[171] Ke WANG et al. Longitudinal compression and transverse matching of electron bunch for external injection lpwa at esculap. In *EAAC*, 2017.

[172] Paul Andreas Walker et al. HORIZON 2020 EuPRAXIA Design Study. In *Proceedings, 8th International Particle Accelerator Conference (IPAC 2017): Copenhagen, Denmark, May 14-19, 2017*, page TUOBB3, 2017.

[173] Jacqueline Eidelman. Le palais de la découverte 1934-1937 : culture scientifique et professionnalisation de la recherche. In *Cahiers pour l'histoire du CNRS*, volume 1990-9, page 127, 1990.

[174] N. Delerue. Accélérateurs de particules, collisions imminentes. *Revue du Palais de la Decouverte*, 399:28–37, 2015.

[175] N. Delerue. Les oeuvres d'art décryptées aux rayons x. *Cosinus Magazine*, 182:24–31, 2016.

[176] N. Delerue. Du chocolat dans un accélérateur de particules ! *Cosinus Magazine*, 185:1, 2016.

[177] X. Pintat and J. Lorgeoux. La nécessaire modernisation de la dissuasion nucléaire. Rapport d'information 560, Sénat, 2017.